THE COOL HYDROGEN-DEFICIENT CARBON STARS AND THEIR ATMOSPHERES

Kevin N. Jones

A Thesis Submitted for the Degree of PhD
at the
University of St Andrews

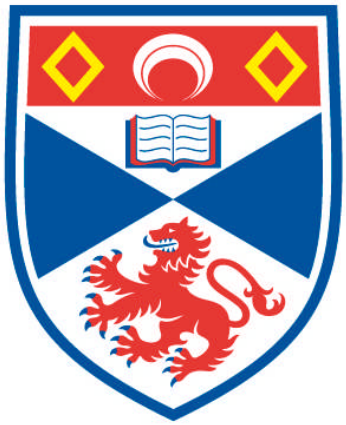

1992

THE UNIVERSITY OF ST. ANDREWS

The Cool Hydrogen-Deficient Carbon stars and their Atmospheres

Kevin N. Jones

Submitted for the degree of Ph. D.

July, 1991.

Abstract

Photoelectric photometry of a large sample of R CrB and hydrogen-deficient carbon stars was obtained over a period of five months in order to search for variability and determine the period if variable. All the stars in the sample were found to be variable. Only for the stars S Aps, U Aqr and V CrA were sufficient observations obtained to enable periods to be identified. The determined periods were 39.7, 41.8 and 69.0 days respectively. These periods are in agreement with the theoretical period-temperature relationship.

Photoelectric photometry of the hot hydrogen-deficient star DY Cen was obtained over a period of four weeks. DY Cen was confirmed to be variable and the dominate period of 3.8 days determined. This period was consistent with the period-temperature relationship.

Model atmospheres were calculated for hydrogen-deficient compositions with temperatures between 5000–8000K and surface gravities between 0.0 and 4.4. The models included the effects of molecular formation, convection and line-blanketing. It was shown that the temperature structure was strongly dependent on the composition, in particular the ratios of C/He and H/He.

R CrB was re-analysed using these new models. The derived atmospheric parameters were $T_{eff} = 7400 \pm 500$K, $\log g = 0.55 \pm 0.25$, $\xi_t = 8 \pm 2$kms^{-1} and C/He=0.005. High resolution spectra were obtained of RY Sgr in order to do a similar analysis. The derived parameters were $T_{eff} = 7000 \pm 500$K, $\log g = 0.65 \pm 0.25$, $\xi_t = 10 \pm 2$kms^{-1} and C/He=0.005. Both stars were found to have solar metallicities with no over-abundances of s-process elements. The abundances of C, N and O were all enhanced relative to the solar values.

Medium resolution spectra were obtained at the Isaac Newton telescope of suspected R CrB stars in order to correctly classify them. The stars were classified on the basis of the strength of the hydrogen lines and the G band. BG Cep, LO Cep, CC Cep, DZ And, RZ Vul, VZ Vul, V638 Her and V1405 Cyg were all classified as not being R CrB stars. UV Cas, SU Tau and SV Sge were classified as R CrB stars.

I Kevin Jones hereby certify that this thesis has been composed by myself, that it is a record of my own work and that it has not been accepted in partial or complete fulfilment of any other degree or professional qualification.

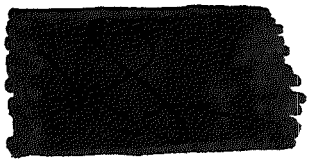

K.N. Jones

I was admitted to the Faculty of Science of the University of St. Andrews under Ordinance General No. 12 on 1*st* October 1988 and as a candidate for the degree of Ph.D. on 1*st* October 1989.

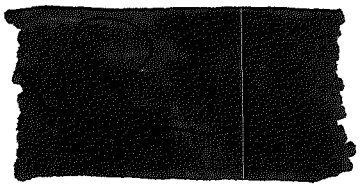

K.N. Jones

I hereby certify that the candidate has fulfilled the conditions of the Resolution and Regulations appropriate to the degree of Ph.D.

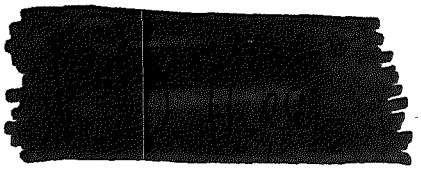

P.W. Hill

In submitting this thesis to the University of St. Andrews I understand that I am giving permission for it to be made available for use in accordance with the regulations of the University Library for the time being in force, subject to any copyright vested in the work not being affected thereby. I also understand that the title and the abstract will be published, and that a copy of the work maybe made and supplied to any *bona fide* library or research worker.

Acknowledgements

I would like to thank my supervisor Dr. P Hill for providing the opportunity to undertake this thesis and for his help and suggestions which have enabled me to complete it. Special thanks must be given to Don for his unceasing enthusiasm, Simon for technical help with my computer models and to Helen for proof-reading this thesis.

The support and friendliness of the staff, particularly Dr. D. Kilkenny, of the South African Astronomical Observatory were greatly appreciated during my long periods at Sutherland and Cape Town. The director of SAAO, Dr. M. Feast, is thanked for his more than generous allocation of telescope there.

I would like to thank the Science and Engineering Research Council for my postgraduate award and financial support whilst abroad. Additional thanks are given to the R. D. Hughes Foundation for their sponsorship throughout my university education. The use of the facilities at the University of St. Andrews was appreciated, with special thanks to Roger Stapleton our computer manager and the research students in the astronomy group.

The final and biggest thanks must go to my parents, who despite not understanding why I wanted to do astronomy, have supported me wholeheartedly throughout the last four years.

Contents

List of Figures

List of Tables

Chapter 1

An introduction to the cool hydrogen-deficient stars

1.1 Hydrogen-deficient stars

There are several different classes of stars which have hydrogen-deficiency and these are listed below:

1. Hydrogen-deficient carbon stars (HdC);
2. R Coronae Borealis stars (R CrB);
3. Hot R CrB stars;
4. Extreme helium stars (EHe);
5. Intermediate helium stars (magnetic stars);
6. Hydrogen-deficient binaries;
7. Wolf-Rayet stars;
8. Some central stars of planetary nebulae;
9. Hydrogen-deficient white dwarfs (DB).

The work presented here mainly concerns the HdC and R CrB groups of stars together with possible connections between them and the hot R CrB and EHe stars. The relative positions of these objects are shown in the Hertzsprung-Russell diagram in figure 1.1

1.2 The Hydrogen-deficient carbon stars

From their position in the HR diagram it can be seen that the HdC stars are cool supergiants. Only five HdC stars have been identified, although there are expected to be many more HdC stars hidden within the population of cool carbon stars. However medium resolution spectroscopy is required to determine hydrogen-deficiency. The HdC stars are all concentrated towards the galactic plane and centre and are thought to belong to an intermediate Population II. None of the five HdC stars were found to have an infra-red excess from the IRAS satellite observations (Walker 1986).

1.2.1 Physical Properties

All the known physical properties were determined by Warner (1967). They were obtained from a coarse analysis of high resolution coudé spectroscopy for each of the stars. All the stars had temperatures of T_{ex} = 5000K, and the calculated electron pressures implied low gravities.

The hydrogen abundance could only be given a lower limit, of [H/Fe]< -0.7 due to the uncertainty in detecting and measuring the hydrogen Balmer lines. It is interesting to note that HD 144839 was much less hydrogen-deficient, with [H/Fe]=3.7.

Carbon was determined to be overabundant by a factor of 3–10 with respect to the solar value.

With the exceptions of hydrogen and carbon, the rest of the elements were found to have solar abundances.

1.2.2 Pulsation

The theoretical studies of Saio and Wheeler (1985) and Weiss (1987b) predicted that the HdC stars would be unstable to pulsation from linear nonadiabatic models. However, at that time no observations had indicated variability. Variability was discovered by Kilkenny *et al.* (1988) in all five objects. Typically the amplitudes observed were $\Delta V \sim 0.05$, although HD 175893 has an amplitude of $\Delta V = 0.25$, which accounts for the late discovery of variability. From these observations they were only able to determine that the periods were greater than 20 days.

Further observations by Jones *et al.* (1989) and Lawson (1990) confirmed the existence of variability. Lawson obtained sufficient observations to determine the periods of HD 137613, HD 148893 and HD 182040 which were 110, 156 and 109 days respectively for the dominant period. The observations of Jones *et al.* (1989) and work presented in Chapter 2 give a period of 53 days for HD 137613.

The combination of very low amplitude oscillations and long periods makes it extremely difficult to obtain precise periods. This is further complicated by the fact that the R CrB stars are known to be only quasi-periodic and it would not be unexpected for the HdC stars to exhibit such behaviour.

1.3 The R Coronae Borealis stars

The R CrB stars are similar to the HdC stars, only being distinguished from HdC stars by their extreme variable behaviour and infra-red properties. They are halo stars of intermediate Population II. The luminosity of the galactic R CrB stars is estimated from the observations of the three LMC R CrB stars and results in luminosities of $\sim 10,000\,L_{\odot}$(Feast 1972). The high luminosities and late spectral types imply that the R CrB stars must be supergiants. All the R CrB stars, except possibly XX Cam, are variable. The variability is divided into two phases: a semi-periodic pulsation of between 30-120 days and a random anti-flaring in which the star can dim between 1 and 7 magnitudes over a period of some months, recovering more slowly over several

months to a year. It is these fadings which led to the discovery of nearly all the R CrB stars by the Harvard variable star patrol.

1.3.1 Infra-red Observations

The R CrB stars, except for XX Cam, have an excess of flux in both the near and far infra-red wavelengths. Kilkenny *et al.* (1984) showed that the visual (UBVRI) and infra-red observations (JHKLMNQ) could be interpreted as emission from two black bodies, one representing the star and the other a cool surrounding dust cloud. The observations and fitted black bodies are shown in Figure 1.2. The estimated errors in the temperatures are ±500K and ±50K for the star and cloud respectively.

Walker (1986) reviewed the survey work of IRAS on the R CrBs at wavelengths of 12, 25, 60 and 100 microns. The results obtained agree well with those of Kilkenny *et al.* (1984) although for some of the stars a power law fit to the spectrum was better than the blackbody fit. Again the HdC stars showed no red excess confirming the absence of any surrounding dust cloud.

When the point spread function for the observations of R CrB and SU Tau was compared with that of the point source NGC 6543 Walker (1986) found that at 60 and $100\mu m$ they were extended. The extension amounted to about 20 arcminutes. Similar observations of RY Sgr failed to find any such extension.

Gillet and Blackman (1986), in a more sophisticated analysis of the IRAS observations of R CrB, calculated that the shell had a temperature of 25–30K and was spherically extended by 18 arcminutes. They assumed a distance of 1.6Kpc to R CrB giving a shell extension of 8pc (far larger than the dust shells surrounding other late type stars) and a total luminosity of $28\,L_{\odot}$ with a minimum mass of $0.25\,M_{\odot}$.

The shell was found to have a nearly constant temperature throughout. For equilibrium grain heating this requires that an external heating source dominate the grain heating. Given estimates of the stellar luminosity and shell mass this leads to a value for the interstellar radiation field (ISRF) ten times greater than that in the solar vicinity. Although this is a large value for the ISRF, observations by Soifer *et al.* (1986)

found similar values towards M31.

The constant temperature shell does not quite rule out impulsive grain heating from the stellar radiation field. However, it does require that the mass loss rate be highly time dependent following an inverse square law, and that the grain size be very small in comparison with the measured values. Therefore this scenario is considered very unlikely.

This shell was tentatively identified as the fossil remnant of R CrB's hydrogen-rich envelope ejected in a phase of constant mass loss.

The infra-red flux emitted from the shell is known to be variable (Glass 1978 and Menzies 1986). This is best studied at L (3.5μm), where the flux from the shell dominates that of the photosphere. Observations over fifteen years show that the dust shells surrounding many R CrB stars are variable by δL$\sim$1–2, with periods of thousands of days. In common with the visual pulsations the infra-red variations are also only quasi-periodic (Feast 1990).

1.3.2 Pulsation

All R CrB stars are variable on time scales of 30–150 days with the possible exception of XX Cam. Only RY Sgr has a well defined period of 37.7 days which is decreasing with time (Kilkenny 1982, Lawson 1990). The period changes are in agreement with those predicted for evolving low mass helium stars (Schönberner 1977, Weiss 1987b).

The rest of the R CrB stars do not show such periodic behaviour, and are often termed quasi-periodic. Their periods vary from season to season and have a smaller amplitude. Recent observations over several seasons together with period determinations are given in Lawson (1990) and Chapter 2. The temperatures and determined periods including sources are given in Table 1.1 for most of the R CrB stars.

Kilkenny (1983) observed a change in the period of S Aps following the 1971 minimum. The period changed from 120 to 40 days, possibly due to a change in mode. It was not possible to ascertain whether or not the change was a direct consequence of

Table 1.1: Periods and effective temperatures of R CrBs.

Star	Period (Days)	Temperature (K)
S Aps	39–43	4000
V CrA	57–112	4000
WX CrA	60	5000
RZ Nor	42	5000
GU Sgr	38	5000
RS Tel	38	5000
VZ Sgr	47	?
UW Cen	43	6800
R CrB	46	7000
RT Nor	45–46	7000
RY Sgr	37.7	7100
XX Cam	?	7200
DY Cen	3.8–5.5	14000
U Aqr	40–42	?

the minimum because no data had been obtained prior to its commencement.

The observed periods generally agree with the predictions for F mode pulsation in the linear nonadiabatic models of Weiss (1987) and Saio and Jeffery (1988). The periods also appear to agree with the calculated temperature-period relationships derived, although it most be noted that the temperatures of most of the R CrB stars are poorly determined. However the longer periods observed by Lawson (1990) (see Chapter 2) and the earlier period of S Aps do not fit this model.

The possible cause of the quasi-periodicity in the R CrB stars is the combination of pulsation and shallow minima occurring randomly.

1.3.3 The Minima

R CrB stars randomly fade visually by between 1 and 7 magnitudes then recover slowly over a period of some months to a year. Rosenbush (1986) showed that for RY Sgr and

R CrB the time between minima is distributed regularly up to a limit of about 1800 days and 1540 days respectively. Earlier work by Howarth (1975) and Tempesti *et al.* (1975) had suggested that the time between minima followed the Poisson distribution, but they failed to realise that the onset of each minimum always falls on or near the same phase of pulsation. This link was first noted by Pugach (1984) and may provide an important clue to the mechanism of minima generation.

Extensive observations of R CrBs through minima have been carried out by Alexander *et al.* (1972) for RY Sgr and Lawson (1990) for R CrB, consisting of simultaneous photometry and spectroscopy. The major points of interest are that the decline and subsequent rise are asymmetric, the decline occurring quicker than the rise. An extensive chromospheric emission line spectrum becomes visible with Ca H and K and Na D lines especially prominent. These lines have a large velocity of around 100–200 Kms^{-1} with respect to the photosphere. Broad He I emission lines have also been seen in R CrB and RY Sgr and are most likely to be due to high energy electron excitation. Surendiranath *et al.* (1986) modelled these emission lines and obtained the results $T_e = 10,000\mathrm{K}$ and $N_e = 10^{11}\mathrm{cm}^{-3}$.

Photometry by Raveendran *et al.* (1986) in the colours B and V of R CrB stars whilst at maximum showed that the emitted light was linearly polarized by 0.1–2%. XX Cam was included in the sample and showed a 2% linear polarization despite having no detectable infra-red excess. Stanford *et al.* (1988) observed R CrB during the 1986 minimum and found that the degree of polarization increased as the star faded.

Forrest *et al.* (1972) showed that during a minimum the visual and infra-red fluxes do not vary in antiphase, and hence the total bolometric flux is not conserved. This result implies that the dust cloud surrounding the central star cannot be spherically symmetric.

Recent observations by Pollacco *et al.* (1991) of UW Cen whilst in minimum revealed the presence of a faint reflection nebula surrounding the star. The nebula extended for 8 arcseconds and was circular, centred on the star. The nebula also showed two sets of diagonally opposed jets.

All models for the R CrB phenomena have relied upon dust clouds of some form or other occasionally obscuring the star. The earliest model is that of O'Keefe (1939) in which orbiting dust clouds passing in front of the star were the cause of the minima. However, this model is not consistent with the observations, since for example, it would imply that the fall and rise would be symmetric and chromospheric emissions would only be faintly seen, if at all.

The most comprehensive model presented to date is that of Feast (1986), which goes a long way in explaining most of the observations. However, it must be stressed that the model is still only phenomenological.

The R CrB star ejects a puff of dust in a random direction and a minimum occurs whenever a puff is in the line of sight. Observations by Goldsmith and Evans (1985) and Lawson (1990) have shown that the condensation of the puff to form the opaque cloud can occur at different phases of the decline, giving rise to red and blue declines. The differences arise from geometrical considerations of the eclipse phenomena. The extreme cases are given below and the normal observed decline is a combination of the two.

In the red decline the puff is ejected and expands laterally until it covers the complete stellar hemisphere before condensing and becoming opaque. It then obscures the photosphere and chromosphere equally, hence no chromospheric emission is seen.

In the blue decline the reverse situation happens. The puff condenses and becomes opaque whilst still small then expands laterally and radially. It progressively obscures first the photosphere and then the chromosphere. The blue colour during the initial stages of the decline is due to a broad emission feature between 3900–4000Å which may be due to unresolved chromospheric emission lines and/or continuum emission (Lawson 1990).

The size of the cloud ejected cannot be too large otherwise there would be an increase in the infra-red flux during minimum. In order to observe the permanent excess there must be enough puffs re-radiating that the addition of an extra puff does not significantly add to the excess. It is estimated that about ten puffs would be

sufficient (Feast 1986).

If the grain formation occurs near the photosphere then the emission lines seen will be due to the decay of the upper populated levels as the continuum is blocked by the cloud. However the dust/gas in this region will be too hot to condense to form an opaque cloud. Fadeyev (1986) proposed that the emission lines seen are created by a shock wave . This would fit the observation that the emission lines are blue-shifted by $\sim$100Kms^{-1}. If the mechanism of grain formation is via a shock wave the region of condensation can be much further from the star in a cooler region. The presence of pulsation induced shock waves has been observed in RY Sgr (Lawson 1986).

Fadeyev (1986) showed that the minimum distance for the carbon gas ejected from the surface of an R CrB of T_{eff}=6000K to condense was between 10–20 photospheric radii.

The grain composition and size was determined from modelling the ultra-violet emission feature at 2400–2500Å (Hecht *et al.* 1984). The assumptions of spherical carbon particles and a Mathis, Rumpl and Nordssieck particle distribution ($N(r) = kr$) were used to fit a model to the observations. RY Sgr was best fitted by a model with amorphous carbon grains with a mean particle size of 150–600Å and R CrB with amorphous carbon grains of 100–350Å or $\sim$ 400Å for graphite.

Given the particle and cloud sizes the mass of solid carbon ejected is $10^{-8}\,M_{\odot}$, and if the composition of the gas was initially photospheric the total cloud mass is $10^{-7}\,M_{\odot}$.

Observation of polarized light during minima by Stanford *et al.* (1988) led to the conclusion that there existed a preferred plane of ejection of puffs. They suggested that non-radial pulsations might be the cause of the expulsion of clouds of dust and gas. The jets in UW Cen discovered by Pollacco *et al.* (1991) may be associated in some way with the ejection of the puffs and again imply a preferred plane of ejection, unless there exists a third pair of jets lying perpendicular to the line-of-sight. Then as long as the opening angle is sufficiently large all R CrB stars would exhibit deep minima.

One of the difficulties with this idea is the absence of hydrogen-deficient stars

with infra-red excesses and no minima which occur when the ejection plane is at ninety degrees to the line-of-sight. However, these stars may exist but remain undiscovered since most if not all R CrB stars were found by their photometric behavior. The R CrB periods appear to agree with those predicted for radial mode pulsations, but as the periods are difficult to measure accurately, one cannot discount non-radial pulsation.

Feast (1990) suggested an alternative model in which mass loss is constant and forms a shell 20–100 stellar radii from the surface. Then when the density reaches some critical value, localised inhomogeneities trigger grain formation and a minimum occurs. The dust is then driven from the shell by radiation pressure. Subsequent minima will only occur after sufficient time has passed to replenish the shell.

1.3.4 Abundances

The unusual composition of the R CrB stars was first noted in 1935 when Berman (1935), using the curve of growth technique, showed R CrB to be hydrogen-deficient and carbon rich. His results were only qualitatively correct.

More accurate curve of growth abundance determinations were not attempted until the 1960's and then only for the brightest R CrB stars : R CrB - Searle (1961), RY Sgr - Danziger (1965) and XX Cam - Orlov and Rodriguez (1974). In each case the analysis was differential, δ Cma for R CrB and β Aqr for RY Sgr.

Searle (1961) found that the carbon — iron ratio was 25 times greater than that of δ CMa but that the metals had solar abundances into within the errors of the analysis. If it is assumed that the iron abundance is solar then the helium abundance can be estimated. On this basis the composition of RCrB is $X = 0.0005, Y = 0.91, Z = 0.09$ and $Z_c = 0.75Z$. The other important point made was that the major source of opacity was the photo-ionization of carbon.

In most respects the results of the analysis of RY Sgr (Danziger 1965) are essentially the same as those of R CrB, but with a slightly greater carbon abundance and an excess of ^{7}Li and Na. XX Cam (Orlov and Rodriguez 1974) had abundances similar to the previous two R CrB stars but with 100 times more carbon.

Table 1.2: Model Atmosphere results

Star	T_{eff}(K)	log g	V_t (Km/s)	Author
R CrB	6900±500	0.15±0.5	6.5±1	S75
R CrB	7000±250	0.50±0.3	8.0	CL82
XX Cam	7200±500	0.20±0.5	9.5	S75
XX Cam	7000±250	0.00±0.3	8.0	CL82
RY Sgr	7100±500	0.10±0.5	11.0	S75
UW Cen	6800±300	0.00	7.0	GR86

Schönberner (1975) adapted his model atmosphere program STERNE to enable R CrB stars to be analysed. The program Sterne was originally written to analyse the hotter EHe stars and the main changes required were the addition of extra opacity sources, important at the lower temperatures, and reduced hydrogen abundances. The models were calculated using the classical model atmosphere assumptions (see Chapter 4) without taking into account the effects of convection or line blanketing. All analyses to date have used these models.

The results of the analyses by Schönberner (1975, S75), Cottrell and Lambert (1982, CL82) and Giridhar and Rao (186, GR86) are presented in Table 1.2 together with the derived abundances in Table 1.3. The errors were reduced by CL82 through the use of higher signal-to-noise spectra, obtained with a Reticon detector, and observations at longer wavelengths where the line crowding is less severe.

CL82 also obtained spectra of RY Sgr in order to do a fine analysis but found that the absorption line profiles were time dependent and often split. This was most obvious in the iron and titanium lines which often were seen in emission. These phenomena were later understood as being due to the presence of a shock wave travelling through the atmosphere (Lawson 1986).

The differences between the abundances obtained by S75 and CL82 are due principally to the different values of N_{He}/N_C used. In CL82 they used the fact that the derived equivalent widths of weak C I lines should be independent of N_{He}/N_C provided that the ratio exceeds some minimum value. It must be noted that the line formation program used by CL82 calculated values for the continuous opacity 0.2dex less than

Figure 1.1: Hertzsprung-Russell diagram showing the positions of the R CrB, intermediate helium stars, EHe stars (dots in upper half of figure), and helium rich sdO stars (dots in lower half). The main sequence is also shown (solid curve).

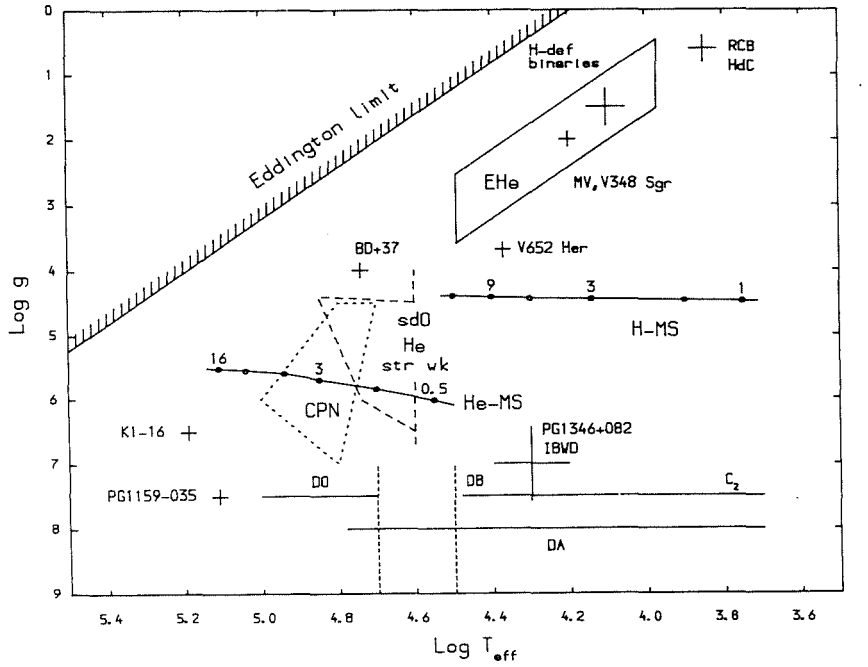

Table 1.3: Abundances of R CrB stars.

Element	R CrB		RY Sgr	XX Cam		EHe stars	Sun
	S75	CL82	S75	S75	CL82	S74	G84
H	7.8	6.6	7.4	≤ 6.5	≤ 3.9	≤ 8.4	12.00
He	11.5	11.5	11.5	11.5	11.5	11.5	11.00
C	10.0	9.1	10.0	10.0	9.0	9.7	8.7
N	—	8.1	8.8	—	8.5	—	8.0
O	—	8.8	8.5	—	8.9	≤ 8.4	8.9
Fe	7.1	6.5	7.3	7.5	6.6	7.4	7.7

The EHe abundances are an average taken from Schönberner (1974).
The solar abundances are from Grevesse (1984).

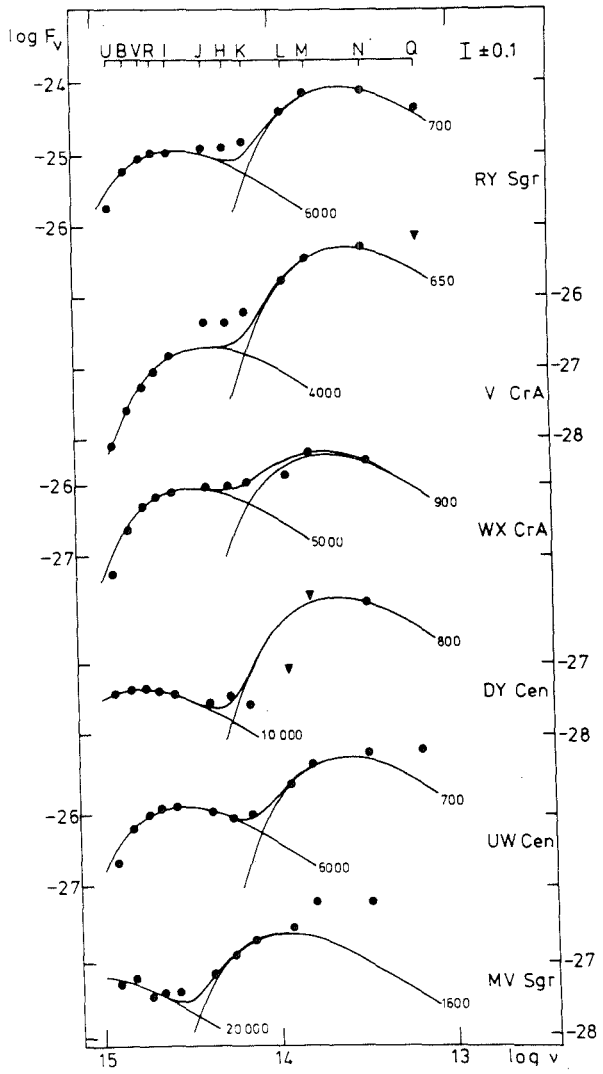

Figure 1.2: The solid lines are blackbody curves for the indicated temperatures fitted to the broadband data.

those used in the model atmosphere calculations.

Both Danziger (1965) and CL82 obtained lower limits for the ratio $^{12}C/^{13}C$ of ~ 40 from the absence of $^{13}C^{12}C$ Swan band heads. The predicted value for this ratio assuming that the ^{13}C is due to the CNO cycle is ~ 3.4.

In general the heavy elements were found to have solar values.

CL82 only observed the Li 6707Å line in R CrB and derived a typically primeval abundance. From the measured wavelength CL82 estimated that the ratio $^{7}Li/^{6}Li > 7$. Since Li is completely destroyed in the stellar core during normal evolution, and even in the outer convective envelope of a giant is reduced to a factor of 10^3 or 10^4 less than that found in R CrB, some mechanism must be found to regenerate Li. The ratio of $^{7}Li/^{6}Li$ rules out the possibility of spallation reactions at the stellar surface so the most likely reaction is $^{3}He(\alpha, p)^{7}Be(e^{-}, \nu)^{7}Li$ at the base of the convective envelope. The produced Li is then swept away from the hot zone and eventually deposited in the surface layers.

Hunger *et al.* (1982) used improved spectral data for R CrB and XX Cam with the curve of growth method to examine them for peculiarities in their Li and Ba abundances and found both to be over-abundant. In accounting for the extra Li, Hunger favours the supra-thermal spallation reactions as the source for the ^{7}Li and is against the ^{7}Be mechanism on the basis of arguments proposed by Canal *et al.* (1977). If spallation processes are creating the ^{7}Li then a method of creating high energy (1MeV) non-thermal particles must be found.

Ba is an s-process element created by the reaction of iron with thermal neutrons; the most promising sources for it are the reaction:

$$^{13}C(\alpha, n)^{16}O \text{ and } ^{22}Ne(\alpha, n)^{25}Mg$$

In order to determine which reaction is the neutron source the ^{25}Mg abundance must be found, but this has not yet been attempted.

Bond, Luck and Newman (1979) discovered that the R CrB star U Aqr had extremely strong lines of yttrium and strontium, both of which are s-process elements.

Malaney (1985) carried out a curve of growth analysis to determine the abundance of these elements and found the following over abundances with respect to the HdC star HD 182040 of [Sr/Fe]=1.4, [Y/Fe]=1.2, [Zr/Fe]=0.4 and [Ba/Fe]=-0.1. Malaney suggested that the pattern of overabundances was due to a distribution of low density neutron exposures, thought to have occurred during thermal pulsing whilst on the asymptotic giant branch.

1.4 The hot R Coronae Borealis stars

This is a very small class of stars with only three members — DY Cen, MV Sgr and V348 Sgr. They are the hotter analogues of the R CrB stars with estimated temperatures of 14000K, 15400K and 20000K (Pollacco *et al.* 1990, Drilling *et al.* 1984 and Schönberner and Heber 1986) respectively. Like the R CrB stars they have infra-red excesses and fade randomly. V348 Sgr seems to be an extreme example, declining very rapidly by several magnitudes within a few days and spending most of its time faint. DY Cen and V348 Sgr are photometrically variable (see Chapter 3 and Pollacco and Hill 1991) in addition to the minima with low amplitudes and periods in approximate agreement with the period-temperature relationship of Saio and Jeffery (1989).Their spectra show weak or absent hydrogen Balmer lines together with chromospheric wind lines indicative of heavy mass loss.

1.5 The Extreme Helium stars

These are B type giants with enhanced helium I lines and weak or absent hydrogen balmer lines. Table 1.3 gives an average EHe abundance which appears to be similar to that of the R CrB stars. They are generally all variable due to either radial or non-radial pulsation (Landolt 1986) but have not been observed to fade. Further evidence that they do not fade comes from the absence of any infra-red excesses (Walker 1986).

1.6 The evolution of HdC and R CrB stars

Any evolutionary scenario which purports to explain the existence of the HdC and R CrB stars must be able to account for the following observation data:

1. hydrogen-deficiency;
2. enhanced carbon and nitrogen abundances;
3. large circumstellar dust clouds;
4. the paucity of such stars;
5. the temperature and luminosity ranges;
6. single low mass stars.

Nuclear burning of hydrogen through the CNO cycle results in a nitrogen rich and carbon and oxygen poor core. With onset of carbon burning through the 3α process, the carbon and oxygen abundances increase and the nitrogen abundance decreases. From the observed CNO abundances (Table 1.3) the surface composition must consist of a mixture of both CNO and 3α processed material.

All attempts to produce models of the R CrB stars have started from the helium main sequence (HeMS)and evolved the models through core and shell helium burning and carbon core burning if ignition occurred (Oke 1961, Paczynski 1971, Schönberner 1977 and Weiss 1987a). The models of Weiss (1987) are the most realistic and include the most up to date physical data. The following discussion will therefore concentrate on his results.

Two different starting models were used in the calculations; a homogeneous composition of $X = 0.0, Y = 0.972, Z_C = 0.012, Z_O = 0.010$ and $Z_{other} = 0.006$ or a carbon oxygen core with $X = 0.0, Y = 0.0, Z_C = 0.497, Z_O = 0.497$ and $Z_{other} = 0.006$ with the homogeneous composition envelope. The homogeneous models with masses in the range 0.85–0.9 $M_\odot$ and inhomogeneous models with 0.8–0.9 $M_\odot$ evolve into the R CrB region (see Figure 1.3. All models spent the majority of their lifetimes (10^7 years) on

Figure 1.3: Evolution of R CrB models from homogeneous models. The region of the observed R CrBs in the HRD is indicated by the box labelled R CrB. Numbers are stellar masses in solar units.

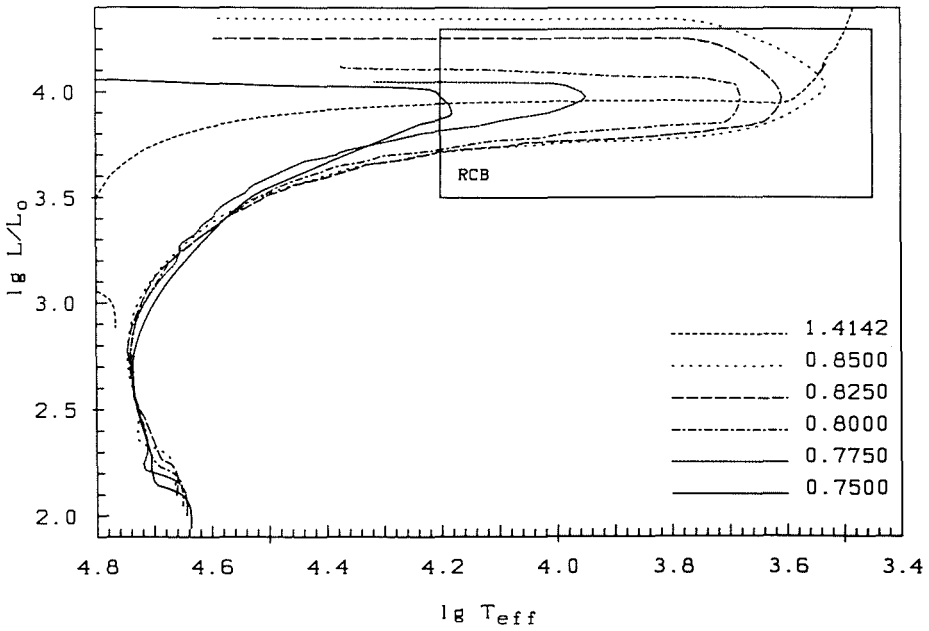

the HeMS spending only 10^5 years in the R CrB region. In both cases Weiss considers the evolution towards the coolest temperature artificial. This is because the helium burning shell is extremely sensitive to the treatment of the nuclear processes and the timestep used for evolution there, but not whilst on the upper path.

The decreasing period of RY Sgr implies that the star is evolving to higher temperatures and is consistent with the timescale for evolution along the upper track ($\sim 10^4$yrs).

Evolution beyond the R CrB region was followed by Schönberner (1977) and the models ended up as DB white dwarfs. Using the evolutionary lifetimes along the upper R CrB track he proposed that the death rate of R CrB stars was sufficient to account for the birth rate of DB white dwarfs.

The evolutionary history of the hydrogen-deficient stars is still a subject full of conjecture. As presented above, it has been possible to generate R CrB models but only using arbitrary starting conditions which are in no way representative of the R CrB

progenitors. Two evolutionary scenarios have been proposed for the formation of R CrB stars and both try to evolve white dwarfs back to the giant region; the merging of a pair of binary white dwarfs and the final helium shell flash in a post AGB star.

1.6.1 Merging white dwarfs

Webbink (1984) showed that for low to intermediate mass binary systems after both phases of mass transfer the system ended up as a pair of close binary white dwarfs, the more massive star being a carbon-oxygen white dwarf (COWD) and the other a helium white dwarf (HeWD). The orbit then decays through the loss of angular momentum due to gravitational radiation until finally they coalesce. The outcome of the coalescence is dependent on the total mass of the system. When the mass lies between 0.5–0.75 $M_{\odot}$ a sub-dwarf O/B star is formed, 0.7–1.45 $M_{\odot}$ a R CrB star and finally when $> 1.45\,M_{\odot}$ a type I supernova.

Iben and Tutukov (1985) showed that after merging to form a R CrB star the COWD forms the inert core around which the HeWD is smeared. The new star then starts to burn helium in a shell and expands to giant dimensions. The surface composition is explained by shear mixing during coalescence, the trace quantity of hydrogen and nitrogen from the HeWD and the carbon and oxygen from the COWD.

This scenario may be tested observationally by looking for suitably close binary white dwarfs where the orbital separation is small enough to allow the orbit to decay in less than the Hubble time. A survey of 54 white dwarfs by Bragaglia *et al.* (1990) found only one definite binary (P=1.15 days) and four possibles with longer periods. The sample is too small to draw definite conclusions, but it does suggest that low mass stars form relatively wide white dwarf binaries. This leads to a merger time of several Hubble times, unless angular momentum can be lost through some other process.

1.6.2 Final flash

In low to intermediate mass AGB stars when the hydrogen shell is extinguished the star has a final helium shell flash (Renzini 1981, Iben 1983). As the helium shell ignites

the convective zone expands to the surface and ingests the hydrogen. The hydrogen ignites and splits the convective zone in two, helium burning at the bottom of the lower and hydrogen at the bottom of the other. The energy generated by the hydrogen burning shell allows the star to expand to giant dimensions. After the hydrogen has been exhausted in the upper convective zone the ratio $^{12}C/^{13}C\sim$ 3.4 and thus further nuclear processing is required. As the shell is extinguished the two convective zones merge and the excess ^{13}C is transported to hotter regions. There it is burnt via $^{13}C(\alpha,n)^{16}O$, thus increasing the $^{12}C/^{13}C$ ratio.

Although U Aqr is the only known R CrB star with enhanced s-process element abundances it would not be unexpected for others to have similar compositions, so the scenarios must be able to explain this.

In the final thermal pulse scenario the ingestion of ^{13}C into the helium burning shell provides a suitable source of neutrons for s-process enhancement providing that the physical conditions are suitable. During the merging of the white dwarfs ^{13}C material from the HeWD is mixed into the COWD, the degree of mixing controlling the neutron abundance and hence any s-process enhancements.

It is important to state that both scenarios only make qualitative predictions due to difficulties in modelling such complex processes where the nuclear timescale becomes commensurate with the dynamical timescale during merger or convection.

1.7 References

Alexander J.B., Andrews P.J., Catchpole R.M., Feast M.W., Lloyd Evans T., Menzies J.W., Wisse P.N.J., Wisse M., (1972) *Mon. Not. R. astr. Soc.*, **158**, 305

Berman L., (1935) *Astrophys. J.*, **81**, 369

Bond H.E., Luck R.E., Newman M.J., (1979) *Astrophys. J.*, **233**, 205

Bragaglia A., Greggio L., Renzini A., D'Odorico S., (1990) *Ap. J. in press*

Canal R., Isern J., Sanahuja B., (1977) *Astrophys. J.*, **214**, 189

Cottrell P., Lambert D.L., (1982) *Astrophys. J.*, **261**, 595

Danziger I.J., (1965) *Mon. Not. R. astr. Soc.*, **130**, 199

Drilling J.S., Schönberner D., Heber U., Lynas-Gray A.E., (1984) *Astrophys. J.*, **278**, 224

Fadeyev Yu., A., (1986) *In IAU Coll. No.* **87**, *Hydrogen-Deficient Stars and Related Objects,* 441 eds. Hunger, K., Schönberner D. and Rao, N. Kameswara., Reidel

Feast M.W., (1972) *Mon. Not. R. astr. Soc.*, **158**, 11p

Feast M.W., Glass I.S., (1973) *Mon. Not. R. astr. Soc.*, **161**, 293

Feast M.W., (1986) *In IAU Coll. No.* **87**, *Hydrogen-Deficient Stars and Related Objects,* 151 eds. Hunger, K., Schönberner D. and Rao, N. Kameswara., Reidel

Feast M.W., (1990) In: *Confrontation Between Stellar Pulsation and Evolution,* ed. Cacciari C., Bologna, Italy, ASP Conference Series, in press.

Forrest W.J., Gillett F.C., Stein W.A., (1972) *Astrophys. J.*, **170**, L129

Gillett F.C., Blackman D.E., (1986) *Astrophys. J.*, **310**, 842

Giridhan S., Rao N., (1986) *In IAU Coll. No.* **87**, *Hydrogen-Deficient Stars and Related Objects,* 177 eds. Hunger, K., Schönberner D. and Rao, N. Kameswara., Reidel

Glass I.S., (1978) *Mon. Not. R. astr. Soc.*, **185**, 23

Grevesse N. 1984, *Phys., Scr.*, **T8**, 49

Goldsmith M.J., Evans A., (1985) *Ir. Astron. J.* **17**, 308

Hecht J.H., Holm A.V., Donn B., Chi-Chao Wu., (1984) *Astrophys. J.*, **280**, 228

Howarth I.D., (1975) *Acta. Astron.*, **27**, 65

Hunger K., Schonberner D., Steenback W., (1982) *Astr. Astrophys.*, **107**, 93

Iben I. Jr.,, Kaler , Truran and Renzini (1983) *Astrophys. J.*, **264**, 605

Iben I. Jr., Tutukov A.V. (1985) *Astrophys. J. Suppl. Ser.*, **58**, 661

Jones K., Van Wyk F., Jeffery C.S., Marang F., Shenton M., Hill P.W., Westerhuys J.,

(1989) *SAAO Circ.* **13**, 39

Kilkenny D., (1982) *Mon. Not. R. astr. Soc.,* **200**, 1019

Kilkenny D., (1983) *Mon. Not. R. astr. Soc.,* **205**, 907

Kilkenny D., Whittet D., (1984) *Mon. Not. R. astr. Soc.,* **208**, 25

Kilkenny D., Marang F., & Menzies J., (1988) *Mon. Not. R. astr. Soc.,* **208**, 25

Lambert D.L., (1986) *In IAU Coll. No.* **87**, *Hydrogen-Deficient Stars and Related Objects,* 127 eds. Hunger, K., Schönberner D. and Rao, N. Kameswara., Reidel

Lawson W., (1986) *In IAU Coll. No.* **87**, *Hydrogen-Deficient Stars and Related Objects,* 211 eds. Hunger, K., Schönberner D. and Rao, N. Kameswara., Reidel

Lawson W., (1990) *The Characteristics of the Cool Hydrogen Deficient Carbon stars* (thesis) University of Cantabury

Malaney R.A., (1985) *Mon. Not. R. astr. Soc.,* **216**, 743

Menzies J.W., (1986) *In IAU Coll. No.* **87**, *Hydrogen-Deficient Stars and Related Objects,* 207 eds. Hunger, K., Schönberner D. and Rao, N. Kameswara., Reidel

Oke J.B., (1961) *Astrophys. J.,* **133**, 166

O'Keefe J.A., (1934) *Astrophys. J.,* **90**, 294

Orlov M.Ya., Rodriguez M.H., (1974) *Astr. Astrophys.,* **31**, 203

Paczynski B., (1971) *Acta. Astron.,* **21**, 1 Pollacco D.L., Hill P.W., Houziaux L., Manfroid J., (1990) *Mon. Not. R. astr. Soc.,* **248**, 1p

Pollacco D.L., Hill P.W., (1991) *Mon. Not. R. astr. Soc.,* ,

Pugach A.F., (1984) *Sov. Astron.,* **28**, 288

Raveendran A.V., Ashoka B.N., Rao N., (1986) *In IAU Coll. No.* **87**, *Hydrogen-Deficient Stars and Related Objects,* 185 eds. Hunger, K., Schönberner D. and Rao, N. Kameswara., Reidel

Renzini A., 1981 *In Effects of Mass Loss on Stellar Evolution* ed. Chiosi C. and Stalio R., p319

Rosenbush A.E., (1986) *In IAU Coll. No.* **87**, *Hydrogen-Deficient Stars and Related Objects,* 173 eds. Hunger, K., Schönberner D. and Rao, N. Kameswara., Reidel

Saio H., Jeffery C.S., (1988) *Astrophys. J.,* **328**, 714

Saio H., Wheeler J.C., (1985) *Astrophys. J.,* **295**, 38

Schönberner D., (1975) *Astr. Astrophys.,* **44**, 483

Schönberner D., (1977) *Astr. Astrophys.,* **57**, 437

Schönberner D., Heber U., (1986) *In IAU Coll. No.* **87**, *Hydrogen-Deficient Stars and*

Related Objects, 217 eds. Hunger, K., Schönberner D. and Rao, N. Kameswara., Reidel

Searle L., (1961) *Astrophys. J.,* **133**, 531

Soifer et al (1986) *Astrophys. J.,* **304**, 651

Stanford S.A., Clayton G.C., Meade M.R., Nordsieck K.H., Whitney B.A., Murison M.A., Nook M.A., Anderson C.M., (1988) *Astrophys. J.,* **325**, L9

Surendiranath R., Rangarajan N., Rao N., (1986) *In IAU Coll. No.* **87**, *Hydrogen-Deficient Stars and Related Objects,* 199 eds. Hunger, K., Schönberner D. and Rao, N. Kameswara., Reidel

Tempesti P., De Santis R., (1975) *Mem Soc Asta Ital* **46**, 451

Walker H.J., (1986) *In IAU Coll. No.* **87**, *Hydrogen-Deficient Stars and Related Objects,* 407 eds. Hunger, K., Schönberner D. and Rao, N. Kameswara., Reidel

Warner B., (1967) *Mon. Not. R. astr. Soc.,* **137**, 119

Webbink R.F., (1984) *Astrophys. J.,* **277**, 355

Weiss A., (1987a) *Astr. Astrophys.,* **185**, 165

Weiss A., (1987b) *Astr. Astrophys.,* **285**, 178

Chapter 2

Photometry of Hydrogen Deficient Stars

2.1 Introduction

The hydrogen-deficient stars are usually divided into 3 groups — the extreme helium stars (EHe), the R Coronae Borealis stars (R CrB) and hydrogen-deficient carbon stars (HdC). Many of the hydrogen-deficient stars are known to be variable but lack accurate period determinations. This lack of data is principally due the long periods and low amplitudes, typically P> 3 days and $\Delta V < 0.1$. The hotter EHe stars have the best determined periods (see the reviews by Landolt (1986) and Saio and Jeffery (1988)) although the cooler EHe stars are not so well determined (longer periods). The variability of RCr B stars together with periods is summarised in Weiss (1987) but only the brightest object, RY Sgr, has an accurate period (P = 36.2) due to its unusually large amplitude, $\Delta V \sim 0.5$. The HdC stars were thought to be stable until the discovery of variability by Kilkenny *et al.* (1988). Apart from HD 137613, the variations are only $\Delta V \sim 0.07$ and the periods are very uncertain.

The aim is to determine accurate periods of a sample of these objects. If the period is well determined and the mode of pulsation can be identified it will be possible to obtain a distance independent mass for these objects. This provides a good means

of checking the results obtained spectroscopically.

The observations were obtained in collaboration with astronomers from the South African Astronomical Observatory, and the universities of Keele and St.Andrews

2.2 Observations

The 0.5m telescope at SAAO together with the People's Photometer was used to obtain UBV(RI)$_c$ photometry. The variable stars ranged in V magnitude from 7.5 to 12 and since small amplitudes were expected, care had to be taken to ensure accurate photometry. The observing procedure adopted was to observe each variable together with comparison and check stars in the sequence C-V-Ck-V-C. The results for each sequence were averaged and the differential magnitude $\delta(V-C)$ calculated. During each night observations were made of standard stars to enable the differential magnitudes to be tied to the standard system. Each star was observed such that about 100,000 counts were obtained in each colour to obtain a theoretical statistical error of less than 0.1%.

The objects were chosen as follows:

HdC stars Known variables with the largest amplitudes.
HD 137613 and HD 175893.

EHe stars Variability suspected or known with periods in excess of 7 days.
HD 320156, LS IV -1 2, BD -1 3438, PV Tel, BD +1 4381.

R CrB stars As many as possible but particularly known and/or suspected variables, the final selection being determined principally by the requirement that all the objects be well distributed in R.A. in order that best use of the night be made.
UW Cen, Y Mus, DY Cen, S Aps, RT Nor, V CrA and U Aqr.

The observations were taken during a 6 month period during 1988. Further details are given in Table 2.1. Observations were obtained on 65% of the 100 nights awarded, and 41% were clear. From 24^{th} July onwards problems were experienced with dust

in the atmosphere resulting in abnormally high extinction. This persisted throughout the latter part of the observing program although it did improve and remain steady after the initial increase. The most likely explanation is that during this period winds from the N/NW carried dust from the Namib and Kalahari deserts. This period of unusual extinction does not seem to have affected the differential magnitudes, but may be the reason for the slight differences in zero-points between the SAAO and Mount John Astronomical Observatory observations (Lawson *et al.* 1990).

Table 2.1: Observers and dates.

Date	H.J.D. 244000 +	Observer	Nights Clear
April26th – –May2nd	7278–7284	F. Van Wyk	6
May17th – –May23rd	7299–7305	C.S. Jeffery	2
May24th – –June6th	7306–7319	K. Jones	4
June21st – –July11th	7334–7354	M. Shenton	9.5
July19th – –July25th	7362–7368	FVW	4.5
July25th – –Aug1st	7369–7375	F. Marang	3
Aug2nd – –Aug15th	7376–7389	FVW	10
Aug16th – –Aug29th	7390–7403	P.W. Hill	7.5
Sep3rd – –Sep4th	7408–7409	FM	2
Sep27th – –Oct3rd	7432–7438	FVW	2.5

2.3 Reductions

Observations of standard stars during each night were used to fix the nightly zero points for each colour and then were reduced to the standard system using the colour equation of Kilkenny and Marang (1987). Differential magnitudes were then obtained by subtracting the comparison star from the variable star and adding the mean value for the comparison.

Care was taken to ensure that only observations which were consistent with the rest were used, especially in the determination of the mean comparison colours. Criteria for accepting/rejecting data included:

1. large scatter in repeated observation of variable or comparison;

2. missing measurement of comparison star;

3. clearly erroneous measurement of variable or comparison.

2.4 Results

The mean colours for the comparison and check stars are give in Table 2.2 The results for each star are displayed in Figures 1-16. The differential magnitudes and mean comparison colours are given in Appendix A.

PAGE

NUMBERING

AS ORIGINAL

Table 2.2: Standard stars, colours and errors.

Star Name	V	B-V	U-B	V-R	V-I	No. Obs.	Variable
HD 110445	7.089(12)	0.050(07)	0.024(08)	0.026(13)	0.072(10)	15	UW Cen C
HD 110290	8.932(16)	0.868(73)	0.495(67)	0.490(10)	0.959(07)	13	UW Cen Ck
HD 113918	8.668(11)	0.355(06)	0.113(12)	0.213(06)	0.441(07)	19	Y Mus C
HD 113376	8.477(12)	0.730(07)	0.271(11)	0.402(06)	0.783(08)	19	Y Mus Ck
HD 132128	8.154(13)	0.784(08)	0.444(34)	0.450(10)	0.877(09)	32	S Aps C
HD 134011	9.227(14)	0.196(09)	0.178(34)	0.106(07)	0.244(11)	32	S Aps Ck
HD 148311	7.614(12)	0.401(08)	0.126(05)	0.237(05)	0.477(06)	26	RT Nor C
HD 148109	9.148(11)	0.270(07)	0.214(12)	0.144(04)	0.293(06)	24	RT Nor Ck
HD 173659	9.229(13)	0.312(06)	0.086(32)	0.182(05)	0.374(10)	25	V CrA C
HD 173164	9.254(11)	0.404(08)	0.148(38)	0.229(06)	0.452(08)	19	V CrA Ck
HD 209848	9.343(10)	0.106(04)	0.129(07)	0.051(03)	0.109(05)	24	U Aqr C
HD 209277	9.048(76)	0.433(06)	-0.041(06)	0.254(04)	0.504(05)	24	U Aqr Ck
CoD-24 12066	8.775(16)	0.453(05)	0.199(06)	0.256(05)	0.503(06)	19	HD 137613 C
CoD-24 1209	9.633(69)	0.474(70)	0.101(23)	0.281(42)	0.570(82)	15	HD 137613 Ck
HD 176367	8.499(19)	0.565(07)	0.038(07)	0.319(06)	0.624(09)	23	HD 175893 C
HD 176613	8.303(11)	0.366(06)	0.032(05)	0.212(07)	0.428(07)	18	HD 175893 Ck
HD 159652	8.296(10)	0.170(10)	-0.312(10)	0.130(05)	0.288(12)	22	HD 320156 C
HD 320325	9.850(13)	0.554(14)	-0.414(14)	0.379(10)	0.786(20)	17	HD 320156 Ck
HD 162247	9.989(18)	0.363(09)	0.231(08)	0.205(7)	0.431(14)	25	LSIV-1 2 C
HD 162692	7.724(27)	0.331(11)	0.211(13)	0.200(08)	0.415(12)	21	LSIV-1 2 Ck
HD 164760	7.982(26)	0.177(10)	-0.017(09)	0.108(05)	0.241(11)	17	BD-1 3438 C
HD 165196	10.544(40)	0.383(09)	0.245(11)	0.228(06)	0.518(13)	14	BD-1 3438 Ck
HD 167918	7.785(27)	-0.056(09)	-0.470(15)	-0.012(04)	-0.025(14)	36	PV Tel C
HD 168910	9.117(28)	0.355(11)	0.210(10)	0.218(08)	0.453(14)	28	PV Tel Ck
HD 198516	9.263(17)	0.206(09)	0.125(12)	0.111(12)	0.255(27)	24	BD+1 4381 C
BD+0 4598	10.085(14)	0.293(09)	0.196(15)	0.147(06)	0.292(11)	21	BD+1 4381 Ck
HD 116388	7.583(10)	0.068(08)	0.050(07)			35	DY Cen C
HD 116562	9.421(18)	0.270(16)	0.110(14)				DY Cen Ck

The errors shown on each figure were calculated from the standard deviation in the differential magnitude $\delta(Ck-C)$ for each colour. These errors give a good indication of the photometric accuracy obtained over the period of observations. Photon noise statistics were calculated for a typical night (10^{th} July). In all cases these errors were negligible in comparison with the errors due to atmospheric conditions given above. Typically these errors were $\sim$ 0.008 mag, but slightly larger in the colour U-B, $\sim$ 0.010.

Variability was seen in all objects observed although in only some cases were tentative period determinations possible. The R CrB and HdC stars had longer periods than the EHe stars. The amplitudes were in the range 0.1–0.3 mag with the R CrB stars generally being larger.

The paucity of data is such that a Fourier analysis to determine periods is unwarranted and would give rise to spurious periods, of a dubious nature. During this period Lawson *et al.* (1990) observed most of the RCrB and HdC stars. By combining both data sets it may be possible to determine periods more accurately than for either set in isolation. The two sets of observations agree well with only small zero point differences (typically $\Delta V \sim 0.03$). Differences at this level are not unexpected given that different observation techniques, telescopes and locations were used. The zero point shift for each of the sets of data was calculated using the average shift between observations taken at the same time or as close in time as possible. This correction had little effect on the period analysis. Only the data obtained within the same season are used, restricting the possible periods to $P < 100$ days, although some of his objects had observed periods longer than this.

Two independent methods of period determination are used – the classical Fourier power spectrum with PULSAR (Skillen 1985) and phase dispersion minimization (Dworetsky 1983) provided by Dr. P. Hill. Using both methods the data sets were searched for periods lying in the interval 5–50 days. In order to determine the significance of any periods found, the data sets were randomized in magnitude and then re-analysed. The resulting periods and powers are inherent in the data sets and provide a means of discriminating against spurious periods. The power spectra thus obtained are shown in Figures 2.4-2.4, the dashed line showing the randomized power spectrum in each case. The phase dispersion minimization technique gives essentially the same information

Table 2.3: A summary of possible periodicities found in the sample of RCrB and HdC stars.

Star	Frequency	Power	Periods	Noise	Lawson
Y Mus	0.0266	$0.17\text{x}10^{-3}$	37.6	$0.19\text{x}10^{-3}$	107.5
	0.0400	$0.12\text{x}10^{-3}$	25.0		108.7
S Aps	0.0252	$0.14\text{x}10^{-2}$	39.7	$0.57\text{x}10^{-3}$	38.9, 43.1
	0.0362	$0.79\text{x}10^{-3}$	27.6		80.0
V CrA	0.0145	$0.13\text{x}10^{-2}$	69.0	$0.25\text{x}10^{-3}$	57.1
	0.0291	$0.12\text{x}10^{-3}$	34.4		76.9
	0.0410	$0.30\text{x}10^{-3}$	24.4		112.4
U Aqr	0.0239	$0.60\text{x}10^{-3}$	41.8	$0.38\text{x}10^{-3}$	40.2
	0.0352	$0.51\text{x}10^{-3}$	28.4		80.3
	0.0458	$0.57\text{x}10^{-3}$	21.8		
HD 137613	0.0189	$0.22\text{x}10^{-4}$	52.9	$0.12\text{x}10^{-3}$	104.2
	0.0299	$0.21\text{x}10^{-4}$	33.4		109.9
	0.0470	$0.10\text{x}10^{-3}$	21.3		

and an example is shown in Figure 2.4 for S Aps.

The results shown in Figures 2.4-2.4 together with the results of Lawson *et al.* (1990) are summarised in Table 2.3. Each dataset analysed contained around fifty independent observations over a period of 150 days. Therefore the datasets were only searched for periods lying in the interval 20-80 days. It is important to note that the noise level is very close to that of the observed periods in most cases and care must be taken in interpreting the results. Only in the cases where the power in the observations is significantly greater than the power in the randomised data can the derived periods be regarded as real. For example, in the case of V CrA, it would be realistic to assume that a period of $\sim$ 69 days is real as the maximum noise in the spectrum is factor of 5 less than that in the randomized data. Whereas in the case of Y Mus, the maximum power is greater in the random dataset than in the observations dataset, so the periods determined are most likely to be unreal.

UW Cen started fading in the interval H.J.D. 7284-7299, falling from a V magni-

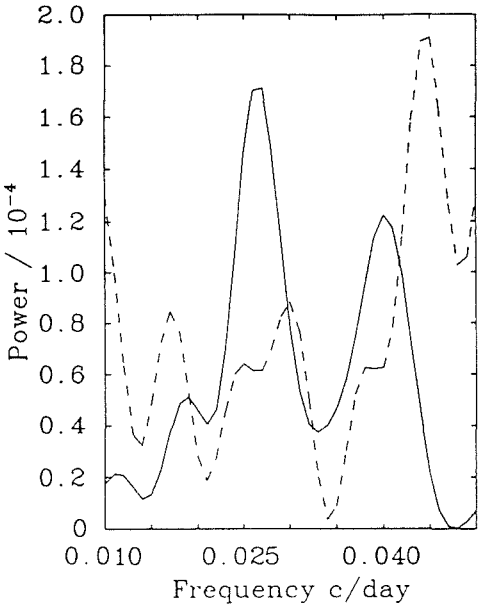

Figure 2.15: The power spectra for Y Mus.

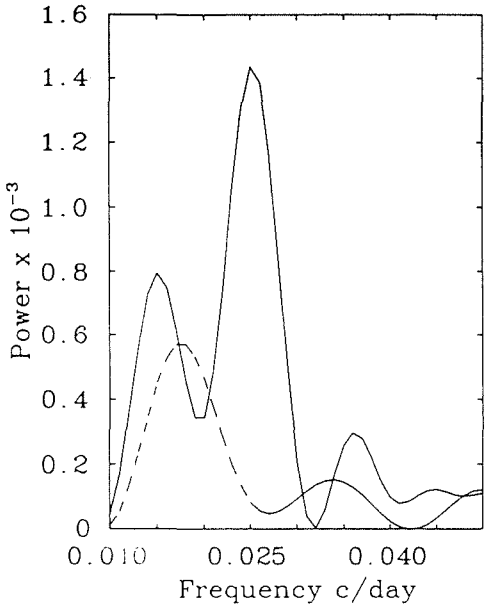

Figure 2.16: The power spectra for S Aps.

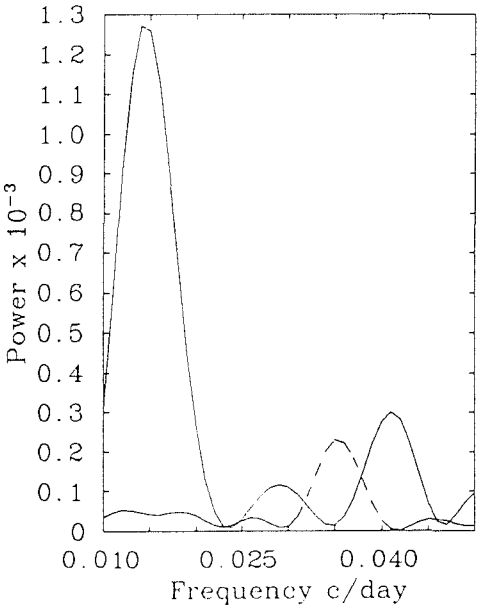

Figure 2.17: The power spectra for V CrA.

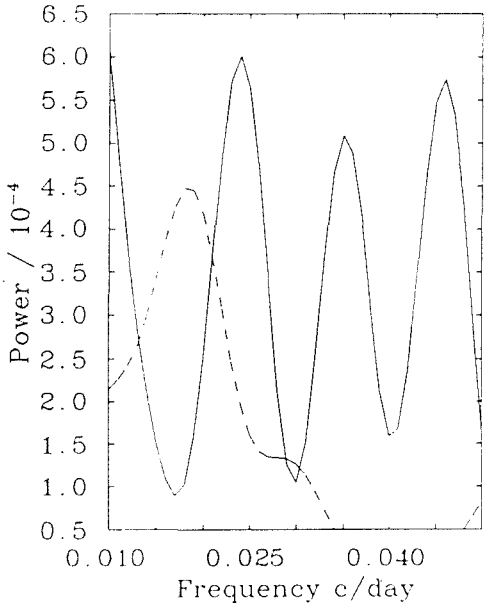

Figure 2.18: The power spectra for U Aqr.

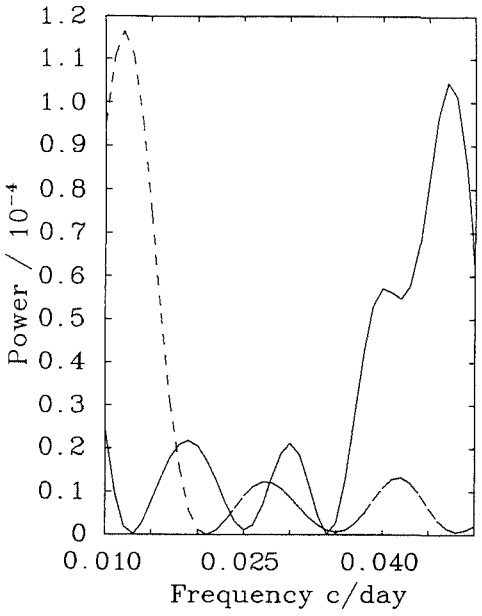

Figure 2.19: The power spectra for HD 137613.

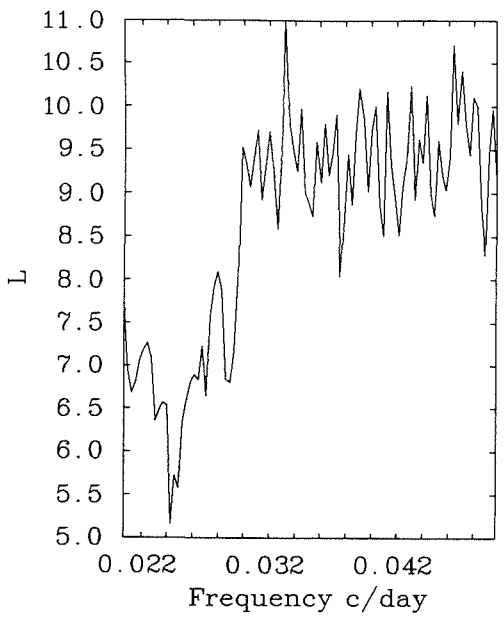

Figure 2.20: The string length for S Aps.

tude of 11.3 to 14.3, becoming progressively redder. Observations were not continued.

2.5 DY Cen and the EHe stars.

Large variations of $\sim$ 0.7 mag in V were seen in DY Cen but the data coverage was poor. All the EHe stars had similar amplitudes of $\sim$ 0.15 – −0.25. Only in the cases of PV Tel and LSIV-1 2 were periods evident, of approximately 8–15 days.

2.6 Conclusion

Variability was observed in all the objects as was expected from the theoretical modelling of Saio and Jeffery (1988) and Weiss (1987). However, conclusive identification of the periods of these objects remains elusive. Theoretical studies have shown that the RCrB and HdC stars are generally only quasi-periodic and thus will need to be observed closely over many cycles to obtain a reasonably precise period. It seems that the only way to achieve such an aim is to use the automatic photometry telescopes and this is being followed by Weiss (1989).

2.7 References

Dworetsky M., (1983) *Mon. Not. R. astr. Soc.*, **203**, 917

Feast M., (1986) *In IAU Coll. No.* **87**, *Hydrogen-Deficient Stars and Related Objects,* p151 eds. Hunger, K., Schönberner D. and Rao, N. Kameswara., Reidel

Kilkenny D., Marang F., & Menzies J., (1988) *Mon. Not. R. astr. Soc.*, **208**, 25

Landolt A., (1986) *In IAU Coll. No.* **87**, *Hydrogen-Deficient Stars and Related Objects,* p51 eds. Hunger, K., Schönberner D. and Rao, N. Kameswara., Reidel

Lawson W., Cottrell P., Kilmartin P., Gilmore A., (1990) *Mon. Not. R. astr. Soc.*, **247**, 91

Saio H., & Jeffery C. S., (1988) *Astrophys. J.*, **328**, 714

Skillen I., (1985) *Fourier analysis of unequally-spaced time series data with applications to the study of helium stars and binary systems,* Ph.D. Thesis, St. Andrews University

Weiss A., (1987) *Astr. Astrophys.*, **185**, 178

Weiss A.,(1989) *private communication.*

Chapter 3

Photometry of DY Cen

3.1 Introduction

DY Cen is an enigmatic star, a cross between the R Coronae Borealis and Extreme Helium stars. DY Cen was observed to undergo RCrB–like minimum (Hoffleit 1930) but has a temperature ($T_{eff} \sim$ 14000K) more typical of the cool EHe stars such as LSE 78. Observations by Kilkenny and Whittet(1986) first indicated that DY Cen may be variable. This was subsequently confirmed by observations by Jones *et al.* (1989), with a tentative period identification by Pollacco and Hill (1991).

Further observations were obtained over a period of four weeks to confirm the presence/absence of the variations observed by Pollacco and Hill (1991).

3.2 Observations

The 0.5m and 1.0m telescopes at the Sutherland observing station of the South African Astronomical Observatory (SAAO) were used to obtain photoelectric Johnson UBV photometry during the period 18^{th} April — 15^{th} May 1989. The 1.0m telescope together with the St. Andrews photometer was used for the first two weeks during bright moon time. For the following fortnight, during dark moon time, the 0.5m telescope with the

Star	V	B-V	U-B	No. Obs.
HD 116562	9.409(9)	0.274(3)	0.108(6)	66
HD 116388	7.584(14)	0.320(15)	-0.652(18)	64
DY Cen	12.779(62)	-0.482(4)	-0.161(7)	64

Table 3.1: Mean differential magnitudes and colour for each star.

dedicated People's Photometer was used.

The 1.0m telescope was used during the period of bright moon to enable observations to be obtained having similar signal-to-noise ratios as those obtained with the 0.5m telescope during the period of dark moon time. In order to obtain a theoretical statistical accuracy of $< 0.1\%$, integration times for U, B and V were 2, 1.5 & 1 minutes.

The observing procedure adopted was to observe the variable, comparison and check star in the following sequence:

$$\text{C} - \text{V} - \text{C} - \text{V} - \text{Ck} - \text{V} - \text{C},$$

interspersed with sky measurements, the frequency determined by the constancy of the sky (*i.e.* , more sky observations during moon-rise and set). The measurements from such a sequence are then averaged and the differential magnitudes, $\delta(V-C)$ and $\delta(C-Ck)$, formed for each colour. Throughout the night observations were obtained of local E–region standards (Menzies *et al.* 1980) which enabled the secondary standards to be tied to the absolute standard system.

3.3 Results

The mean magnitudes and colours and associated errors for each of the observed stars are given in Table 3.1. In the case of the variable and check stars the values are the mean differential plus the mean value of the comparison.

The complete set of observations for each sequence is given in Appendix B. The mean magnitudes and colours of the HD 116562 and DY Cen agree very closely with

those obtained by Pollacco and Hill (1990), lying within both error limits. Due to a mis-identification different check stars were used. Pollacco and Hill (1990) used HD 116700 in preference to HD 116388.

Although the statistical error on any individual measurement, assuming that the errors follow a Poisson distribution, is less than 0.002 mag, a more realistic estimate of the error associated with each *sequence* may be obtained from the error in $\delta(Ck - C)$. This error is significantly greater than the predicted error and is due to the less-than-perfect sky transparency during the time period over which a *sequence* is taken. It is the variation in sky transparency which places a upper limit to the attainable accuracy of photoelectric photometry.

Fig. 3.1-3.3 show the variations in $\delta(V-C)$ and $\delta(Ck-C)$ for each colour. In each case the open symbols represent the (V-C) and the filled symbols (Ck-C). Arbitrary constants have been added to enable both sets of data to be displayed conveniently on the same diagram.

The standard deviation obtained from $\delta(V - C)_V$ is about four times greater than would be expected from purely random fluctuations and this suggests that either DY Cen or HD 116562 may be variable. From inspection of the deviations in the V magnitude of HD 116562 and $\delta(Ck - C)_V$, the conclusion reached is that it is DY Cen which is variable. Similar arguments regarding the presence/absence of variations in the colours B-V and U-B cannot show that DY Cen is variable in either.

3.4 Analysis

The classical power spectrum (Deeming 1975) was calculated for the V colour differential photometry using the Fourier time series analysis program PULSAR (Skillen 1985). The data was searched for frequencies lying in the interval ν =0–0.5 at intervals of $\delta\nu = 0.001$. To determine the validity of periods found in this way the magnitudes were randomized with respect to the observation times and the classical power spectrum calculated. The results of this are shown in Fig. 3.4, the dashed line showing the power spectrum of the randomized data.

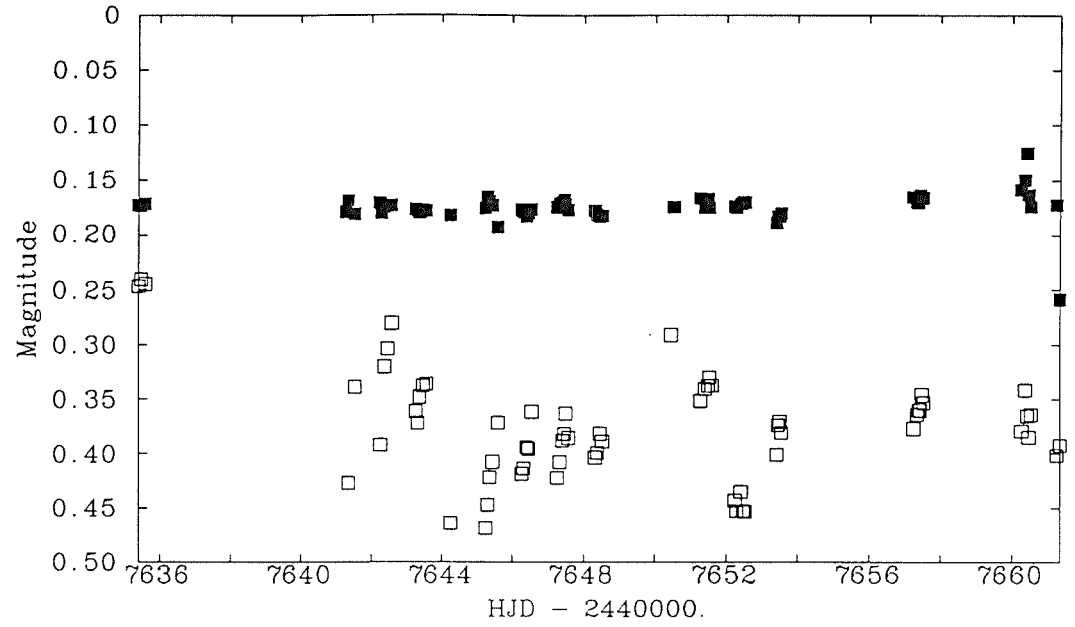

Figure 3.1: The variation in V for DY Cen and associated comparison and check stars.

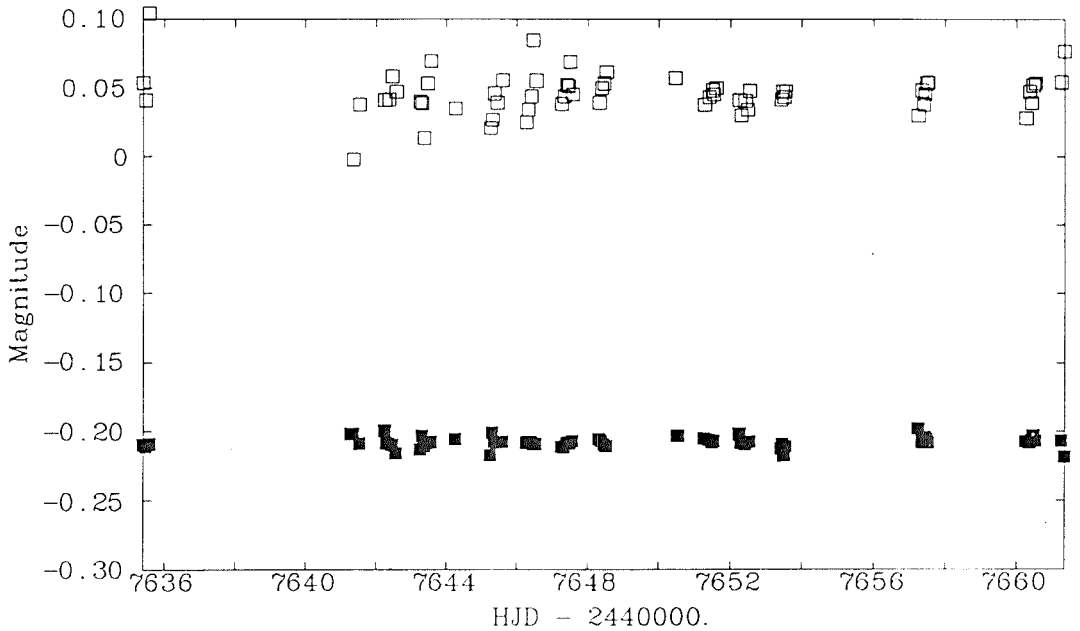

Figure 3.2: The variation in B-V for DY Cen and associated comparison and check stars.

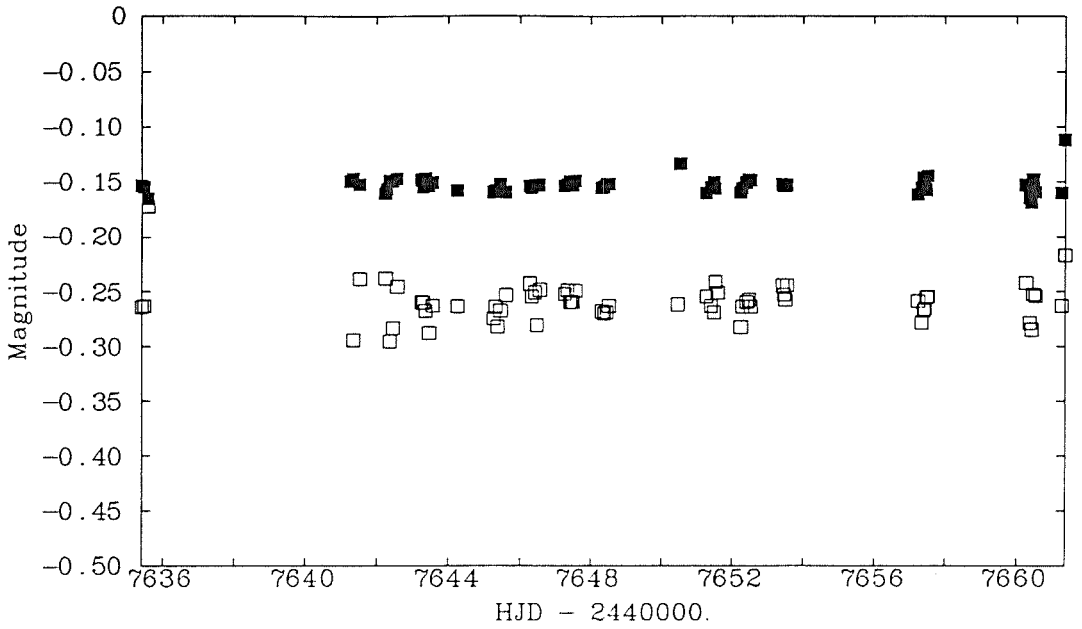

Figure 3.3: The variation in U-B for DY Cen and associated comparison and check stars.

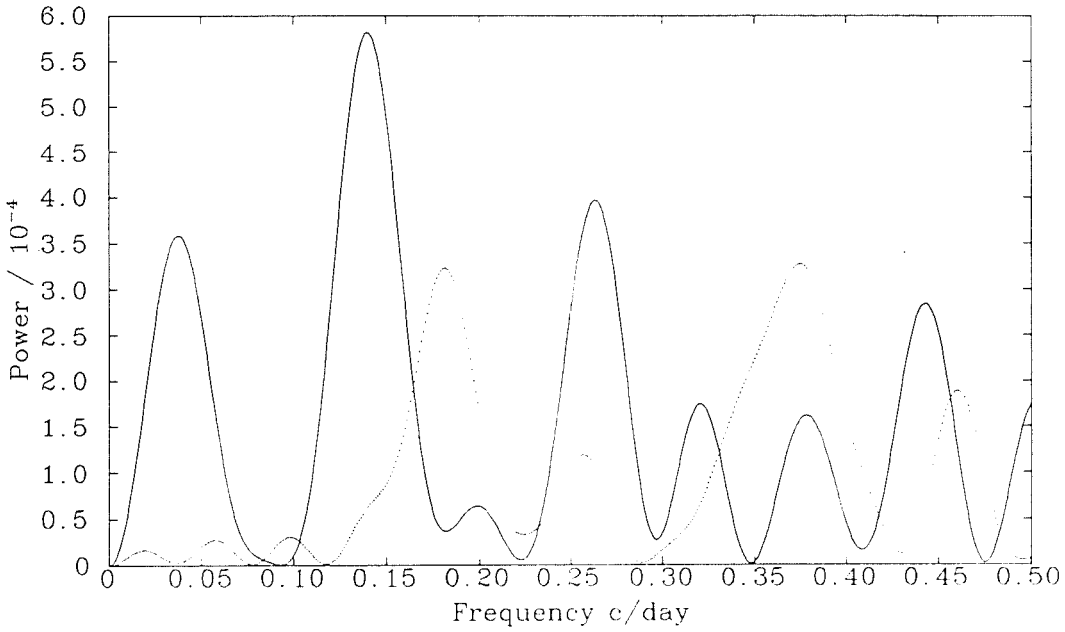

Figure 3.4: The power spectrum of DY Cen, full line and randomized data - dashed line.

The most significant peaks in the power spectrum were:

1. 0.038 c/day (P=26.5 days);
2. 0.140 c/day (P=7.1 days);
3. 0.263 c/day (P=3.8 days).

The long period (P=26.5 days) cannot be regarded as reliable since the observational time-span was only twenty eight days. Furthermore, the amplitude determined by least squares fitting a sinusoidal wave of this period was only $0^{v}.02$. The periods determined by Pollacco (1990) after pre-whitening the data by a period of forty days were:

1. 0.089 c/day (P=11.2 days);
2. 0.182 c/day (P=5.5 days);
3. 0.260 c/day (P=3.8 days).

these being shown in Figures 3.5-3.6. As can be seen from the first figure (Figure 3.5) there is significant power at low frequency. This was removed by pre-whitening the data with a sinusoidal wave of period 40.4 days and amplitude $0^{v}.14$. The effect of removing this is illustrated in the second figure (figure 3.6). Both sets of observations were found to contain variations with periods of 3.8 and 7.1 days, although the latter period is greatly reduced in power after pre-whitening.

The absence of systematic zero-point shifts in either $\delta(V-C)_V$ or C_V makes it worthwhile to combine both datasets and repeat the analysis. The results are shown in Figures 3.7-3.8. Figure 3.7 shows significant power in peaks with periods of 3.8, 7.1 and 40 days and this is consistent with the results obtained from the individual analyses. Figure 3.8 illustrates the effect of pre-whitening each individual data set by its long period (26 and 40 days) and then calculating the power spectrum. This figure clearly shows that the dominant period is that of 3.8 days and is a factor of four stronger than the maximum power in the randomized power spectrum.

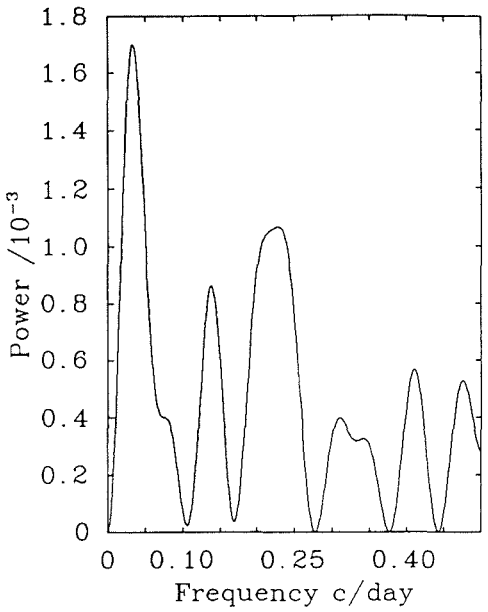

Figure 3.5: The power spectrum of DY Cen from 1987.

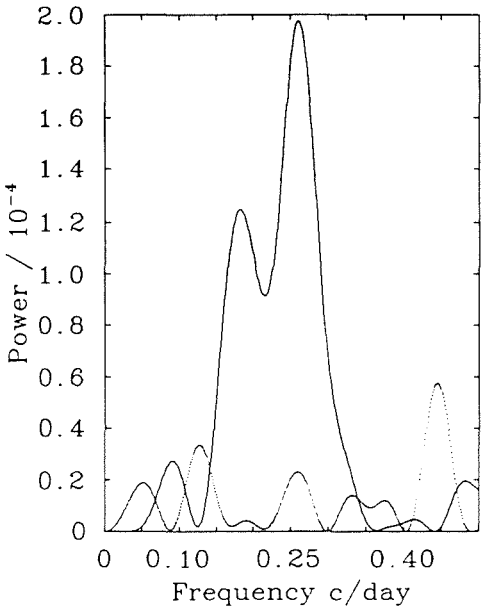

Figure 3.6: The power spectrum of DY Cen from 1987, full line and randomized data - dashed line.

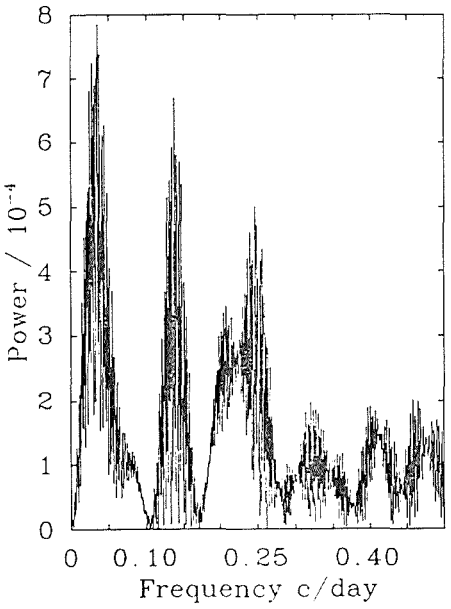

Figure 3.7: The power spectrum of DY Cen with both data sets.

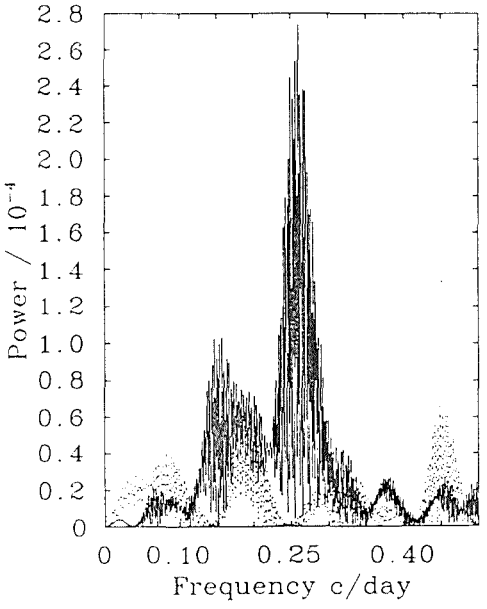

Figure 3.8: The power spectrum of DY Cen with both data sets, prewhitened – full line and randomized dashed line.

3.5 Conclusions

DY Cen is definitely variable with a period of 3.8 days, this period being common to both sets of observations. If DY Cen has an effective temperature of T_{eff} = 14000K (Pollacco and Hill 1990) then this period is consistent with the period-temperature relationship derived by Saio and Jeffery (1989). Moreover, observations of other cool EHe stars have shown them to be only quasi-periodic and this may provide an explanation for the other short periods observed (5.5, 7.1 & 11.2 days). However, it is very difficult to understand the presence of a period in excess of $\sim$ 26 days if DY Cen is a radial pulsator and the large amplitude observed by Pollacco and Hill (1991) makes non-radial oscillations also unlikely. It is therefore important to obtain further observations of DY Cen to search for periods between 2-50 days.

3.6 References

Deeming T.J., (1975) *Astrophys and Space Sci* **36**, 137

Jones (1989) *South African Astronomical Observatory* **13**, 39

Kilkenny D., & Whittet D., (1984) *Mon. Not. R. astr. Soc.,* **208**, 25

Pollacco D., Hill P.W., (1991) *Mon. Not. R. astr. Soc.,* **248**, 572

Menzies J., Blanfield R., Laing J., (1980) *South African Astronomical Observatory* **5**, 149

Saio H., Jeffery C.S. (1988) *Astrophys. J.,* **328**, 714

Skillen W.J., (1985) *Fourier analysis of unequally-spaced time series data with applications to the study of helium stars and binary systems*, Ph.D. Thesis, St. Andrews University

Chapter 4

The Theory of Model Atmospheres

4.1 Introduction

The model atmosphere attempts to describe the physical processes occurring in the upper layers of a star, in which the stellar spectrum is formed. As far as possible the model should be free from *ad hoc* assumptions and provide a self-consistent description. Then using the models and the techniques of spectrum synthesis the fundamental quantities of temperature, gravity and composition may be determined.

Although many different programs have been written to compute model atmospheres (*e.g.* ATLAS - Kurucz (1970), MARCS - Gustafsson (1975) and STERNE - Schönberner (1975)) using a variety of different techniques they are not generally suitable for computing realistic cool hydrogen-deficient atmospheres. Previous attempts to compute such models have used Schönberner's program STERNE which was originally intended to calculate models for hydrogen-deficient B stars. However, although needing no alterations to deal with hydrogen-deficiency, it lacks provisions for dealing with convection or a means of treating line blanketing. Furthermore, the numerical techniques used in solving the transfer equation are limited, giving poor convergence. For these reasons it was decided to adapt the more modern program MARCS which was written

to compute cool atmospheres. It includes the means for dealing with convection and line-blanketing together with a very efficient scheme for solving the transfer equation, although needs adapting for hydrogen-deficiency.

The following chapter outlines the assumptions and theory of *classical* model atmospheres and provides a brief description of how the problem is solved numerically in the program MARCS. A more detailed description of the new equation of state routines which have been written is given.

4.2 Assumptions

It is important to understand the implicit assumptions used in calculating any model in order to understand the inherent model limitations. This section details the assumptions used in calculating model atmospheres using the program MARCS.

The *classical* model atmosphere is static, plane parallel and exists in local thermodynamic equilibrium.

In thermodynamic equilibrium the state of the gas is uniquely determined by the temperature T and particle density N. Local thermodynamic equilibrium (LTE) assumes that the state of the atmosphere is determined by the quantities $T(\mathbf{r})$ and $N(\mathbf{r})$, where $\mathbf{r}$ is the position vector. This is a purely local theory in that neighbouring elements of gas do not interact except through constraints such as radiative and hydrostatic equilibrium. This is an enormous simplification and must be treated with caution. The assumption is known to fail in the cases of high temperatures and low densities when the radiation field couples elements of gas over distances large compare with the electron mean free path. However the alternative, non-LTE, requires the solution of the statistical rate equations for every species which are coupled with all depths, a very difficult problem, in order to calculate the required absorption coefficients. For cool stars this is not possible due to the many contributions to the total absorption coefficient from numerous species and thus LTE is forced upon us.

Although stars are 3-dimensional bodies, provided that the extension of the atmosphere is small compared with its curvature then the surface may be regarded as plane parallel and treated 1-dimensionally.

The atmosphere is considered in be in a steady state. This poses a problem because the process of convection is hydrodynamic in nature and must be taken into account. However, as no adequate hydrodynamic treatment of convection is known the simplified approach of "mixing length" theory will be employed.

The total flux through the star must remain constant, which when convection is not important implies radiative equilibrium.

The presence of rotation and magnetic fields is ignored.

4.3 Radiative Transfer

The formulation and solution of the transfer equation as used in MARCS is taken from Featrier (1964, 1967 and 1968) and is summarised below.

The equation for the transfer of radiation through a gas may be expressed generally as

$$\left[\frac{1}{c}\frac{\partial}{\partial t} + \Omega\nabla\right] I(\mathbf{r}, \Omega, \lambda, t) = \varepsilon(\mathbf{r}, \Omega, \lambda, t) - \chi(\mathbf{r}, \Omega, \lambda, t) I(\mathbf{r}, \Omega, \lambda, t) \qquad (4.1)$$

where

I – specific intensity at $\mathbf{r}$ in direction Ω at wavelength λ,

ε – emission coefficient ($ergscm^{-3}Hz^{-1}s^{-1}$),

χ – extinction coefficient (cm^{-1}).

For the time-independent, plane-parallel atmosphere this simplifies to

$$\mu\frac{dI(\mu, z, \lambda)}{dz} = \varepsilon(\mu, z, \lambda) - \chi(\mu, z, \lambda) I(\mu, z, \lambda) \qquad (4.2)$$

where $\mu = \cos\theta$ is the angle between the ray and the outward normal.

Although this differential equation is just first order, it is nonlinear because both ε and χ are coupled to the radiation field I through the equation of state.

Following Feautrier (1964, 1967 and 1968) the equation is transformed into an equivalent 2 point boundary level problem. Let

$$I_+(\mu, z, \lambda) = I(+\mu, z, \lambda) \tag{4.3}$$

and

$$I_-(\mu, z, \lambda) = I(-\mu, z, \lambda) \tag{4.4}$$

where μ is restricted to the range $0 \leq \mu \leq 1$. Then the symmetric and anti-symmetric sums may be formed as

$$u = \frac{I_+ + I_-}{2} \tag{4.5}$$

and

$$v = \frac{I_+ - I_-}{2} \tag{4.6}$$

Note for clarity the explicit dependence on μ, z and λ has been omitted. From these definitions Eqn. 4.2 becomes

$$\mu \frac{du}{dz} = -\chi v \tag{4.7}$$

$$\mu \frac{dv}{dz} = \varepsilon - \chi u. \tag{4.8}$$

By eliminating v from Eqn. 4.8, we obtain

$$\mu \frac{d}{dz}\left[-\frac{\mu}{\chi}\frac{du}{dz}\right] = \varepsilon - \chi u. \tag{4.9}$$

Define the source function S and the optical depth τ as

$$\frac{\varepsilon}{\chi} = S, \tag{4.10}$$

$$d\tau = -\rho\chi\, dz, \tag{4.11}$$

then we have

$$\mu^2 \frac{d^2 u}{d\tau^2} = u - S. \tag{4.12}$$

The boundary conditions are:

1. Outer boundary $I_- = 0$ so $u = v$ then

$$\mu \frac{du}{d\tau} = u. \tag{4.13}$$

2. Inner boundary, the optical depth is chosen to be large enough for the diffusion approximation to be valid then $u = B$, the Planck function.

From the derivation of Eqn. 4.12 we see that the source function S must be an even function. The source function maybe split into two components, a thermal source and a scattering source. Then

$$S_\lambda = \frac{\sigma_\lambda}{\sigma_\lambda + \kappa_\lambda} \iint R(\lambda, \lambda', \mu, \mu') u(\lambda', \mu')\, d\lambda'\, d\mu' + \frac{\kappa_\lambda}{\sigma_\lambda + \kappa_\lambda} B_\lambda(T) \tag{4.14}$$

where $R(\lambda, \lambda', \mu, \mu')$ is the redistribution function and σ_λ and κ_λ the scattering and absorption coefficients respectively. These are related to the extinction coefficient χ_λ by

$$\chi_\lambda = \sigma_\lambda + \kappa_\lambda. \tag{4.15}$$

For the continuum the scattering is essentially coherent, *i.e.*, $\lambda = \lambda'$ and we make the additional assumption that the scattering is isotropic, *i.e.*, independent of μ. Thus the scattering term in Eqn. 4.14 reduces to

$$\frac{\sigma_\lambda}{\sigma_\lambda + \kappa_\lambda} \int_0^1 u\, d\mu = \frac{\sigma_\lambda}{\sigma_\lambda + \kappa_\lambda} J_\lambda. \tag{4.16}$$

4.4 Hydrostatic Equilibrium

Following the assumption of a static atmosphere, the pressure gradient must balance the gravitational force so

$$\frac{dP}{dz} = -g\rho \tag{4.17}$$

where g is the surface gravity. From the above definition of optical depth Eqn. 4.17 becomes

$$\frac{dP}{d\tau} = \frac{g}{\chi}. \tag{4.18}$$

The pressure may be split into two components, the gas and radiation pressures

$$P = P_g + P_r \tag{4.19}$$

where the radiation pressure is given by

$$P_r = \frac{4\pi}{c} \sigma T_{eff}^4. \tag{4.20}$$

4.5 Radiative Equilibrium and Flux Constancy

In LTE radiative equilibrium maybe expressed as

$$\int_0^\infty \chi_\lambda J_\lambda \, d\lambda = \int_0^\infty \chi_\lambda B_\lambda \, d\lambda \tag{4.21}$$

where J is the angle-averaged intensity

$$\int_0^1 u \, d\mu = J \tag{4.22}$$

and $B_\lambda(T)$ the Planck function. However, this equation is only valid when radiative transfer is the dominant energy transport process, and the convective flux, F_c, is negligible. More generally we insist that the total flux remain constant

$$F_c + \int_0^\infty v \, d\lambda = \sigma T_{eff}^4. \tag{4.23}$$

4.6 Convective Flux

As stated earlier, convection is a hydrodynamic process which cannot currently be modelled.Thus a simplified empirical approach is used — mixing length theory. The prescription used in MARCS is that given by Nordlund (1974) and is briefly outlined below.

The atmosphere becomes unstable to convection when the temperature gradient ∇ becomes greater than the adiabatic temperature gradient ∇_{ad} — Schwarzschild's instability criterion. Then following Nordlund (1974) the convective flux and related quantities are given by

$$\pi F_c = \frac{1}{2}\rho C_p T v \frac{l}{H} \Delta\nabla \tag{4.24}$$

where

C_p – specific heat at constant pressure,

v – convective velocity,

l – mixing length typically $1 - 2H$,

H – scale height of atmosphere,

$\Delta\nabla$ – the difference between the two gradients.

The convective velocity is given by

$$v = \frac{l}{H}\left[\frac{gQH}{k}\Delta\nabla\right]^{1/2} \tag{4.25}$$

Q relates the density fluctuations to temperature fluctuations and is given by

$$Q = -\frac{T}{\rho}\left[\frac{\partial\rho}{\partial T} - \frac{\partial\rho}{\partial P_e}\frac{\partial P}{\partial T}\Big/\frac{\partial P}{\partial P_e}\right] \tag{4.26}$$

and $\Delta\nabla$ by

$$\Delta\nabla = \frac{\gamma}{\gamma+1}[\nabla - \nabla_{ad}]\,. \tag{4.27}$$

The convective efficiency γ is

$$\gamma = \frac{v\rho C_p(1 + c(\chi l)^2)}{8\sigma T^3 \chi l}. \tag{4.28}$$

The constant k is characteristic of the rate of energy dissipation by turbulent viscosity and was set to 8; c is determined by the temperature structure within the convective element and was chosen to be 0.076, the value corresponding to the temperature structure formed if the diffusion approximation is used.

4.7 Equation of State

The equation of state determines the physical state of the atmosphere and is controlled by radiative and collisional processes. In general this is an extremely difficult problem to solve since the statistical rate equations which determine the occupancy of each energy level for each species must be solved simultaneously with the transfer and constraint equations. However, the assumption of LTE allows this problem to be greatly simplified as now the occupancy of the energy levels is determined by the local temperature only. Given the local temperature the state of the gas may be calculated using Saha's equation and the Boltzmann excitation equation. This assumption is valid when the temperature gradient $dT/d\tau$ is small and when collisional processes dominate radiative processes.

In addition to ionization, in cool atmospheres molecular formation must also be considered. This has two effects; it reduces the atmospheric pressure and contributes to the continuous opacity. Only at very low temperatures ($<$ 3000K) is the degree of molecular formation large enough to significantly alter the gas pressure and these temperatures are smaller than those found in the cool hydrogen-deficient atmospheres.

Once the degree of ionization and the molecular pressures have been calculated then the various contributions to the continuous opacity may be obtained. The physics involved in the equation of state is obviously independent of the composition of the atmosphere. Altering the composition merely changes the degree of ionization and molecular formation.

In normal stars with solar compositions, the composition is dominated by hydrogen, all other elements being at least a factor of ten less abundant. Hydrogen also provides the largest contribution to the gas pressure and continuous opacity. Thus when the abundance of a species, X, is determined it is the ratio X/H which is obtained. As a consequence, the composition is defined relative to hydrogen. The number density of hydrogen, N_H, is defined as

$$\log N_H = 12 \tag{4.29}$$

and the relative fractional abundance of element X, n_X as

$$n_X = \frac{N_X}{N_H}. \tag{4.30}$$

From this definition, the relative fractional abundance of hydrogen is unity and the sum of the fractional abundances is

$$\sum_{allX} n_X \sim 1.15 \tag{4.31}$$

for a solar composition.

This method of defining the composition is not suitable for the hydrogen-deficient stars as they have helium as the most abundant element and carbon dominates the continuous opacity. Although it would be possible to define the fractional abundances relative to helium or possibly carbon this would make it impossible to calculate normal (solar) composition models.

Following Schönberner (1975), it was decided to define the fractional abundances relative to the total abundance of all the elements present in the atmosphere. So the fractional abundance of element X is

$$n_X = \frac{N_X}{\sum_{allX} N_X}. \tag{4.32}$$

Using this definition, solar abundances have

$$n_H \sim 0.9,\ n_{He} \sim 0.09 \text{ and } n_Z \sim 0.01$$

and hydrogen-deficient compositions

$n_H \sim 0.001$, $n_{He} \sim 0.95$, $n_C \sim 0.04$ and $n_Z \sim 0.009$.

The relative fractional abundances are then scaled such that

$$\log \sum_{allX} a_X.N_X = 12.15, \tag{4.33}$$

where a_X is the atomic weight of element X. This choice of scaling allows direct comparison with the solar composition using the earlier definition of relative abundances and effectively compares the relative abundances of a unit mass of atmosphere.

As stated earlier, altering the way in which the composition of the atmosphere is defined has no effect on the physics. However, it does alter the way in which some of the equations are solved and the scaling of the opacity contributions. In particular the equations governing molecular formation must be rephrased and a different approach to solving them used. This is detailed in the next section. The opacity calculations provide the opacity per unit species and therefore need to be scaled by the number of the species present in the atmosphere at that particular depth. This scaling is obtained from the gas pressure and is given by

$$N_X = n_X.\frac{(P_g - P_e)}{K_B T}. \tag{4.34}$$

The ionization energies used in solving Saha's equation were taken from the general literature. The partition functions used were those calculated by Traving *et al.* (1966), Baschek *et al.* (1966) and Fischel and Sparks (1971). Although these partition functions are temperature dependent, their variation over the range of temperatures present in the model atmospheres was insignificant and they were treated as constants.

4.7.1 Molecular Formation

For late type stars molecular formation must be taken into account due to the large contribution molecular species make to the continuous opacity in the outer layers of the atmosphere. The most abundant molecules expected in hydrogen-deficient atmospheres will be those containing the elements H, C, N and O. The molecules considered were H_2, H_2^+, H^-, H_2O, OH, CH, CO, CN, C_2, N_2, O_2, NO, NH, C_2H_2, HCN, C_3H and C_3.

In equilibrium, the molecular partial pressure of species xyz is given by the equation

$$\frac{P_x P_y P_z}{P_{xyz}} = K_{xyz}(T), \tag{4.35}$$

where P_x, P_y and P_z are the atomic partial pressure of the molecules constituents and $K_{xyz}(T)$ is the dissociation constant at temperature T. There is one such equation for each molecular species considered. The dissociation constants were obtained from calculations by Tsuji (1973).

The total number of atoms of a species must remain constant in the atmosphere and this gives rise to a conservation equation for each atomic species. For the species carbon the conservation equation is given by

$$\begin{aligned} C &= P_C + P_{CH} + P_{CO} + P_{CN} + 2.P_{C_2} \\ &\quad + 2.P_{C_2H_2} + P_{HCN} + 3.P_{C_3H} + 3.P_{C_3} \end{aligned} \tag{4.36}$$

where C is the partial pressure of carbon in the absence of molecular formation. The molecular partial pressures in the conservation equation are eliminated using the equilibrium equations:

$$\begin{aligned} C &= P_C + \frac{P_C.P_H}{K_{CH}} + \frac{P_C.P_O}{K_{CO}} \\ &+ \frac{P_C.P_N}{K_{CN}} + \frac{2.P_C^2}{K_{C_2}} + \frac{2.P_{C_2H_2}}{K_{C_2H_2}} \\ &+ \frac{P_H.P_C.P_N}{K_{HCN}} + \frac{3.P_C^3.P_H}{K_{C_3H}} + \frac{3.P_C^3}{K_{C_3}}. \end{aligned} \tag{4.37}$$

The conservation equations are of the general form

$$F_j(x_i) = 0 \tag{4.38}$$

where $x_i = (P_H, P_C, P_N, P_O, P_e)^T$ and are nonlinear in the atomic partial pressures. The electron pressure is included due the presence of the molecules H_2^+, H_2^- and H^-. The method of solution for coupled nonlinear equations is to use a generalised form of the Newton-Raphson method. For a single nonlinear equation the solution is obtained by iterating the equation

$$x^{n+1} = x^n - \frac{F(x^n)}{F'(x^n)} \tag{4.39}$$

where $F'(x^n)$ is the derivative of F with respect of x, until the required accuracy is obtained. In the case of coupled equations this equation is transformed from the scalar equation into the vector equation

$$\mathbf{x}_i^{n+1} = \mathbf{x}_i^n - \frac{F_j(\mathbf{x}_i^n)}{F_j'(\mathbf{x}_i^n)}. \tag{4.40}$$

Although the derivatives may be evaluated using finite differences it is both computationally faster and more accurate to evaluate them analytically. The matrix of derivatives of a function with respect to each of the independent variables is called the Jacobian matrix. For example the row corresponding to the carbon conservation equation has elements:

$$\frac{\partial F_C}{\partial P_H} = \frac{P_C}{K_{CH}} + \frac{P_C.P_N}{K_{HCN}} + \frac{3.P_C^3}{K_{C_3H}} + \frac{4.P_H.P_C}{K_{C_2H_2}}, \tag{4.41}$$

$$\begin{aligned} \frac{\partial F_C}{\partial P_C} &= 1 + \frac{P_H}{K_{CH}} + \frac{P_N}{K_{CN}} + \frac{P_O}{K_{CO}} \\ &+ \frac{P_H.P_N}{K_{HCN}} + \frac{4.P_C}{K_{C_2}} + \frac{4.P_C.P_{H_2}}{K_{C_2H_2}} \\ &+ \frac{9.P_C}{K_{C_3}} + \frac{9.P_C.P_H}{K_{C_3H}}, \end{aligned} \tag{4.42}$$

$$\frac{\partial F_C}{\partial P_N} = \frac{P_C}{K_{CN}}, \tag{4.43}$$

$$\frac{\partial F_C}{\partial P_O} = \frac{P_O}{K_{CO}}, \tag{4.44}$$

and

$$\frac{\partial F_C}{\partial P_e} = 0. \tag{4.45}$$

This method needs an initial guess at the solution which was taken to be the atomic partial pressures in the absence of molecules. This starting solution proved reliable as the molecular partial pressures were always small in comparison to the atomic partial pressures and therefore the starting solution was never far from the final solution.

4.7.2 Continuous Opacity

The basic algorithm for calculating the continuous opacity is taken from MARCS (Gustafsson 1973). This contained most of the sources of continuous opacity necessary for calculating cool hydrogen-deficient model atmospheres. These routines needed

no alterations to take into account the change in definition of the fractional abundance of the elements other than the scaling mentioned above.

The sources of opacity and their origins are:

H^-	Doughty *et al.* (1966) and Doughty and Fraser (1966)
H bound-free & free-free	Karzas and Latter (1961)
H_2 & H_2^+	Mihalas (1965)
H_2^-	John (1975)
He I, C I, Mg I, Al I, Si I	Peach (1970)

In atmospheres with solar compositions the hydrogen species totally dominate the contributions to the continuous opacity with the other sources of only minor importance. However in hydrogen-deficient compositions, all these sources have approximately equal importance, the metals, in particularly C I, dominating in the visual region. As the total continuous opacity is greatly reduced in the hydrogen-deficient atmospheres the temperature becomes greater at any given depth and as a consequence it was necessary to include contributions from C II, N I, N II, Mg II, Si II, Ca I and Ca II (Peach 1970).

4.7.3 Line opacity

Although the individual line opacity of most metal lines is small in comparison with other contributions, the large number of such lines and their close proximity create a quasi–continuous opacity source. This is line blanketing, important for early type stars in the ultra–violet and for late types in the visual region. Note that in the visual region molecular lines also become important.

In theory it is possible to take into account the wavelength variation of line opacity, but the resulting large number of frequency points would result in prohibitive computational costs. The solution has been to replace the rapid variation of line opacity with frequency with a statistical measure of the line opacity over some interval large

compared to that of an individual line. The simplest are mean or harmonic mean line opacities (Carbon 1974). A more accurate approach is that based upon the opacity distribution functions, ODF (Strom and Kurucz 1966). This is the approach used by Gustaffson *et al.* (1975).

Within the the wavelength interval $\lambda, \lambda + \Delta\lambda$ the opacity distribution function $F(l_\lambda)$ is calculated such that

$$F(l_\lambda)\, dl_\lambda \tag{4.46}$$

is the fraction of line opacity lying in the interval l, $l + dl$ and hence

$$\int_0^\infty F(l_\lambda)\, dl_\lambda = 1. \tag{4.47}$$

Given the distribution function and the total opacity over the wavelength interval *giant* lines may be constructed at sub-intervals. Obviously this is just the same as using a mean opacity if the number of sub-intervals is one. The visible region from 3000-7200Å was divided up into 42 intervals of 100Å each with four sub-intervals forming the *giant* line. To prevent systematic errors in the emergent flux the opacity distribution functions were reversed alternatively (failure to do this either leads to models too red or too blue). Redwards of 7200Å the distribution functions only considered molecular opacities from the CO and CN bands. The spacing of frequency points was determined by the grid of frequency points used by MARCS in the transfer equation.

4.8 Numerical Solution of Model Atmospheres.

Although the transfer equation (Eqn. 4.2) may be solved exactly given the source function S, an iterative scheme is needed if the solution is to satisfy simultaneously the constraint equations (Eqn. 4.17 & 4.21). The approach MARCS uses is a modification of Mihalas's technique of complete linearisation (Mihalas 1978). Although originally used to solve the more complex case of NLTE model atmospheres, a simplified approach with only partial linearization has been shown to be extremely efficient for LTE atmospheres (Gustafsson *et al.* 1975). In this case the opacity is not linearized.

Firstly, the continuous variables μ, λ and τ are approximated by discretisation.

$$\begin{aligned} \mu_m, &\quad \mu_1, \ldots, \mu_M \\ \lambda_n, &\quad \lambda_1, \ldots, \lambda_N \\ \tau_d, &\quad \tau_1, \ldots, \tau_D \end{aligned} \tag{4.48}$$

The differential operators are represented as difference equations and the integrals as quadrature sums. Then following Rybicki (1971) the independent variables are grouped by depth to form vectors, *i.e.*,

$$\mathbf{u}_i = (u_{i1}, \ldots, u_{iD})^T \quad i = m + n \tag{4.49}$$

.

Although the grouping of the independent variables has no effect on the final solution it does affect the time taken to solve it. This method is superior to Feautrier's original method when $I \gg D$ as is the case for a realistic atmosphere where many angle-wavelength points are needed to describe the radiation field.

The transfer and constraint equations (Eqn. 4.2, 4.17 & 4.21) are linearized in the dependent variables $T, P, P_e, P_{rad}, F_\lambda, F_{conv}$, and mean intensity u, giving a set of linear equations to be solved. The radiative part is then solved using Rybicki's method (see Gustafsson and Nissen 1972). Then the perturbations, ∂u and F_λ are eliminated from the linearized equations (Eqn. 4.21 and 4.23) and the remaining system of equations is solved using Gaussian elimination to obtain the dependent variable corrections at each depth.

The initial solution is usually that of a grey atmosphere with the temperature structure given by

$$T^4 = \frac{3}{4}(\tau + 3^{-1/2})T_{eff}^4 \tag{4.50}$$

although in some cases, near the Eddington limit, a rescaled model is more appropriate. The rate of convergence is usually second order with 4 to 8 iterations required to compute a model such that the maximum temperature change $\partial T < 1K$.

4.9 Spectrum Synthesis

The calculated model atmosphere must be related to the real world of observations. The observations consist of measurements of line profiles and/or equivalent widths of absorption lines from the stellar photosphere.

We can formally integrate the transfer equation (Eqn. 4.2) provided that the source function is known. Then the specific intensity at the surface ($\tau_\lambda = 0$) is

$$I_\lambda(0,\mu) = -\frac{1}{\mu}\int_0^\infty S_\lambda(\tau_\lambda)e^{-\tau_\lambda/\mu}d\tau_\lambda. \tag{4.51}$$

By further integrating over the angle μ to obtain the flux we obtain

$$F_\lambda(0) = \frac{1}{2}\int_{-1}^{1}\mu d\mu\int_0^\infty -\frac{1}{\mu}S_\lambda(\tau_\lambda)e^{-\tau_\lambda/\mu}d\tau_\lambda. \tag{4.52}$$

This integral is more normally written as

$$F_\lambda = 2\int_0^\infty S_\lambda(\tau_\lambda)E_2(\tau_\lambda)d\tau_\lambda \tag{4.53}$$

where E_2 is the second exponential integral defined as

$$E_n(x) = \int_1^\infty w^{-n}e^{-xw}dw. \tag{4.54}$$

We define the residual flux R_λ as the ratio of line to continuum flux,

$$R_\lambda = \frac{F_l(\lambda)}{F_c(\lambda)}, \tag{4.55}$$

where the fluxes are calculated using Eqn. 4.53. This equation gives us the normalised line profile which may then be related to the equivalent width, W, by

$$W_\lambda = \int 1 - \frac{F_l}{F_c}d\lambda. \tag{4.56}$$

As was stated earlier we have assumed that the source function is known. This is only true if we assume LTE and then the source function is the Planck function at the local temperature.

The program SSG (Bell 1973) is used to carry out the spectrum synthesis. It is sufficiently general as to enable it to deal with the case of hydrogen-deficiency. Slight modifications have been made to also enable it to calculate equivalent widths.

4.10 Programs

Both programs MARCS and SSG were obtained through Collaborative Computational Project No. 7 (CCP7) and SSG is used with the permission of the author Dr. R. Bell.

4.11 References

Baschek B., Holweger H., Traving G.,, (1966), *Astr. Abh. Hamb. Sternw. Bergedorf* **VIII**,26

Bell R., (1973) *Mon. Not. R. astr. Soc.,* **164**, 197

Carbon D., (1974) *Astrophys. J.,* **187**, 135

Doughty N., Fraser P., McEachran R., (1966) *Mon. Not. R. astr. Soc.,* **132**, 255

Doughty N., Fraser P., (1966) *Mon. Not. R. astr. Soc.,* **132**, 267

Feautrier P., (1964) *C. R. Acad. Sci. Paris* **258**,3189

Feautrier P., (1967) *Ann. d'Astrophys***30**, 125

Feautrier P., (1968) *Ann. d'Astrophys* **31**,257

Fischel D., Sparks W., (1971) *Astrophys. J.,* **164**, 351

Gustafsson B., Bell R.,Erikson K., & Nordlund A., (1975) *Astr. Astrophys.,* **42**, 402

Gustafsson B., (1973) *Uppsala Astron. Obs. Ann.* **5**, No.6

John T.L., (1975) *Mon. Not. R. astr. Soc.,* **170**, 5

Karzas W., Latter R., (1961) *Astrophys. J. Suppl. Ser.,* **VI**, 167

Kurucz R.L., (1970) *SAO Spec Rep. No.* **309**

Mihalas D., (1965) *Astrophys. J. Suppl. Ser.,* **IX**, 321

Mihalas D., (1978) *Stellar Atmospheres*

Nordlund Å., (1974) *Astr. Astrophys.,* **32**, 407

Peach G., (1970) *Mem. Roy. Astron. Obs. Soc.,* **73**, 1

Rybicki G., (1971) *J. Quant. Spectrosc.. Radiat. Transfer* Vol **11**, 589

Strom S. & Kurucz R., (1966) *J. Quant. Spectrosc.. Radiat. Transfer* Vol **6**, 591

Traving G., Baschek B., Holweger H., (1966) *Astr. Abh. Hamb. Sternw. Bergedorf* **VIII**, 1

Traving G., (1973) *Astr. Astrophys.,* **23**, 411

Tsuji T., (1973) *Astr. Astrophys.,* **23**, 411

Chapter 5

Models for Hydrogen-Deficient Atmospheres

5.1 Introduction

In this chapter model atmospheres are presented suitable for use in analysing the cool hydrogen-deficient carbon stars and R CrB stars. The original program as written by Gustafsson and Nordlund (MARCS) is compared with the adapted version (KMARCS). Firstly normal composition models (*i.e.* , with solar abundances) are calculated to allow the rewritten equation of state routines to be compared with the originals, verifying that they are correct.

Hydrogen-deficient models are then presented and compared with equivalent hydrogen-rich models to highlight the differences and similarities. These hydrogen-deficient models are then compared with models from Schönberner's program STERNE (Schönberner 1975).

Finally, the assumptions used in creating the models are reviewed and the validity of the models established.

Element	Log Abundance	Percentage Abundance
H	12.00	90.80
He	11.00	9.08
C	8.55	$2.94\text{x}10^{-2}$
N	7.93	$7.05\text{x}10^{-3}$
O	8.77	$4.88\text{x}10^{-2}$
Ne	8.51	$2.68\text{x}10^{-2}$
Na	6.18	$1.25\text{x}10^{-4}$
Mg	7.48	$2.50\text{x}10^{-3}$
Al	6.40	$2.08\text{x}10^{-4}$
Si	7.55	$2.94\text{x}10^{-3}$
S	7.21	$1.34\text{x}10^{-3}$
K	5.05	$9.29\text{x}10^{-6}$
Ca	6.33	$1.77\text{x}10^{-4}$
Cr	5.47	$2.44\text{x}10^{-5}$
Fe	7.50	$2.62\text{x}10^{-3}$
Ni	5.08	$9.96\text{x}10^{-6}$

Table 5.1: Composition used for producing solar type atmospheres.

5.2 Equation of State

It is essential that the equation of state routines, which have been generalised to enable unusual compositions to be dealt with, are rigorously checked against the original versions — the calculated thermodynamic variables must be exactly the same. In the first part of this section results are presented to show that this has been achieved. The composition used is essentially solar with the abundances given in Table 5.1.

5.2.1 Gas Pressure

The gas pressure is calculated by solving Saha's equation for a given temperature and electron pressure. The results are shown in Figures 5.1-5.2 for a range of temperatures. The differences in results from the two sets of equation of state routines are negligible.

The differences found are due to the differing word length used in the calculations (32 bits on DEC VAX for MARCS and 64 bits on a CRAY XMP4/16 for KMARCS).

Figure 5.2 shows the internal energy as calculated by KMARCS. This cannot compared with the value returned by MARCS since there appears to be an error in its calculation; MARCS returns a negative internal energy. The internal energy consists of three components — kinetic, ionization and molecular association. Neglecting the molecular component the internal energy U is given by

$$U = \frac{3}{2}(N_i + N_e)k_B T + \sum_{j=2} N_{ij}\chi_{ij}$$

where N_{ij} is the number of atoms of species i, in ionization stage j (ground state $j = 1$)and N_e the number of electrons. MARCS incorrectly calculates the ionization component using the number of hydrogen atoms in the ground state times the ionization energy rather than the number in the first ionization stage times the ionization energy. There is also an incorrect sign. Thus the results obtained are typically of the order -10^{13} ergs/cm^3 instead of 10^{11} ergs/cm^3.

The internal energy is important in calculating the convective flux (see Chapter 4) so the MARCS models will be unreliable when the convective flux becomes large enough to start altering the structure of the atmosphere.

5.2.2 Molecular formation

At the temperatures for which model atmospheres are required (*i.e.* , 5000–8000K) the molecular partial pressures are too low to affect the pressure equations, being typically 10^{-4}% of the total pressure. The only effect of molecular formation is in the calculation of the continuous opacity. The species used are $H^-, H_2,$ andH_2^+, CO and CN in the opacity distribution functions. Figure 5.3 shows the variation of molecular partial pressures together with the partial pressure of hydrogen for comparison. Again, the agreement between the two programs is excellent, even though different methods are used to solve the conservation equations.

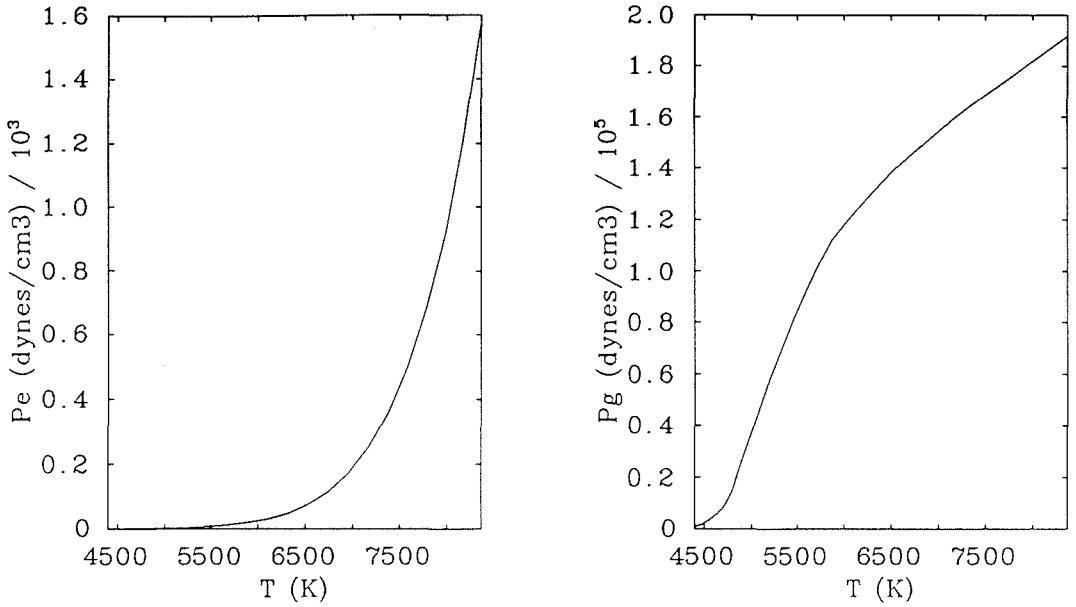

Figure 5.1: The electron and gas pressures as functions of temperature.

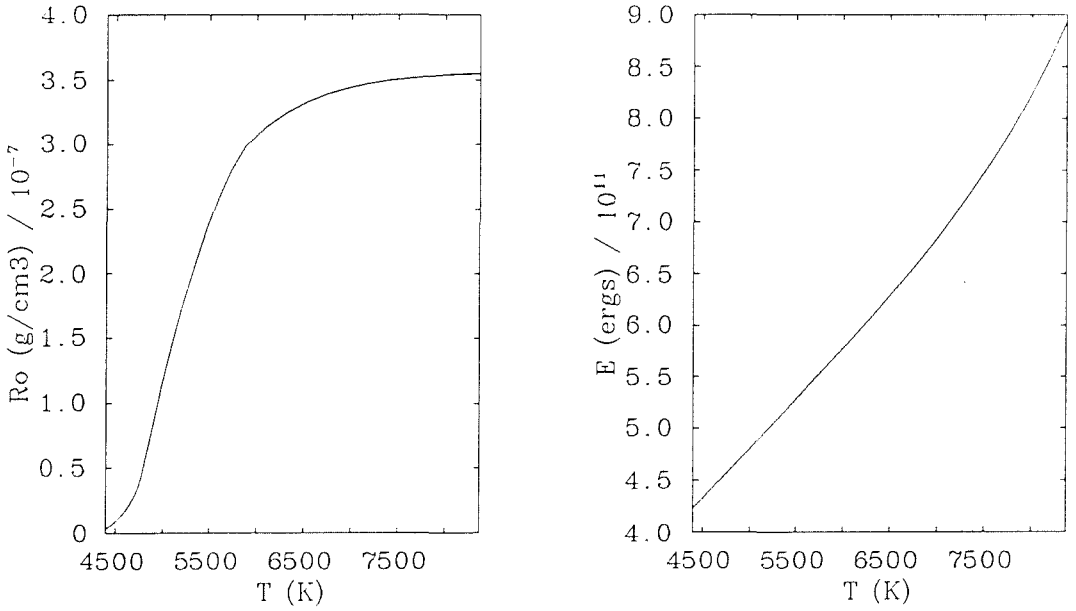

Figure 5.2: The density and internal energy as functions of temperature.

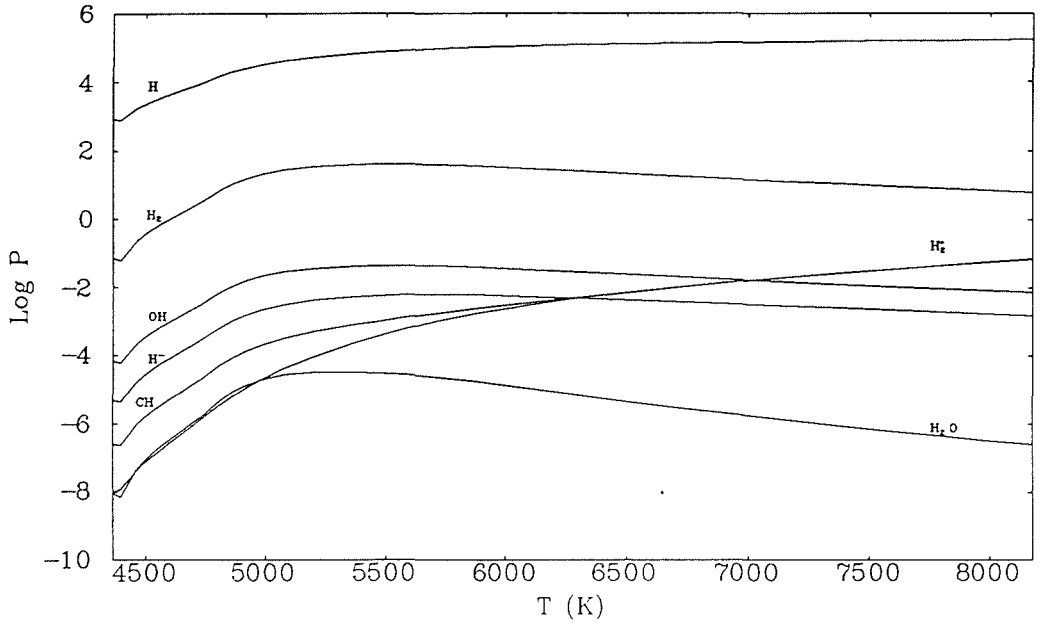

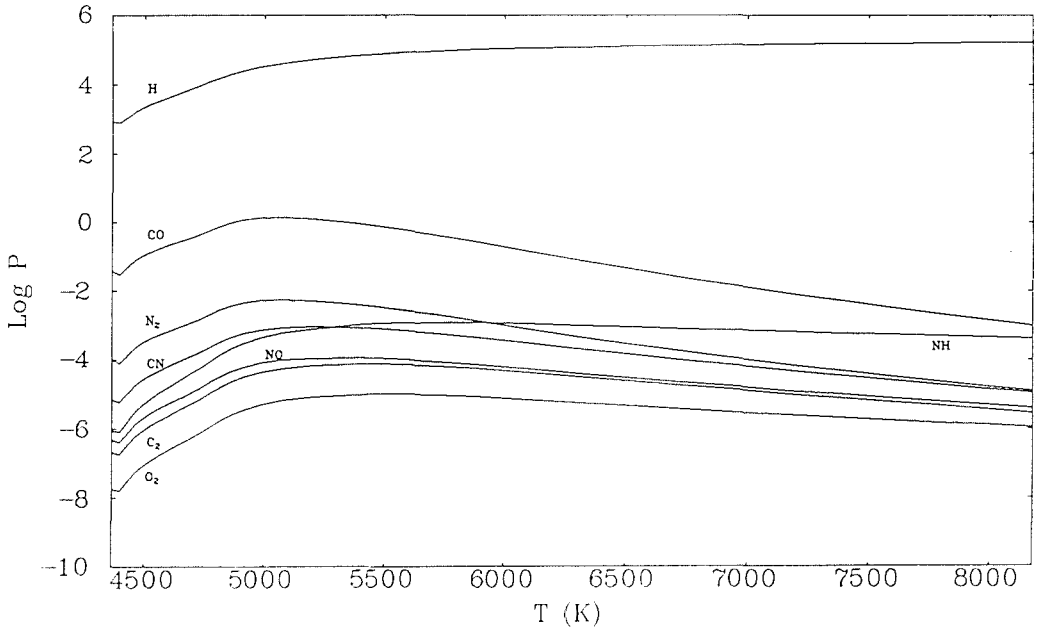

Figure 5.3: Molecular partial pressures as a function of temperature for KMARCS.

5.2.3 Opacity

Alterations in the opacity subroutines were necessitated by the change in normalisation and again it is important to ensure that the opacities calculated by the new routines in KMARCS are identical to those in MARCS. Figure 5.4 shows the total continuous opacity for a range of temperatures and electron pressures typically found in cool atmospheres, the full-line – MARCS and the dashed-line – KMARCS. For hydrogen rich compositions the additional opacity sources included in KMARCS make little or no significant contribution to the total continuous opacity. The main components of the continuous opacity are, at short wavelengths, bound-free and free-free transitions from metals, principally C I, and at longer wavelengths H^-. This is shown in Figure 5.5.

5.3 Hydrogen rich models for comparison.

Models have been computed using both programs for comparison. The results are shown in Figures 5.6 to 5.9. The first set represents a solar type atmosphere with an effective temperature of T_{eff}=5800K and a surface gravity of $2.5\text{x}10^2\,\text{cms}^{-2}(\log g = 4.40)$. The second set represents a giant model with effective temperature of T_{eff}=7000K and surface gravity of $79\,\text{cms}^{-2}(\log g = 1.90)$. In each case the solid line gives the results from MARCS and the dashed line from KMARCS.

The emergent flux has only been plotted for the KMARCS models, since the differences between the two models are insignificant. The strong *absorption* lines visible at the blue end of the spectrum are not physical but are due to the use of opacity distribution functions in the calculations. Obviously this implies that the energy distribution cannot be directly compared with observations, at least in the blue. However, the model atmosphere may be used in conjunction with a spectrum synthesis program to calculate realistic flux distributions.

The temperature structures are very similar, differing only at the boundaries. These differences may be ascribed to the lower convective flux in the KMARCS model. An important point to note is that where the differences are greatest, in the giant

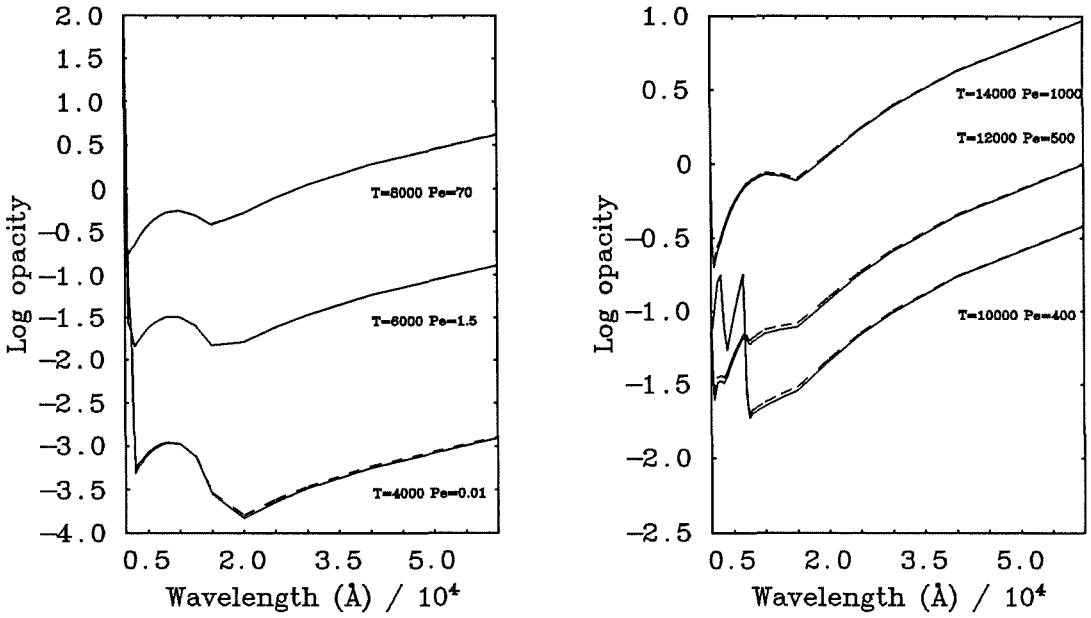

Figure 5.4: The continuous opacity at a selection of temperatures and electron pressures.

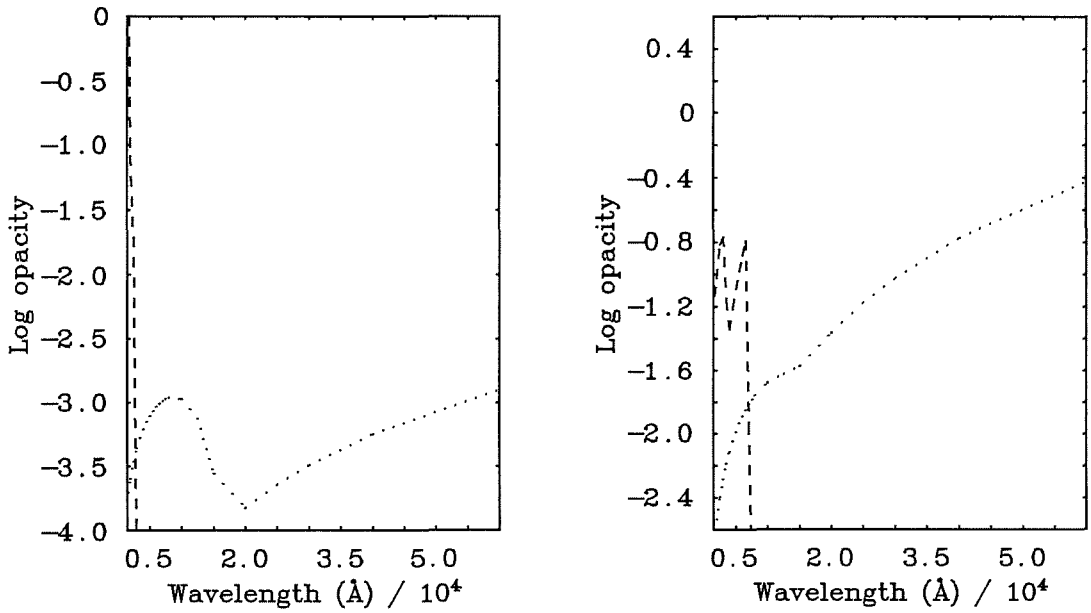

Figure 5.5: The main components of the continuous opacity at T_{eff}=4000K and 14000K, the dotted line is H^- and the dashed line the metals.

model, they lie at depths too great to affect line formation and consequently will not affect the interpretation of stellar spectra.

The gas and electron pressures differ little; the graphs barely showing any differences. The rapid increase in electron pressure at an optical depth of $\tau = 1.0$ is due to the onset of ionization of hydrogen. The consequences of this rapid increase are shown by the fall in density in the giant model (Figure 5.9) and the onset of convection as shown in Figure 5.10.

The difference in the convective flux calculated for the giant atmospheres is due to the errors in calculating the internal energy and the subsequent effect on the connected thermodynamic quantities. This also explains the hotter inner boundary temperature seen in the giant model (Figure 5.8).

5.4 Hydrogen-deficient Models

5.4.1 The effects of hydrogen-deficiency on the equation of state.

The composition remains the same as that given in Table 5.1 with only the ratio of hydrogen to helium changing; the metal abundances remain fixed. The same set of temperature and electron pressure points are used as in the earlier section to enable the effects of altering the hydrogen abundance to be highlighted. Figure 5.11 shows the effect on the gas pressure and density of altering the hydrogen abundance. The solid line is $N_H/N_{He} = 10$, dashed line $N_H/N_{He} = 10^{-2}$, dotted line $N_H/N_{He} = 10^{-4}$ and dash-dotted line $N_H/N_{He} = 10^{-6}$.

The gas pressure becomes greater for the hydrogen-deficient atmospheres beyond temperatures of 7000K due to the absence of the hydrogen ionization zone where increasing the electron pressure does not increase the gas pressure significantly. A similar effect is seen in the density figure. By the time the hydrogen abundance has fallen to $N_H/N_{He} = 10^{-4}$ hydrogen may be regarded as a trace element and no longer affects the thermodynamics.

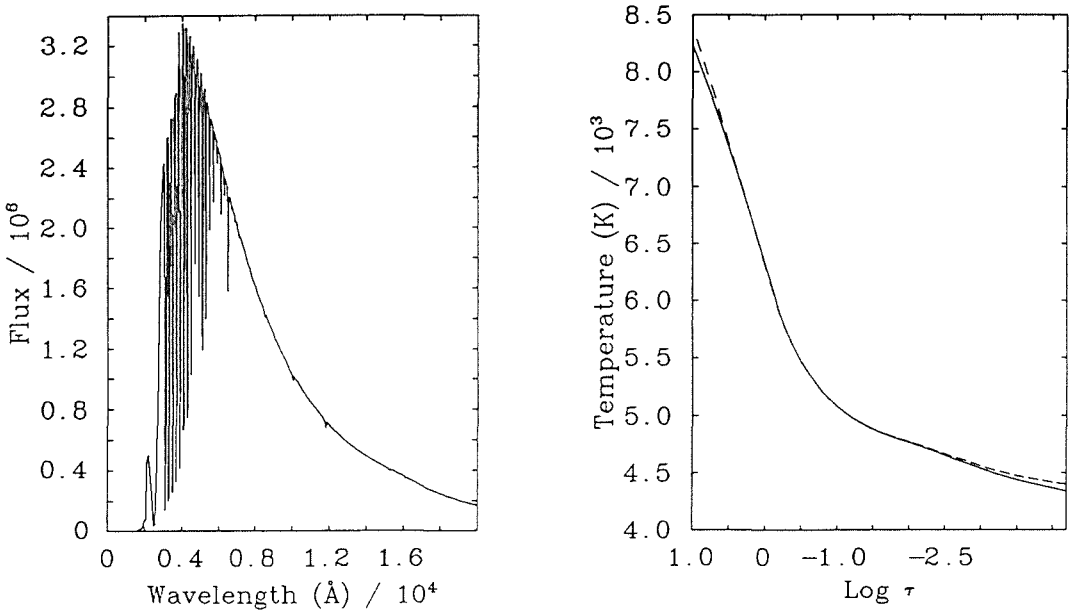

Figure 5.6: The emergent flux and temperature structure for the solar model.

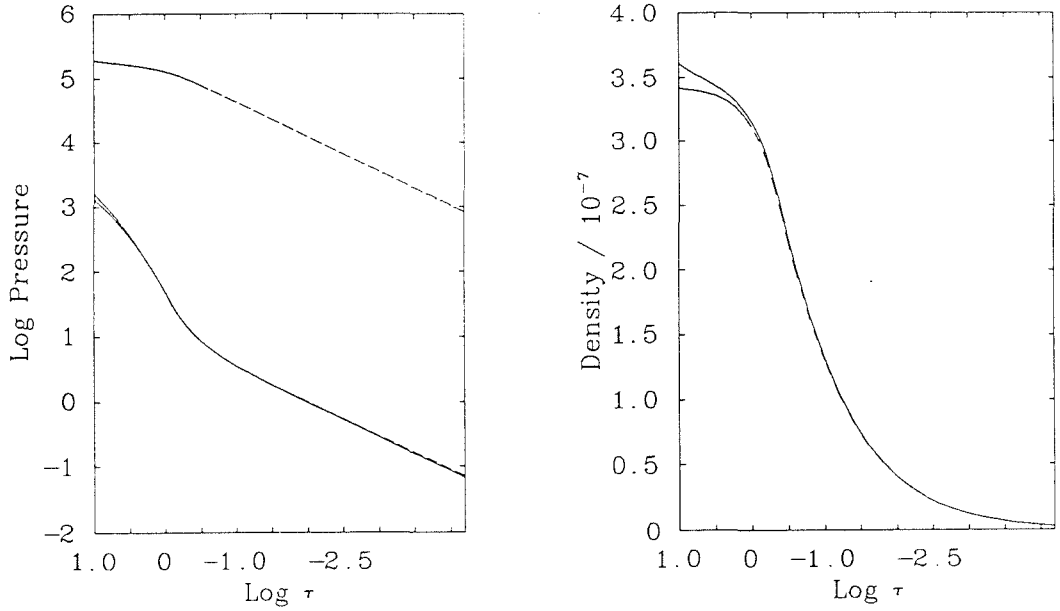

Figure 5.7: The gas and electron pressures together with the density profile for the solar model.

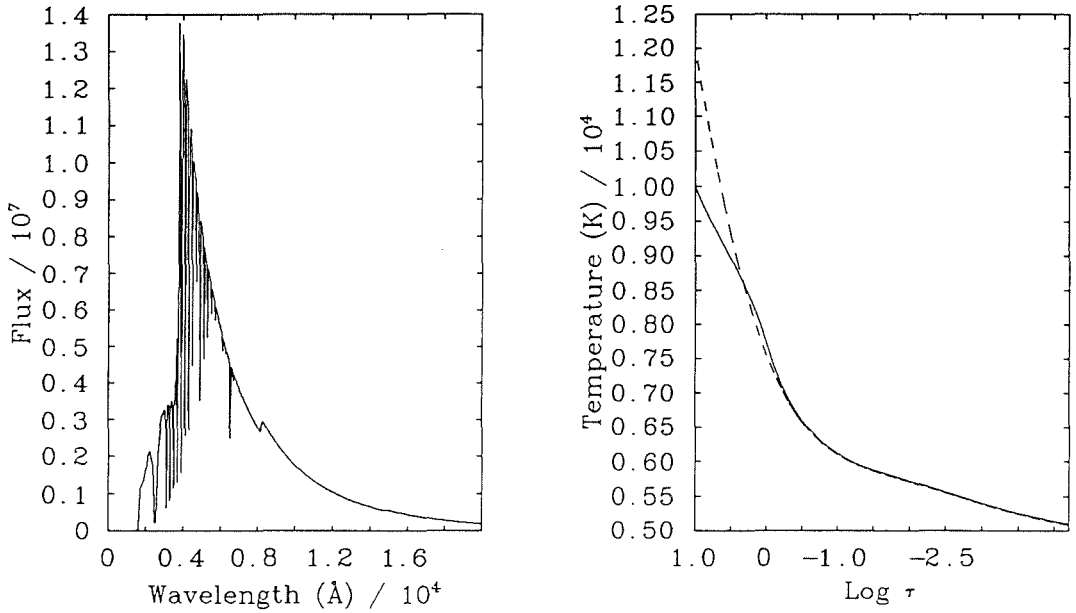

Figure 5.8: The emergent flux and temperature structure for the giant model.

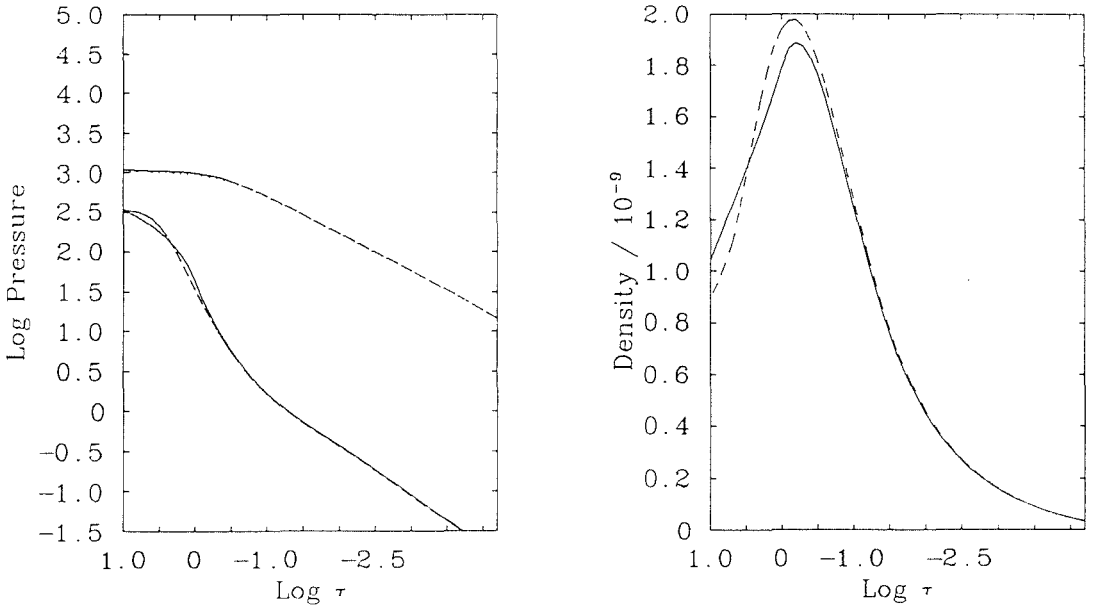

Figure 5.9: The gas and electron pressures together with the density profile for the giant model.

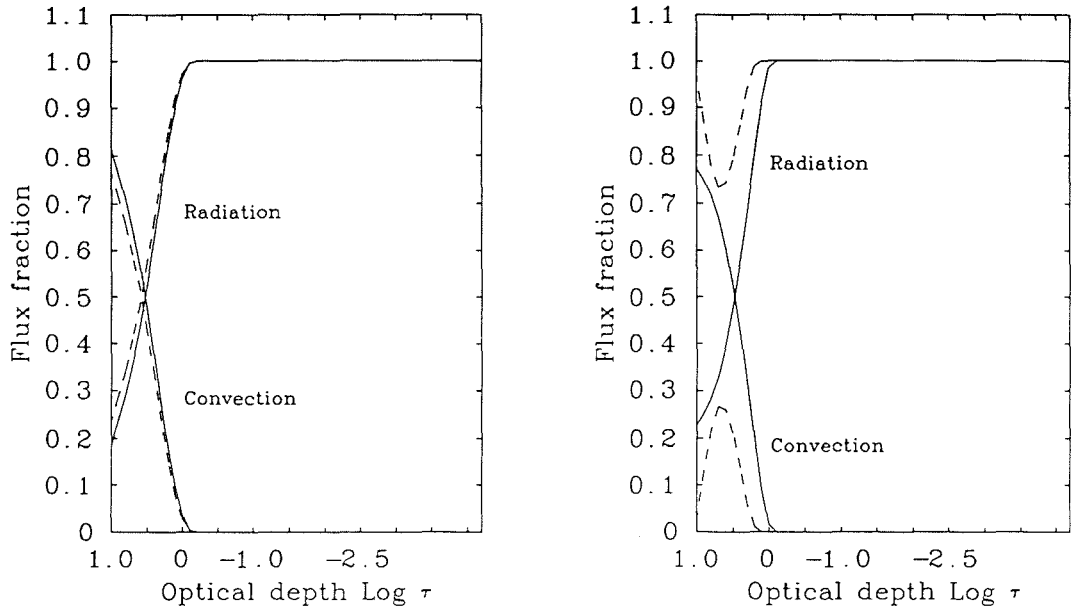

Figure 5.10: The relative contribution to the total flux from radiation and convection for the solar and giant models.

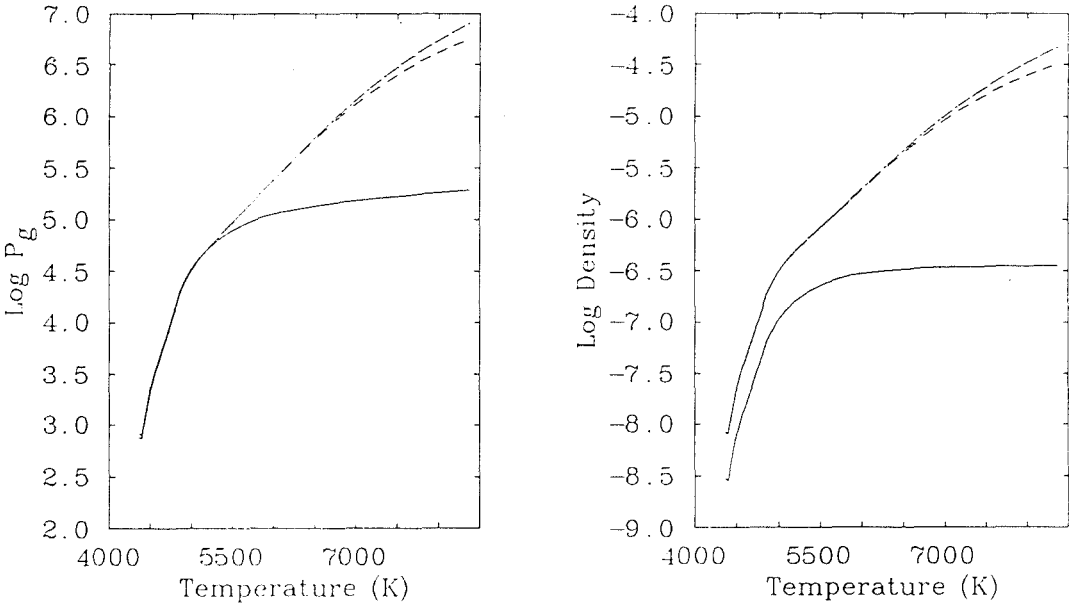

Figure 5.11: The effects of altering the hydrogen abundance on the gas pressure and the density.

Figures 5.12 and 5.13 illustrate the effect on the continuous opacity of reducing the hydrogen abundance whilst keeping the ratio of $N_H + N_{He}/N_Z$ constant. The same line styles as in the previous figure are used for the differing hydrogen abundances.

At low temperatures the major opacity sources are C I and H^-; at higher temperatures He I becomes important. As the hydrogen abundance is reduced, the relative contribution of H^- to the continuous opacity falls. The continuous opacity reaches a minimum when $\log N_H = 8$ when the contributions from C I, He^- and C^- become significant. It is important to note that in the visual region (*i.e.* , λ=3000-10000Å) the dominant opacity source is C I. This point will be returned to in Chapter 7.

5.4.2 Supergiant Models.

Previous studies of cool hydrogen-deficient stars have found them to be supergiants with surface gravities between $1 - 10 cms^{-2}$ ($\log g = 0 - 1.0$) and temperatures 3000-7500K. Therefore, models have only been calculated within this range. Cottrell and Lambert (1982) give the effective temperature and gravity of R CrB as T_{eff}=7000K and $\log g = 0.5$ and this was used to create a *typical* hydrogen-deficient atmosphere and a temperature of T_{eff}=5000K was adopted for the cooler objects.

5.4.2.1 Hydrogen Abundance

The models were calculated with solar metallicities and a reducing N_H/N_{He}. The calculated flux in shown in Figures 5.14 and 5.15, in the first case the H/He ratio has been reduced by a factor of 1000 and then subsequently by one of 100.

There is considerable difference between the *normal* composition and the hydrogen-deficient models. The Balmer jump is greatly reduced in the hydrogen-deficient model, which is only to be expected. The increase in flux at 7000Å corresponds to the opacity minimum as illustrated in Figures 5.12 & 5.13, the local maximum in the hydrogen-rich model is due to H^-. Bluewards of 7000Å the major opacity source is bound–free and free-free transitions from C I.

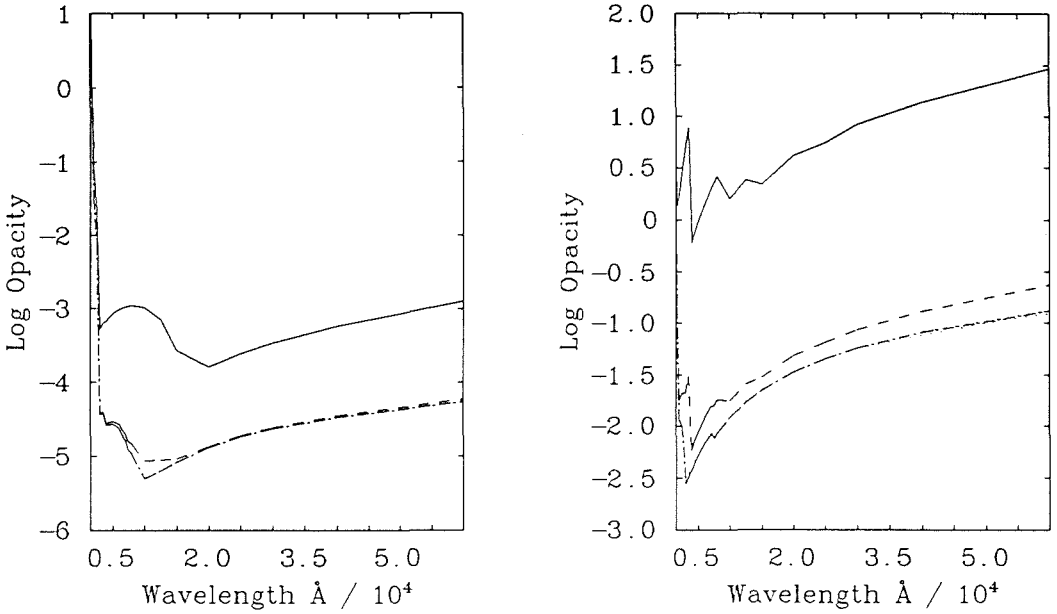

Figure 5.12: The variation in continuous opacity with differing hydrogen abundances at temperatures of 4000K and 8000K.

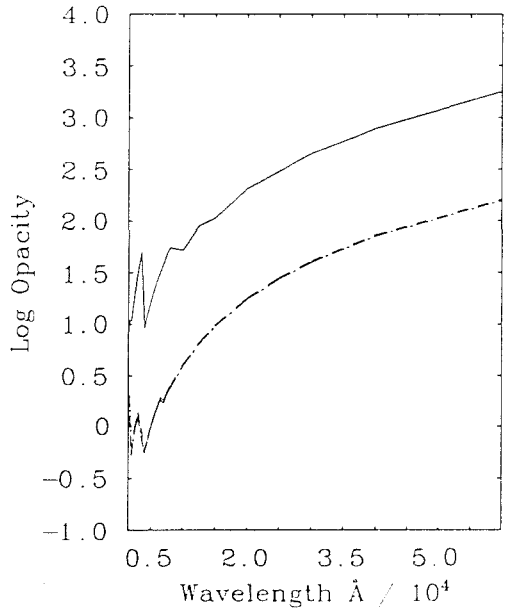

Figure 5.13: The variation in continuous opacity with differing hydrogen abundances at a temperature of 14000K.

The effect of reducing the hydrogen abundance on the temperature structure is shown in Figures 5.16 & 5.17. The left hand figure shows the temperature structure of the hydrogen-rich model (($N_H/N_{He} = 10$) and the right hand side the the differences between it and the hydrogen-deficient models (($N_H/N_{He} = 10^{-2}$and10^{-4}.

5.4.2.2 Carbon abundances

It was shown in the previous section that in hydrogen-deficient atmospheres the main continuous opacity source in the visual region is that of C I. Although C is a minor species it will greatly effect the calculated temperature structure of the model. This is illustrated in Figures 5.18 and 5.19.

It is important to note that the size of the temperature differences for differing N_H or N_C are the same. The consequence for the fine analyses of R CrB and HdC stars is that unless the atmosphere is extremely hydrogen-deficient both N_H and N_C will need to be determined along with N_{He}, T_{eff} and $\log g$.

5.4.2.3 Models of different T_{eff}

A series of models with a fixed composition of $N_H/N_{He} = 3x10^{-5}$ and $N_C/N_{He} = 3x10^{-4}$ was calculated for the same gravity ($\log g = 0.5$) and a range of temperatures. The calculated flux for each model is shown in Figures 5.20 and 5.21.

5.4.2.4 Convection

The mixing-length theory approximation used to describe convection in these models requires one to specify the mixing-length constant. Generally, a value of 1.5 times the pressure scale height is used, since this provides the best fit of solar models to observations. It is this value which was adopted for the initial calculations. All models calculated have the composition $N_H = 7.5$, $N_{He} = 12$ and $N_C = 10$.

In cool models with T_{eff}=5000K convection is seen in the deepest layers and is

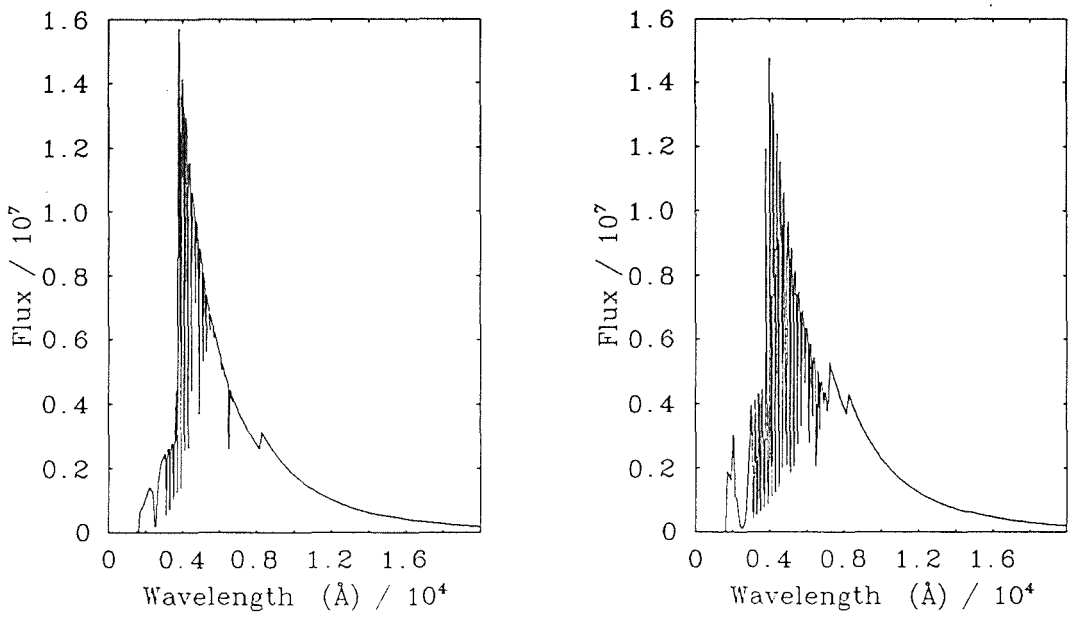

Figure 5.14: The flux for T_{eff}=7000K and $\log g = 0.5$ with N_H/N_{He} ratios of 10 and 10^{-2} respectively.

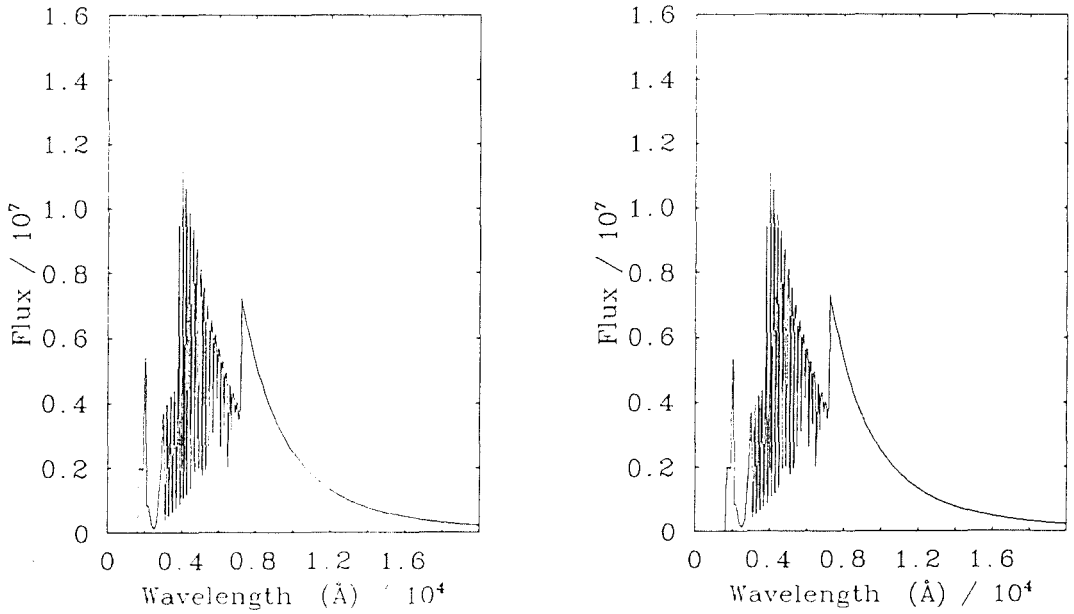

Figure 5.15: The flux for T_{eff}=7000K and $\log g = 0.5$ with N_H/N_{He} ratios of 10^{-4} and 10^{-6} respectively.

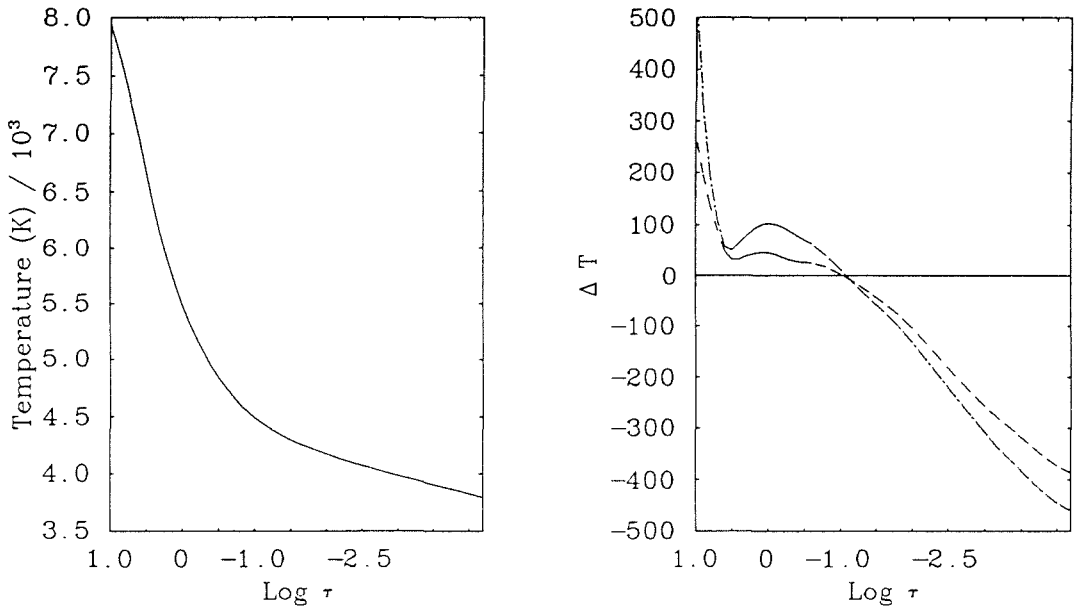

Figure 5.16: The effect on the temperature structure of reducing the ratio N_H/N_{He} with T_{eff}=7000K $\log g = 0.5$.

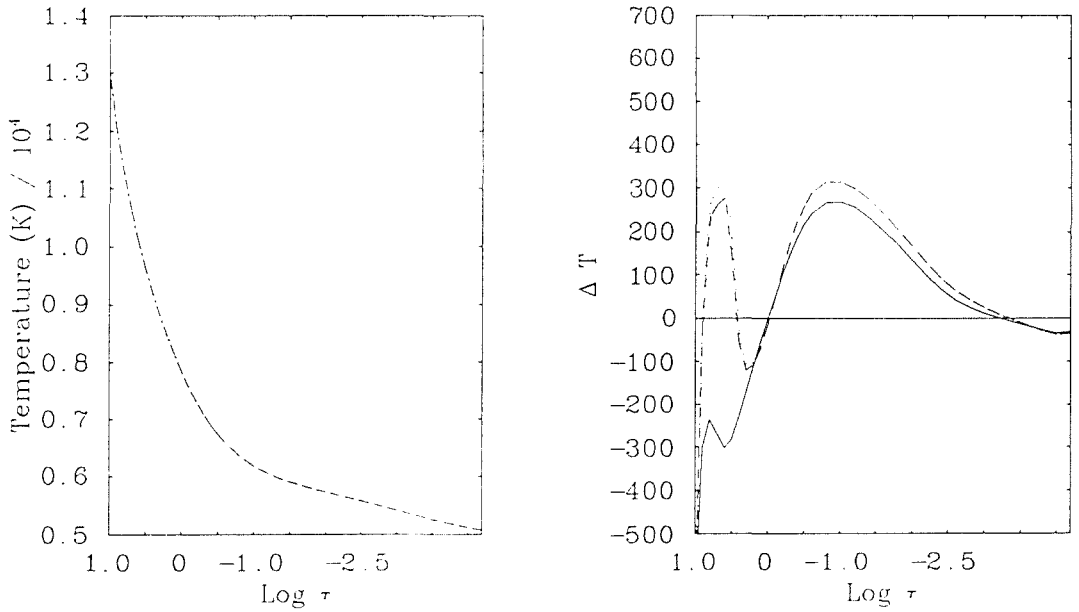

Figure 5.17: The effects of reducing N_H/N_{He} with T_{eff}=5000K and $\log g = 0.5$.

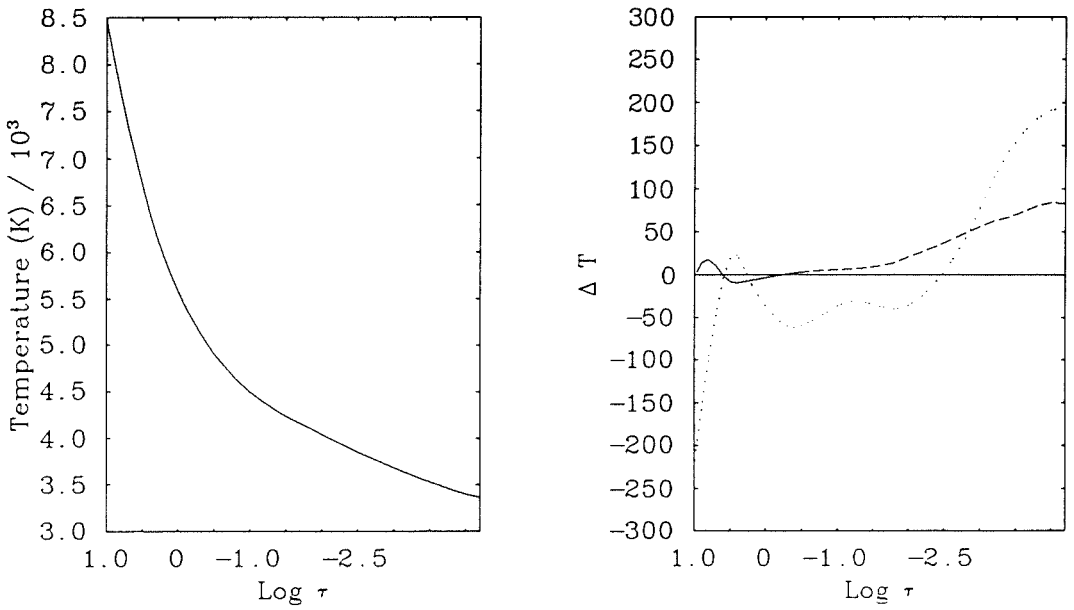

Figure 5.18: The temperature structure and differences for models with $N_C = 8.5, 7.0 \text{and} 10.0$ - full,dashed and dotted line, T_{eff}=5000K and $\log g = 0.5$.

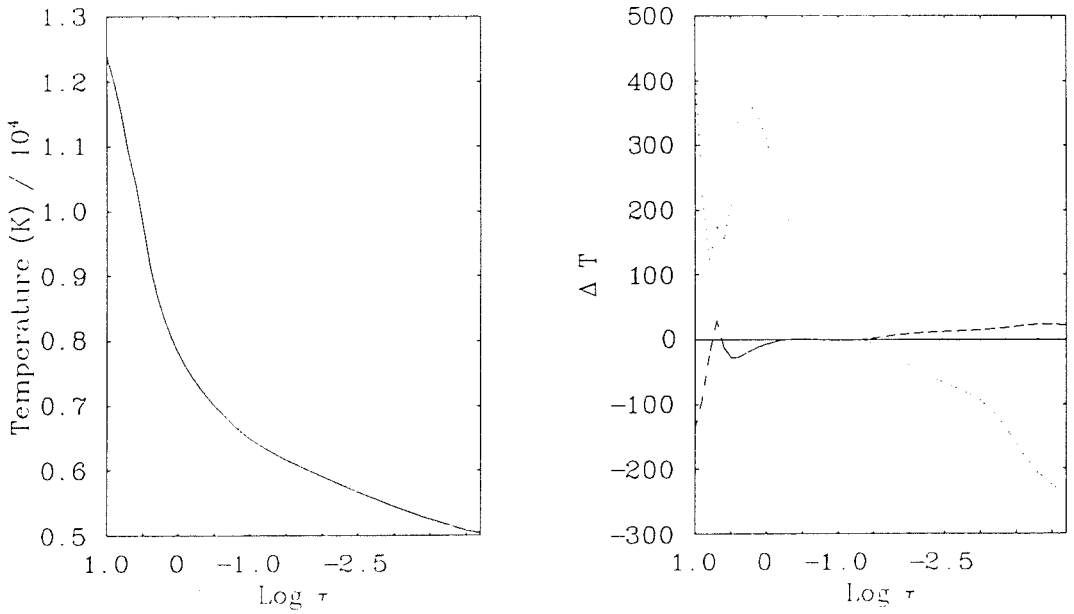

Figure 5.19: The temperature structure and differences for models with $N_C = 8.5, 7.0 \text{and} 10.0$ - full,dashed and dotted line, T_{eff}=7000K and $\log g = 0.5$.

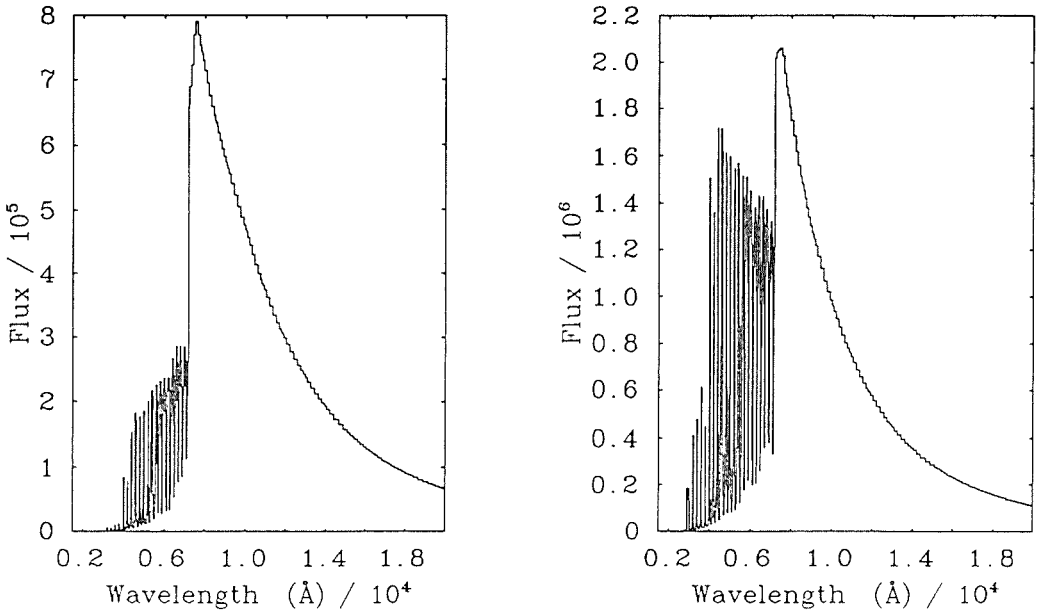

Figure 5.20: The flux for models with T_{eff}=4000K and 5000K.

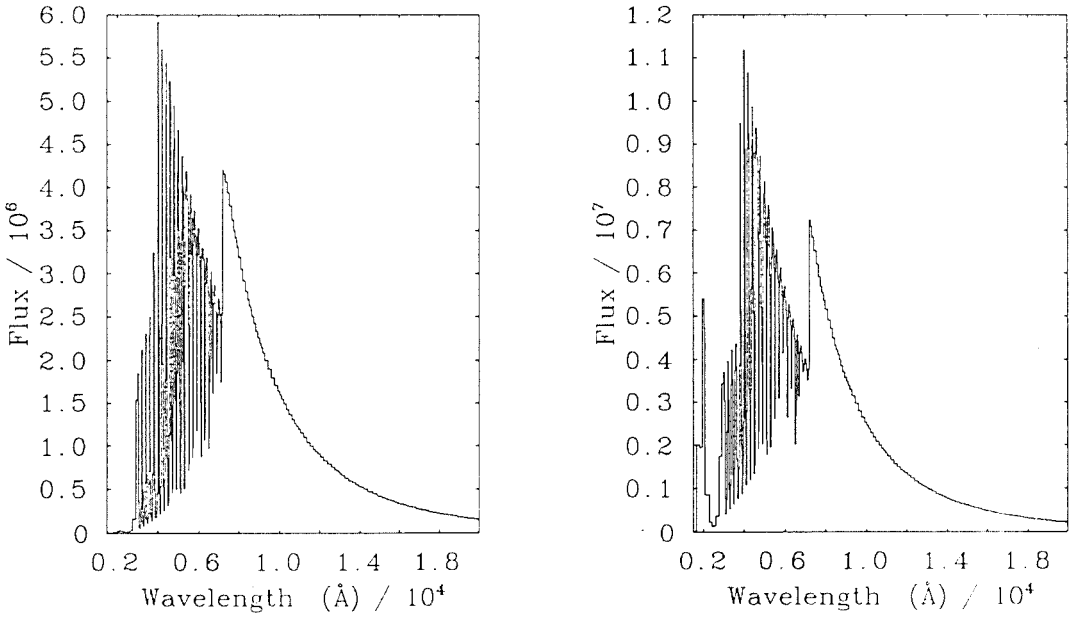

Figure 5.21: The flux for models with T_{eff}=6000K and 7000K.

associated with the ionization of carbon I. The convective flux rises to a maximum of 30% of the total flux. Obviously the relative proportion of convective flux increases with increasing carbon abundance.

In the higher temperature models (T_{eff} = 7000K) the carbon I ionization zone lies too close to the surface for convection to occur. The low hydrogen abundance suppresses the H I/H II convective zone. Convection only becomes important in these models when both the hydrogen and carbon abundances are small, when it is due to He I ionization at the bottom of the atmosphere. Thus, convection is unlikely to be important, since previous observed carbon abundances are far greater than the required low abundance to initiate convection.

In order to investigate the effects of convection on the models the mixing-length parameter was set to zero and three. Only in the case of the low temperature model, T_{eff} = 5000K, did the mixing length have any effect on the resulting temperature structure of the atmosphere. The effect of convection was to decrease the inner boundary temperature, giving a shallower temperature gradient. Increasing the value of the mixing length parameter to three increased the convective flux to 50% of the total flux. This corresponds to a temperature decrease of $\sim$ 700K.

5.4.2.5 Line blanketing

The effects of numerous overlapping absorption lines in the visual region in cool atmospheres is modelled as an additional quasi-continuous opacity source. The technique used in MARCS is that of opacity distribution functions (ODF), a description is given in Chapter 4. The ODFs calculated by Gustafsson *et al.* (1975) used hydrogen rich compositions and therefore their use in representing the line-blanketing in hydrogen-deficient models is questionable.

The opacity calculations shown in Figure 5.12 and 5.13 show that for low hydrogen abundances the decrease in continuous opacity is of the order of 10^3. The metal abundances will be constant and therefore the line opacity remains unchanged. The consequence is that the line-blanketing will be enhanced by a factor of 10^3 with re-

spect to the hydrogen-rich composition. Thus the use of the hydrogen-rich ODFs will represent a lower limit to the line-blanketing present.

The effects of line-blanketing are shown in Figures 5.22–5.23. The blanketed models show a decrease in the surface temperature together with increase in the temperature gradient in the outer layers.

5.4.2.6 STERNE

As has been stated earlier, previous models of hydrogen-deficient stars have used Schönberner's program STERNE. The program STERNE was written independently of MARCS. The version of STERNE used does not include ODFs for line-blanketing. Figure 5.24 shows the temperature structure for STERNE, unblanketed and blanketed KMARCS models. The continuous line is that of STERNE, the dotted line of unblanketed KMARCS and the dashed line of blanketed KMARCS.

The unblanketed KMARCS models are similar in form to those of STERNE. The differences between them are due to the fact that the optical depth scales are defined differently. KMARCS uses an optical depth scale based on the Rosseland mean opacity whereas STERNE uses the opacity at $\lambda = 5000$Å.

As can be seen from these figures KMARCS has a more limited depth scale. In Figure 5.25 the depth scale in KMARCS was extended from the usual $\log\tau = -4.2$ to $\log\tau = -5.8$. There are no significant changes. However, the extended depth scale may be necessary for the calculation of equivalent widths if the lines are formed in the outermost regions.

5.5 Conclusion

It has been shown in the first section that the changes made to MARCS to enable hydrogen-deficient models to be calculated have not affected the calculation of hydrogen-rich models. The slight differences between the two programs have been iden-

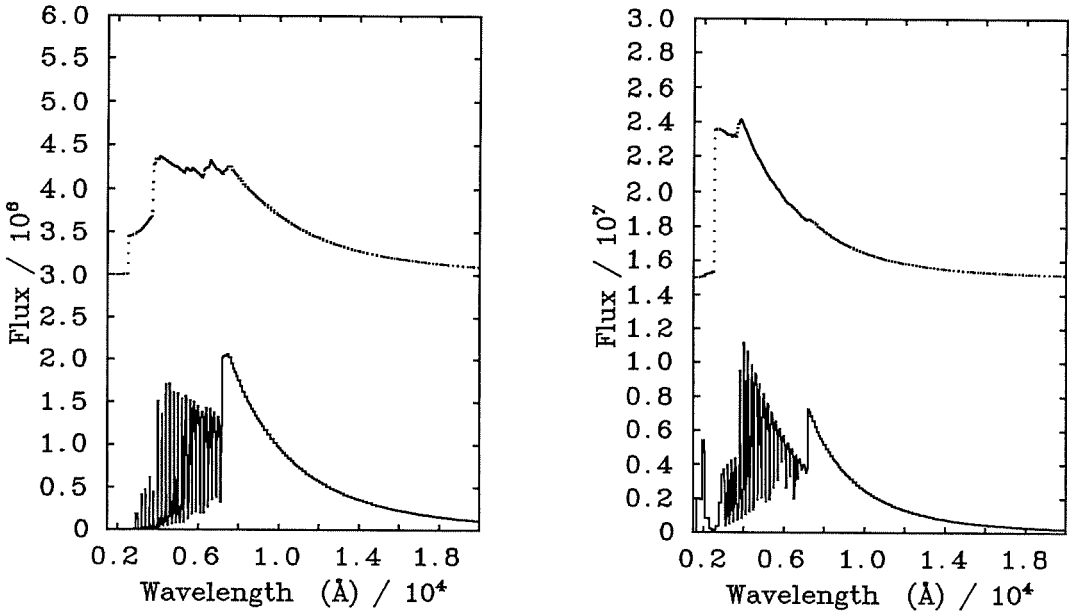

Figure 5.22: The flux for blanketed and unblanketed models with T_{eff}=5000K and 7000K (blanketed full-line, unblanketed dotted-line).

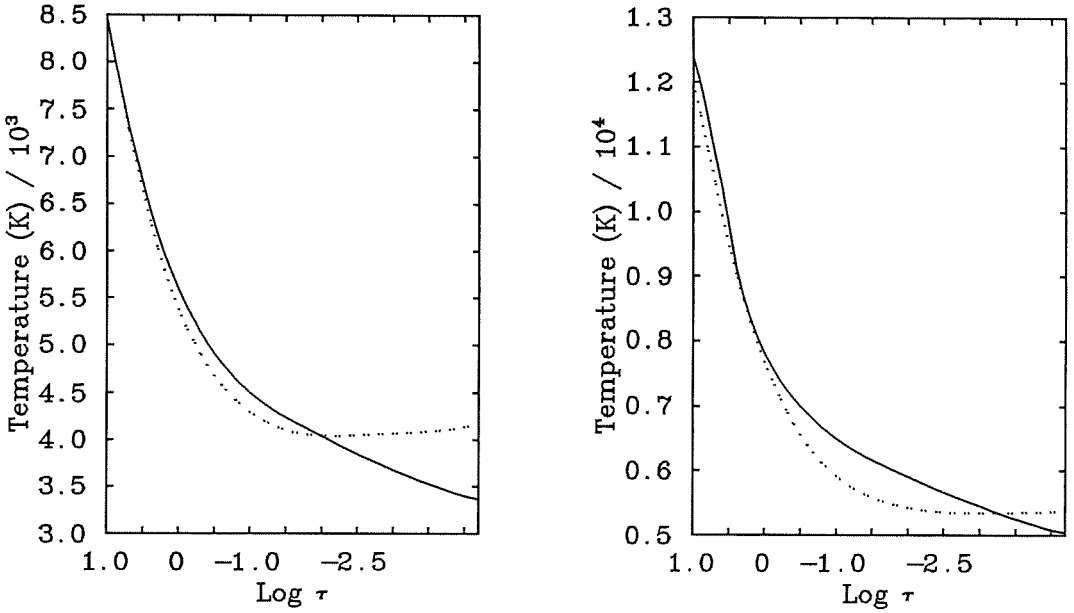

Figure 5.23: The effect on the temperature structures (blanketed full-line, unblanketed dotted-line).

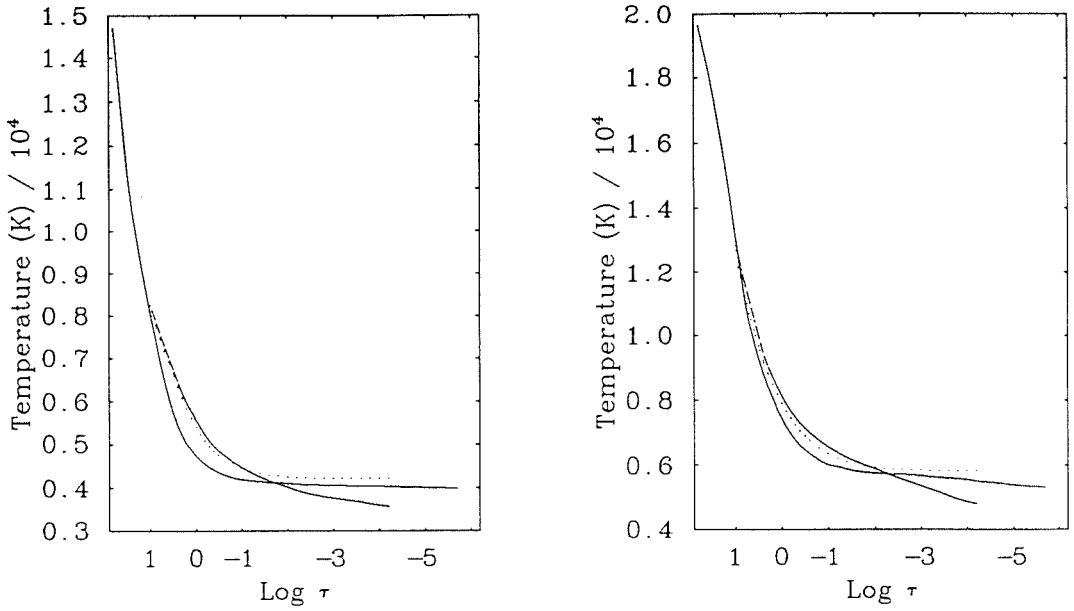

Figure 5.24: The temperature structures for models with T_{eff} = 5000K and 7000K, $\log g = 0.5$.

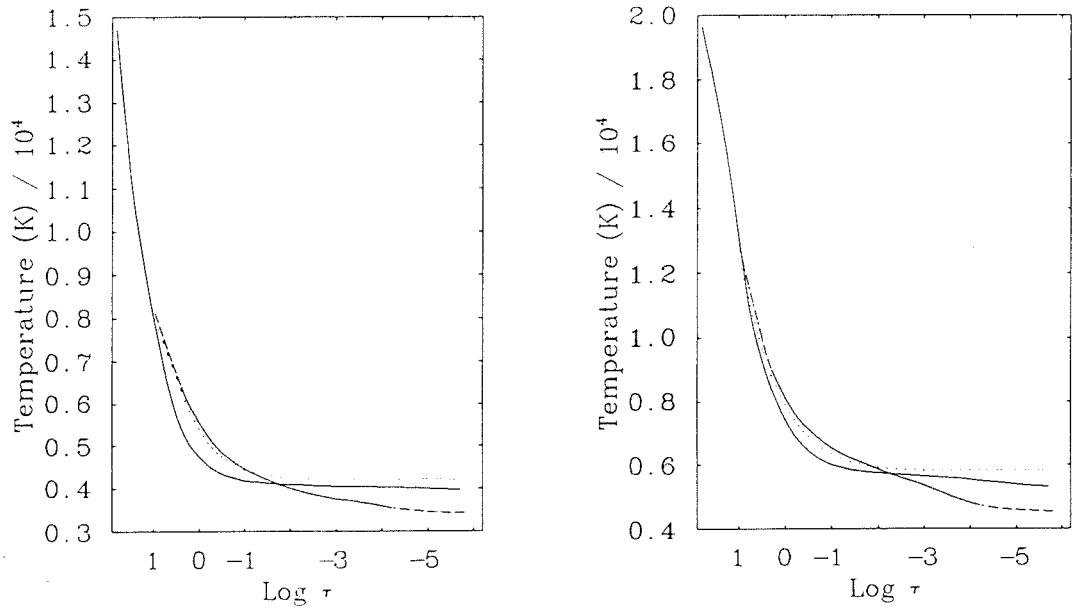

Figure 5.25: The temperature structures for models with T_{eff} = 5000K and 7000K, $\log g = 0.5$ with extended depth scales.

tified as being due to the error in the calculation in convective flux and the addition of new opacity sources necessary for hydrogen-deficient models.

The hydrogen-deficient models presented have shown that the relative abundance of N_H and N_C are equally important and that this will complicate the fine analyses of R CrB and HdC stars. Although the ODFs used for line-blanketing were calculated for hydrogen-rich models they provide a lower limit to the expected blanketing and its subsequent effects. The use of hydrogen-deficient ODFs is expected further to decrease the surface temperature and increase the gradient. Convection was found to be unimportant except in the coolest models where the ionization of C I is the site of the convective zone. This occurs in the deepest layers where the atmosphere is optically thick and will probably only affect line formation slightly.

It is impossible to quantify any possible systematic errors inherent in these models. Unlike the programs for hydrogen-rich stars which may be used to calculate solar models for comparison with high accuracy solar observations, there is no such comparison available for hydrogen-deficient programs. Thus it is very difficult to quantify any model inadequacies. Apart from possible errors due to deviations from the classical model assumptions, the most likely source of errors will be in the physical data used in the equation of state. As was shown in the previous sections the reduction in hydrogen abundance results in minor species contributing significantly to the opacity. Thus it is important that all minor opacity sources are included and that the data used are accurate.

5.6 References

Gustafsson B., Bell R., Erikson K., Nordlund A., (1975) *Astr. Astrophys.*, **42**, 402

Cottrell P., Lambert D.L., (1982) *Astrophys. J.*, **261**, 595

Schönberner D., (1975) *Astr. Astrophys.*, **44**, 483

Chapter 6

High Resolution Spectra of RY Sgr.

6.1 Introduction

The fine analysis of stellar spectra requires good wavelength coverage at high resolution and signal-to-noise in order to derive accurate temperatures, gravities and abundances. The choice of instrument and detector are dictated by these requirements. The echelle spectrograph is an optimal choice of spectrograph, having a multiplex advantage over conventional grating spectrographs. However, it is only the recent advent of large format electronic detectors that has seen the realisation of this advantage.

The results of observations obtained with the University College of London echelle spectrograph (UCLES) at the Anglo-Australian telescope (AAT) are presented. The reduction of echelle spectra is more difficult and complicated than that of conventional spectrographs so the reduction procedure is outlined in greater detail than usual.

For completeness the stars U Aqr and HD 182040 are included in the description of the reduction process. However, only for the spectrum of RY Sgr have lines been identified and measured.

6.2 Observations

The Director of the Anglo-Australian Observatory allocated about half of the night 14-15 September 1989 for service observations to be made of RY Sgr, U Aqr and HD 182040. The observations were made by the duty astronomer Dr. W. Lupton and are detailed in Table 6.1.

Table 6.1: The journal of observations made with the AAT UCLES and Thomson CCD.

Star	H.J.D. - 2440000	Exposure (s)	Grating Angle
RY Sgr	7784.03	240	56.17
HD 182040	7784.03	240	
U Aqr	7784.04	1200	
U Aqr	7784.06	1200	
HD 2796	7784.08	500	
HD 2796	7784.08	500	56.40
U Aqr	7784.10	1200	
U Aqr	7784.14	1200	
RY Sgr	7784.13	240	

The 31g/mm grating was chosen to give the highest possible resolving power ($\lambda/\delta\lambda$) of $\sim 80,000$. The detector used was the Thomson 1024x1024 CCD. The choice of detector was determined by the need for good quantum efficiency in the red and a large physical size to minimise the number of exposures required to cover the spectral range. The Thomson CCD fulfills both criteria, having a quantum efficiency of $\sim 40\%$ from 5000-8000Å (Barton & Sadler 1990) and an area of 19x19mm. The only other possible detector would have been the IPCS which, although it has a larger format, has poor response in the red and suffers from count rate limitations associated with photon counting detectors when observing bright objects.

The spectral range 4890–6950Å observed required a pair of observations in order to cover fully the free spectral range (FSR). The FSR increases with wavelength, being 20.8mm (42.3Å) in order 116 and 29.1mm (82.5Å) in order 83, the CCD being only 19mm wide.

In addition to the program stars the B star HD 2796 was observed in order to enable the identification of telluric absorption lines present in the program star spectra.

Finally, a thorium – argon arc and quartz lamp continuum source were observed at each grating setting as needed for the reduction process set out below.

6.3 Reduction of Echelle Spectra.

The reduction process is implemented as a set of Figaro tasks (Shortridge 1986) based upon the Caltech echelle reduction software written by J. MacCarthy and adapted for UCLES by W. Lupton.

1. The frames must be orientated such that the wavelength scale increases from left to right and from bottom to top. This required the frames to be rotated clockwise 90° and then reflected about the x axis.

2. The three bias frames obtained during the night were averaged and subtracted from the other frames.

   At this point the pairs of observations of U Aqr were co-added, the stability of UCLES dispensing with the need to reduce them individually.

3. The position of each order is found by cross-correlating the central few columns and then triangular filtering to enhance the peaks. The positions of the peaks then give a good approximation to the order centres. The orders are then individually traced across the frame by fitting a Gaussian profile in the spatial direction at intervals along the order. Then a low order polynomial (3^{rd} order being sufficient) is fitted to the midpoints of the Gaussian, thus giving the position of the order in pixel coordinates.

4. From the quartz lamp frame the position of the jaws of the dekker is found and the spatial profile of the object then determined from the central few columns. At this stage the sky pixels may be identified to enable sky subtraction. However, the design of UCLES created narrow orders tightly packed in order to maximise the wavelength coverage in a single frame. The consequence is that except in very

good seeing the star profile fills the order with no sky present. For bright objects the absence of sky is not that important, since its contribution is small except in regions with night sky lines. The night sky lines are easily identified from the spectrum of the B type star HD 2796.

5. The quartz lamp frame is used to obtain the pixel to pixel variations and thus correct the object frames. The method used is to fit a low order polynomial along each row within an order. The flat field corrections are then calculated by dividing the row by the fitted polynomial, the corrections being of order unity.

6. The simplest method of extracting the spectrum from each order is just to sum the contributions from each row making up the order. However, this approach fails to take into account the effect of the spatial profile of the star within the order, *i.e.* , the signal to noise being least at the edges of the profile. An optimal scheme of summing the contribution from each row within each order is used. The spatial profile of the star is fitted with either a polynomial or a Gaussian and this is then used to obtain the optimal weights for summation. This approach follows that of Horne (1986). Generally it is at this stage that any contribution from the sky will be subtracted from the echellogram, but no sky was observed.

7. A thorium-argon arc was observed for the purposes of wavelength calibration and the lines were identified using the ESO arc atlas (D'Odorico *et al.* 1987). The arc fitting is semi-automatic. Initially a few orders need to be fitted manually, then a program uses this to fit the rest automatically. The typical fit for given order generally has an O-C of less than 5.0×10^{-3}Å/pixel (rms). In the case of orders where the fit was worse than this, they were refitted manually.

8. In addition to the pixel to pixel variations in sensitivity there is a large scale variation in sensitivity caused by the echelle grating, the blaze profile or function. This profile is at a maximum at order centre falling away at the edges of the order. The profile may be corrected by fitting a suitable polynomial and then dividing the object spectum by it. In order to get the best possible fit to the profile a source of continuum radiation is required. This may be obtained from either the quartz lamp or from the B star frames. The quartz lamp was used because of the greater signal to noise in those frames when compared with the B star frames.

9. The final step is to convert the two dimensional echellogram into a one dimension spectrum. As the detector does not cover the complete free spectral range at these wavelengths this results in gaps in the wavelength coverage of a single exposure. Thus a second spectrum of each object was obtained at a slightly different central wavelength to ensure complete wavelength coverage. Although it is possible to merge the two spectra into a single continuous spectrum it was decided to treat them individually due to the difficulties in obtaining a good match for each overlapping order simultaneously.

10. A inherent feature of echelle spectra is that each pixel corresponds to a fixed velocity interval, so the wavelength scale is nonlinear. Therefore the spectrum is resampled and mapped onto a linear wavelength scale with a resolution of 0.1Å/pixel.

6.3.1 Cosmic Rays

One of the problems of using CCDs as detectors is that they are also sensitive to cosmic ray events. This is especially a problem with long integrations and was the main reason why the observations of U Aqr were split into two shorter integrations.

The cosmic ray events may be single pixel events or extend across several adjacent pixels depending on the angle at which the cosmic ray hits the CCD. If the event is just a single pixel then it is possible to *fix* it by interpolation between the surrounding pixels. Obviously when the event extends over several pixels this is inaccurate.

Although Figaro contains routines to enable the events to be *fixed* it was decided that the best approach was to treat any events as lost pixels and ignore them. The number of events was relatively small due to the short integration times (maximum 1200s). The region of overlap between the two observations allowed some cosmic rays to be fixed by using the data in the other frame. Otherwise, lines affected were ignored and not used to obtain equivalent widths.

6.4 Measurement of Equivalent Widths

The equivalent width (EW) of a spectral line is defined as

$$W_\lambda = \int_{\lambda_c-\Delta\lambda}^{\lambda_c+\Delta\lambda} (1 - F_{line}/F_{cont})\, d\lambda \tag{6.1}$$

where F_{line} and F_{cont} are the fluxes in the line and continuum respectively.

In order to measure the EW the position of the continuum must be found. This is a major problem for cool stars where the large number of lines, often blended, precludes accurate placement of the continuum level. The approach taken was to fit a cubic spline through the maximum points in each order and use that as estimate of the continuum level. An example showing the positioning of the continuum level is shown in Figure 6.1.

The measurement of the EW is done by least squares fitting a Gaussian profile to the line, the EW then being given by the integral over the Gaussian. The fit for most lines is good, any errors being far less than the error due to continuum level placement. Blended lines are modelled by fitting several Gaussians simultaneously (see Figure 6.2).

All EW's have been measured using the emission line fitting (ELF) procedures within the Starlink package DIPSO (Howarth and Murray 1988)

6.5 Atomic Data

The oscillator strengths, gf values, are taken from many sources. The principal source is the list presented in Cottrell and Lambert and (CL82,1982) with the remainder from Weise *et al.* (1966).

As can be seen in Tables 6.2–6.7, for certain species and ions there is a paucity of atomic data. This is especially true for C I, Ti II, Fe II and Ni II. As accurate laboratory values are unavailable for these species, the only alternative is to use solar oscillator strengths. Then one uses the known abundance of a species and observed EW together with a solar model to calculate the oscillator strength. This is far less accurate than laboratory values due the inadequacies of the models and physics used.

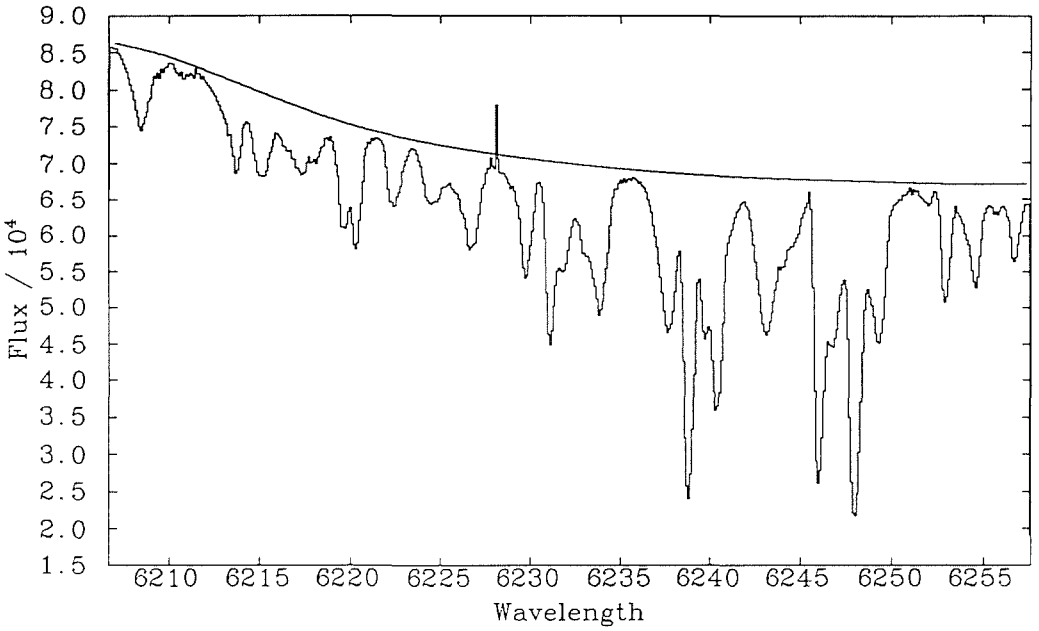

Figure 6.1: An example showing the position of the continuum in RY Sgr.

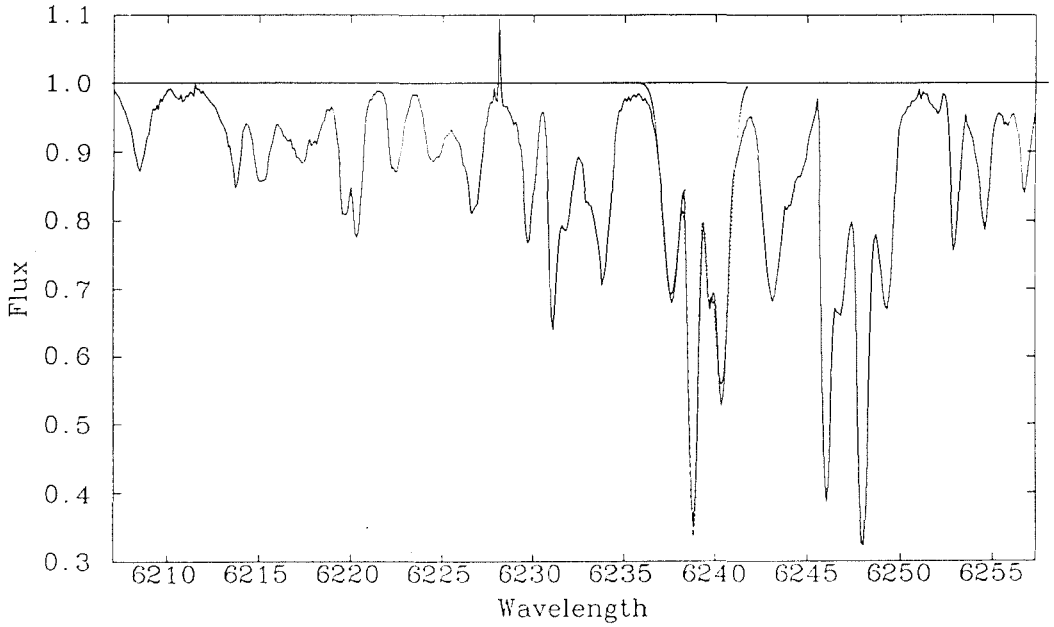

Figure 6.2: The fitted absorption lines.

6.6 RY Sgr

6.6.1 Line Identifications

The spectrum of RY Sgr is presented in Figures 6.7–6.27. The absorption lines were identified with the aid of the published line lists of R CrB (Keenan and Greenstein (1963) and CL82), together with previously identified lines in RY Sgr by Danziger (1965), D65, and Moore's Multiplet Tables (1959). Line identifications together with the measured equivalent widths are given in Tables 6.2–6.7. In cases where the blending is very severe the line is merely identified and no EW given.

A comparison between the EWs measured by D65 and CL82 is shown in Figures 6.3 and 6.4. In the upper two diagrams the continuous line is the predicted line along which the measured EWs should lie. The dotted line shows the best fit to a line through the origin. The gradient of this line is less than unity which implies that the EWs presented here are greater than those of CL82 or D65. The most probable reason for this is that the placement of the continuum level is slightly higher than used by them.

There still exists considerable scatter between the different sets of measured EWs. It is expected that the measurements by D65 have greater errors due to the use of photographic emulsion as the detector. In addition D65 calculated the EWs by using the product of the half intensity width and the depth rather than calculating the area under the line. The EW of Hα as measured by CL82 is 50% different from the results obtained here and in D65. This discrepancy is most likely due to the shock wave present in the atmosphere of RY Sgr during the observations of CL82 and may account for some of the scatter in the different sets of EWs.

It is interesting to note that there are no molecular bands due to C_2 or CN visible in the spectrum in these regions.

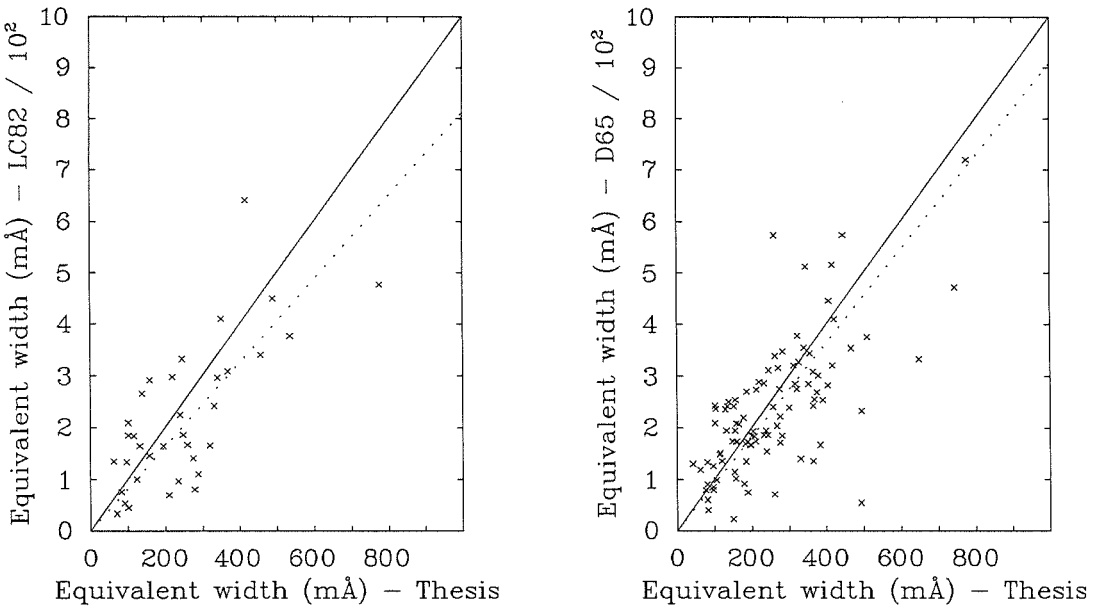

Figure 6.3: A comparison of the measured EWs by CL82 and D65.

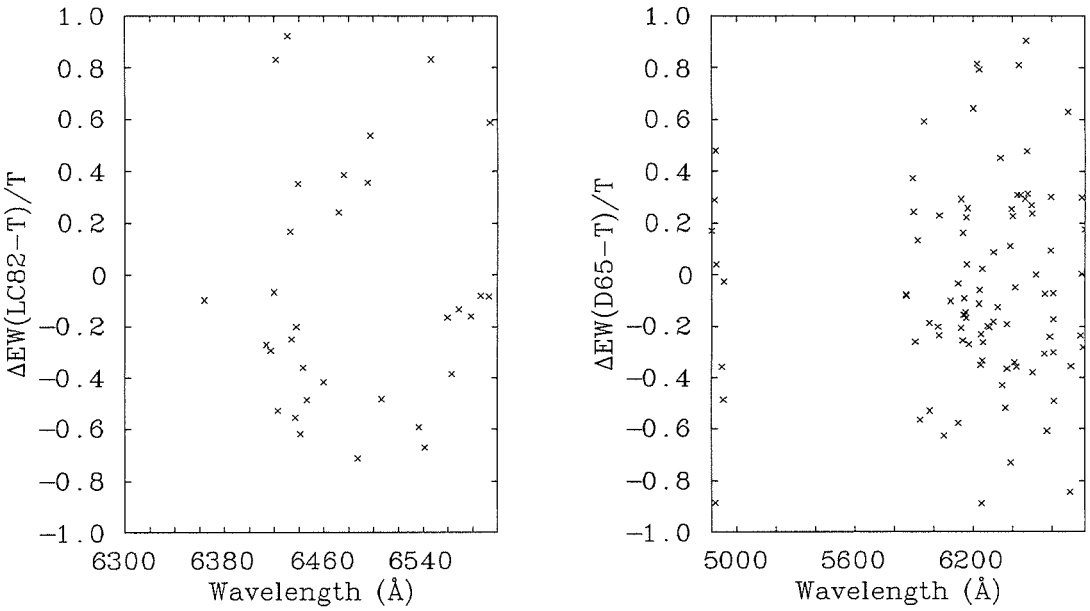

Figure 6.4: The residuals as a function of wavelength for CL82 and D65.

6.6.2 Radial Velocity

The radial velocity was obtained from the Fe I lines and was found to be 16.4 ± 0.2 km s^{-1}.The heliocentric velocity for J.D. 2447784 was calculated using the program OBSDAT supplied by Dr. P. Hill and was found to -26.9 km s^{-1}. Thus the heliocentric radial velocity of RY Sgr is -10.5 ± 0.2 km s^{-1}. This is in agreement with the value quoted in Drilling and Hill (1986).

6.6.3 Line Splitting

Observations by CL82 found that the weak metal lines were split into doublets. This was subsequently found to be due the presence of a shock wave passing through the atmosphere. Lawson (1986) found that the presence of shock split lines occurred around the time of maximum light and persisted for about 0.25 of the cycle. This is illustrated in Fig. 6.5.

The linear piece-wise ephemeris is of the form

$$JD_n = JD_o + P.n \tag{6.2}$$

where $JD_o = 2433878.6$ and the period $P = 37.81$ were taken from Lawson (1990). The observations presented here were obtained on J.D. 2447784 (Table 6.1) corresponding to cycle number n=362 and phase 0.78. At this phase line splitting is not expected to be seen. Figure 6.6 shows the same wavelength region as that in Figure 6.5 and there is no evidence for the presence of line-splitting.

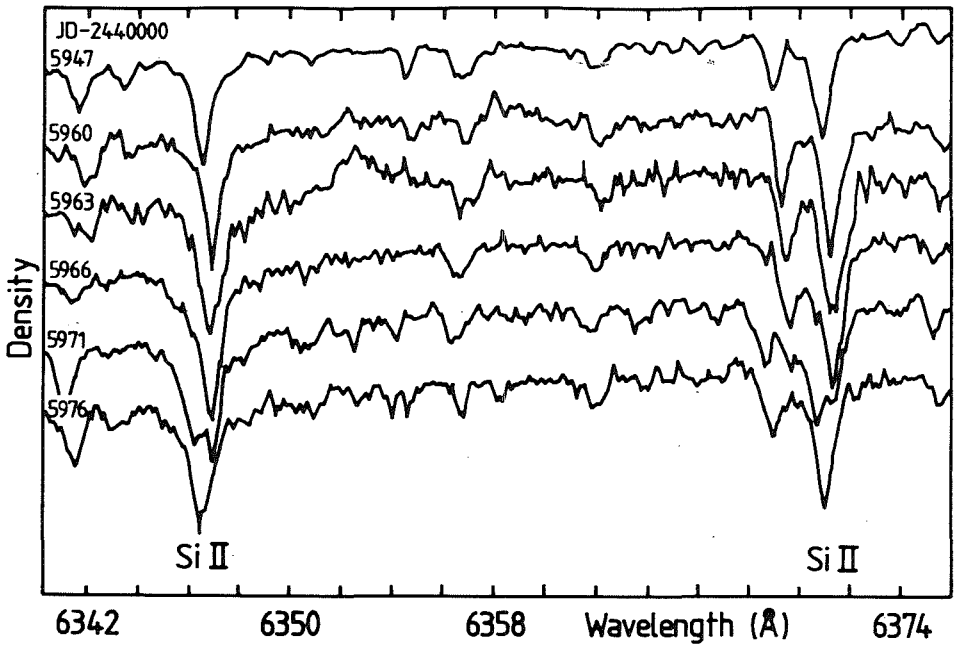

Figure 2. The evolution of the 6347Å and 6371Å Si II lines throughout the pulsation cycle.

Figure 6.5: Line splitting in RY Sgr taken from Lawson (1990).

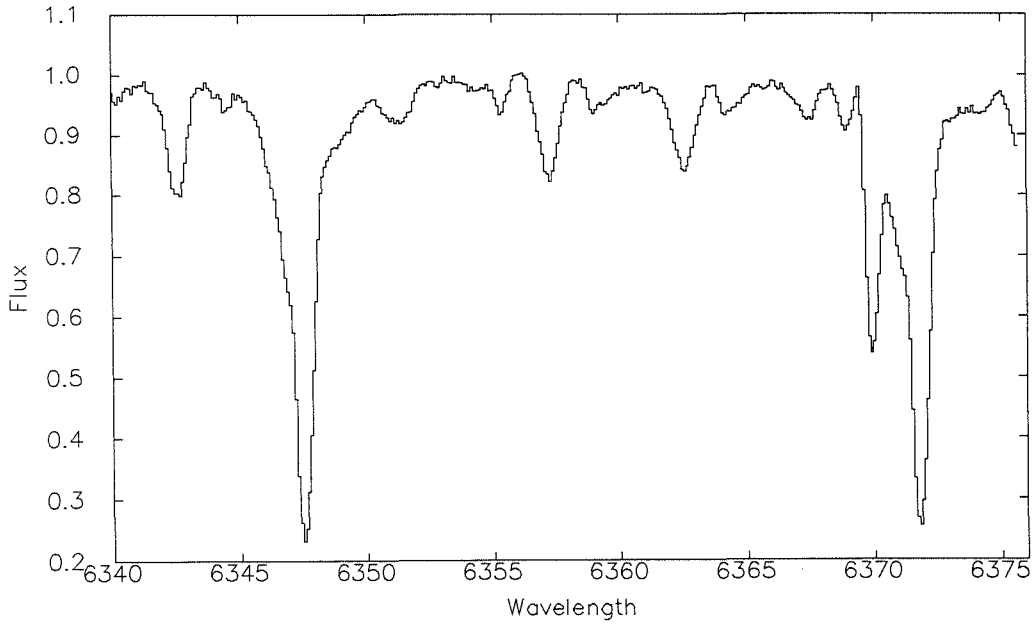

Figure 6.6: Spectrum showing absence of line splitting.

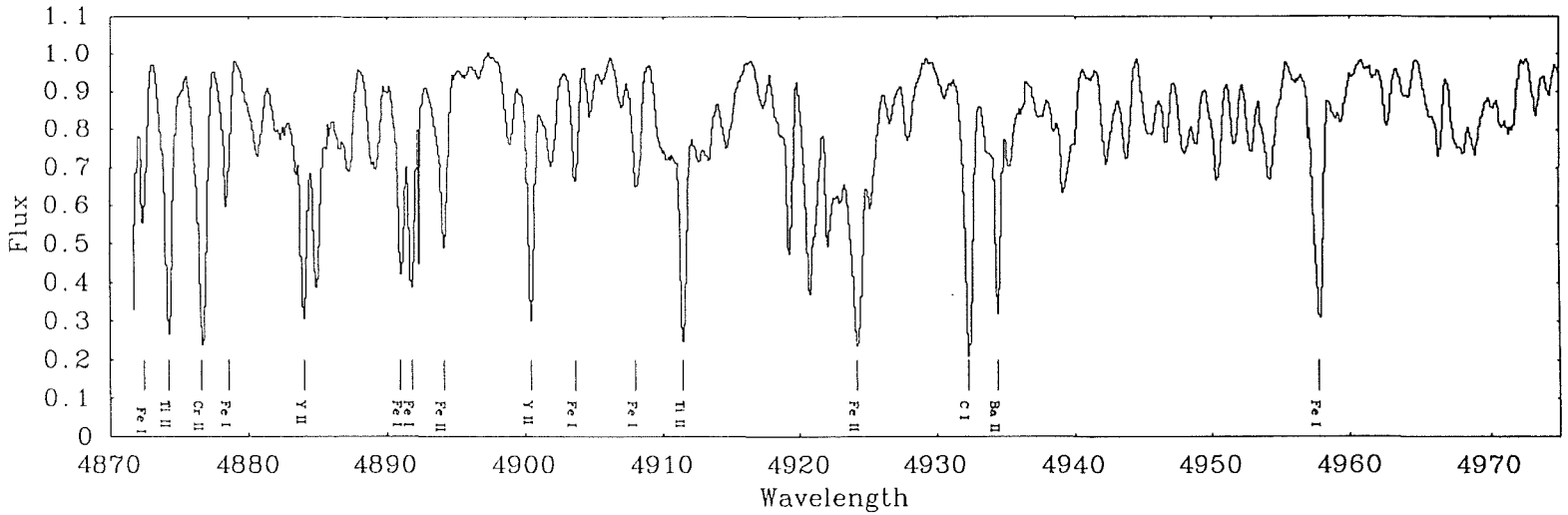

Figure 6.7: The spectrum of RY Sgr.

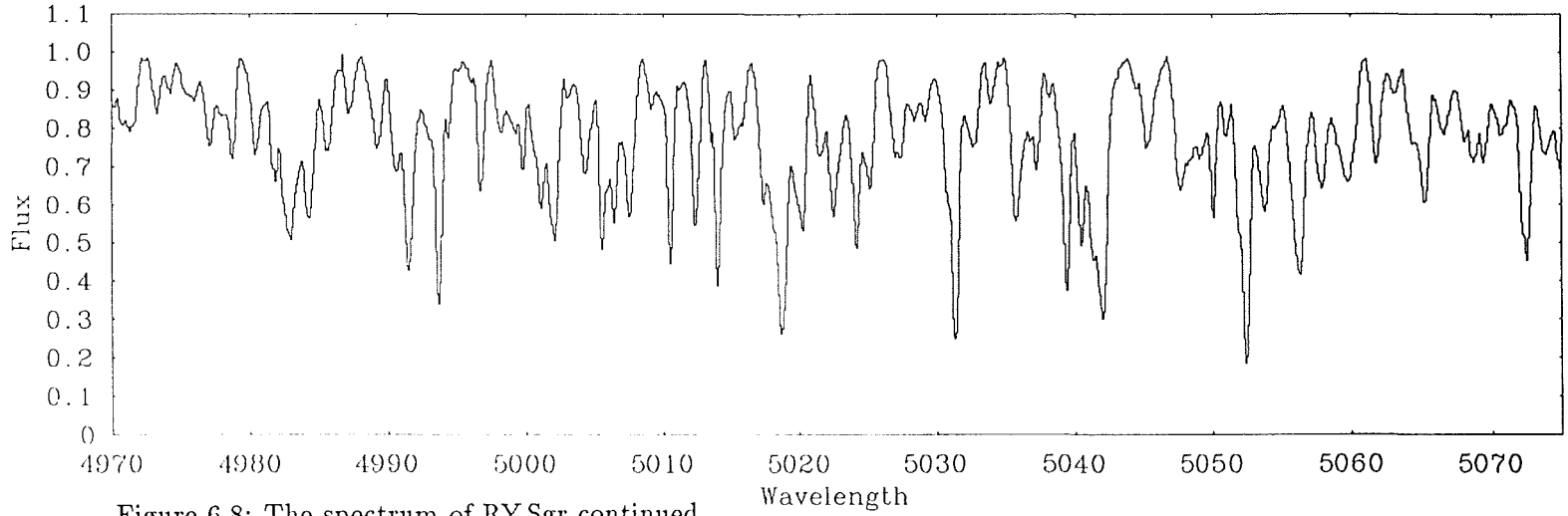

Figure 6.8: The spectrum of RY Sgr continued.

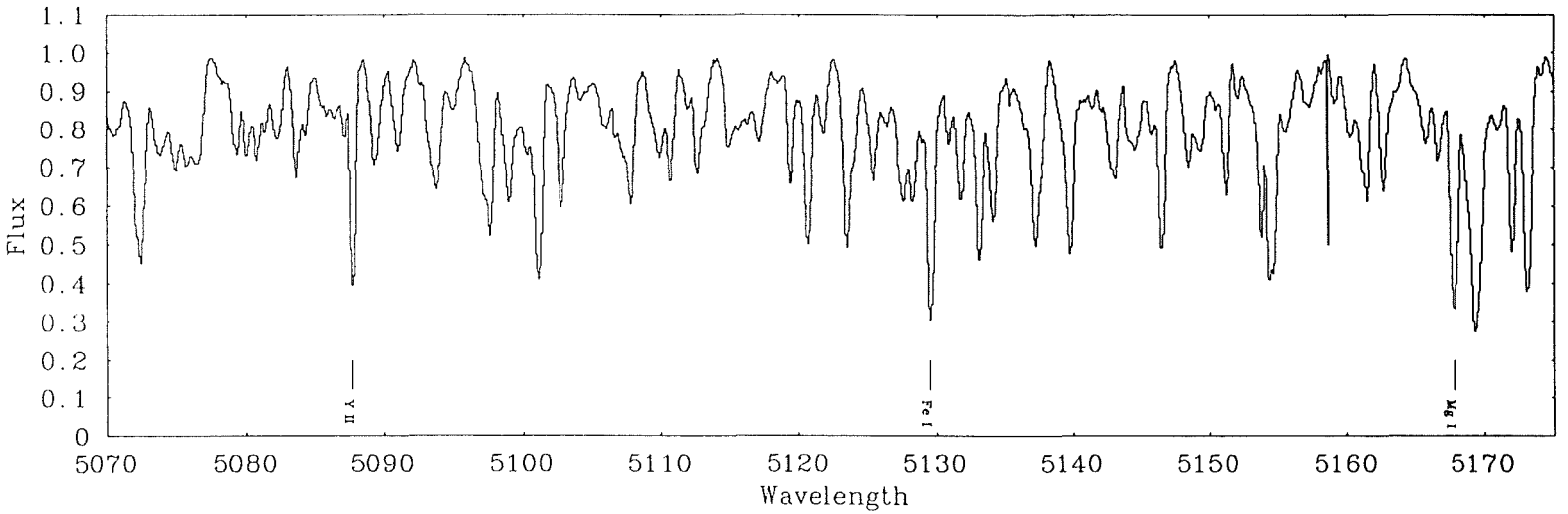

Figure 6.9: The spectrum of RY Sgr continued.

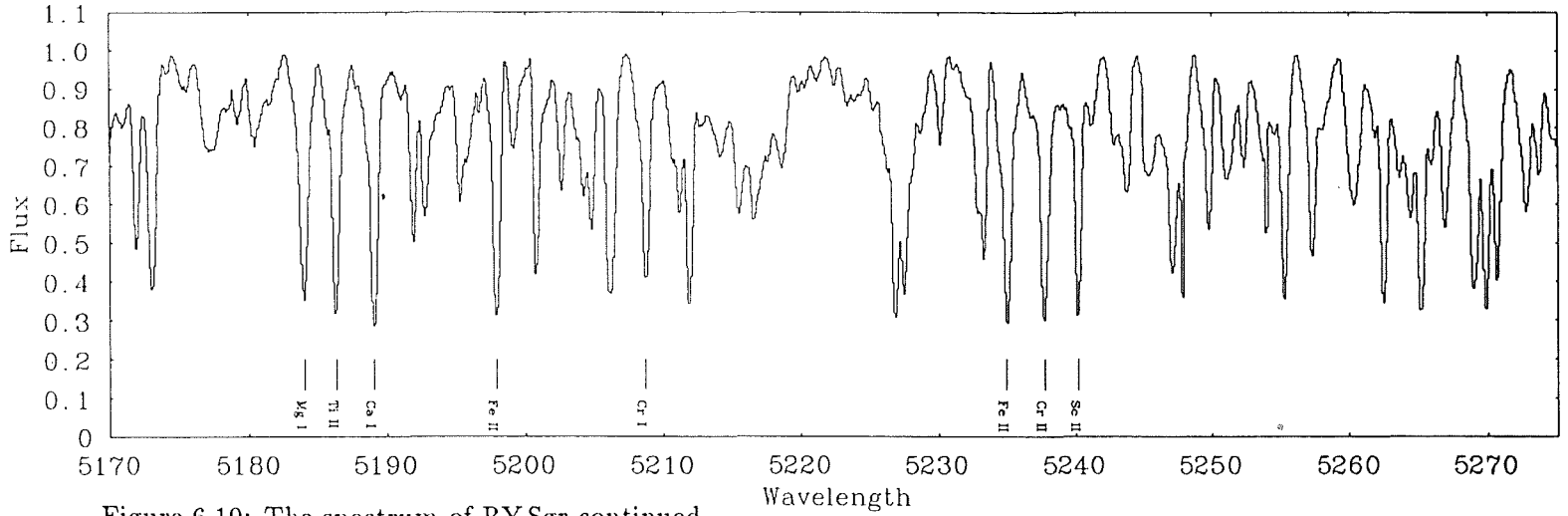

Figure 6.10: The spectrum of RY Sgr continued.

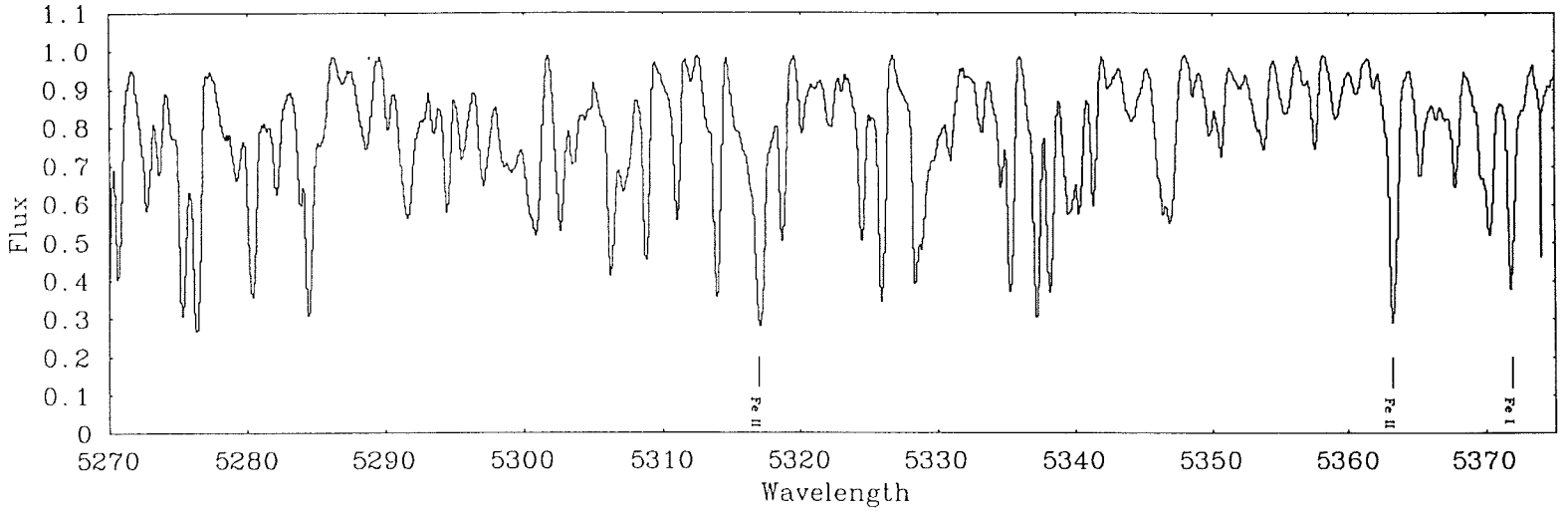

Figure 6.11: The spectrum of RY Sgr continued.

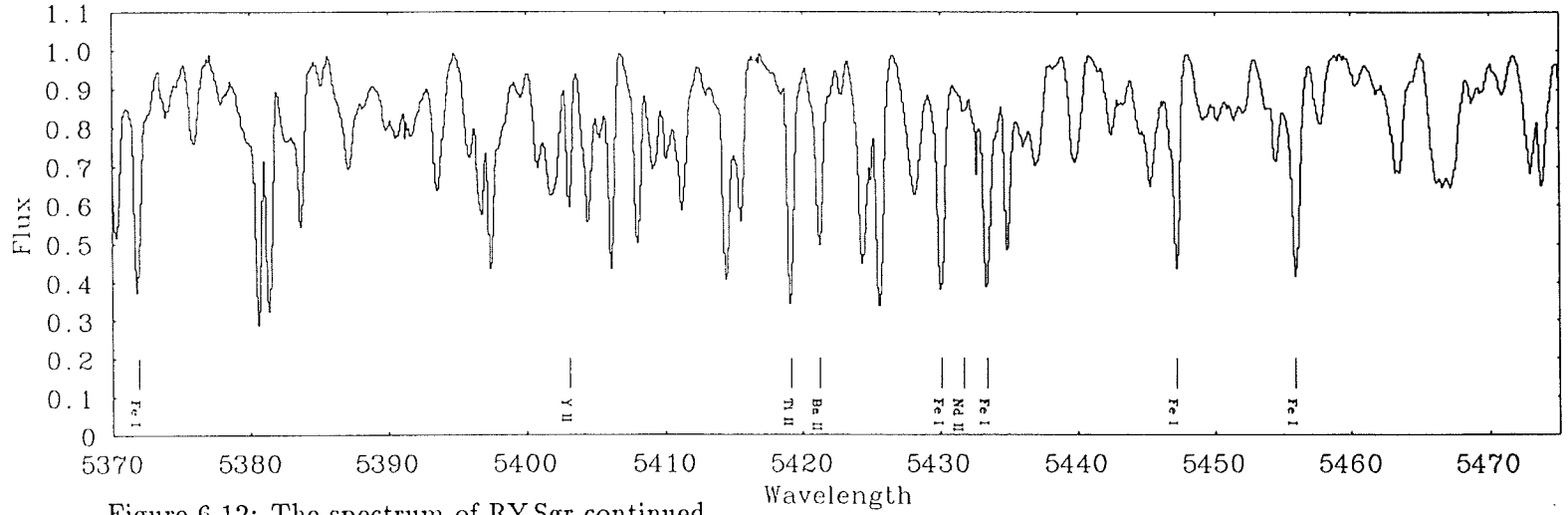

Figure 6.12: The spectrum of RY Sgr continued.

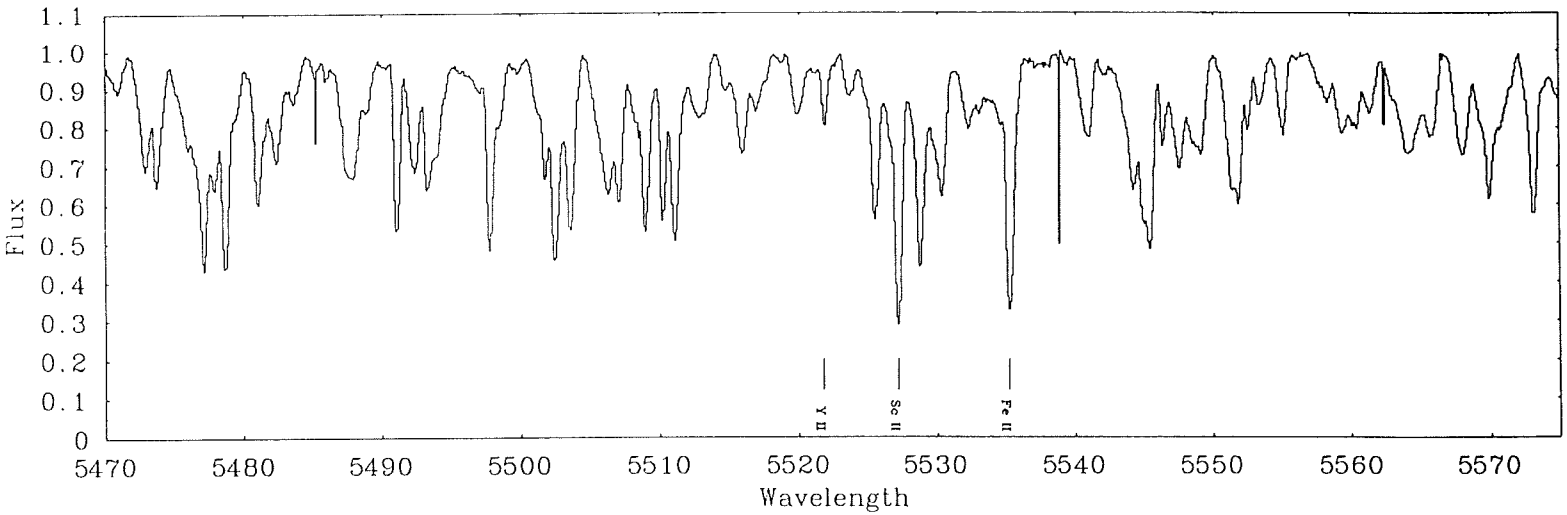

Figure 6.13: The spectrum of RY Sgr continued.

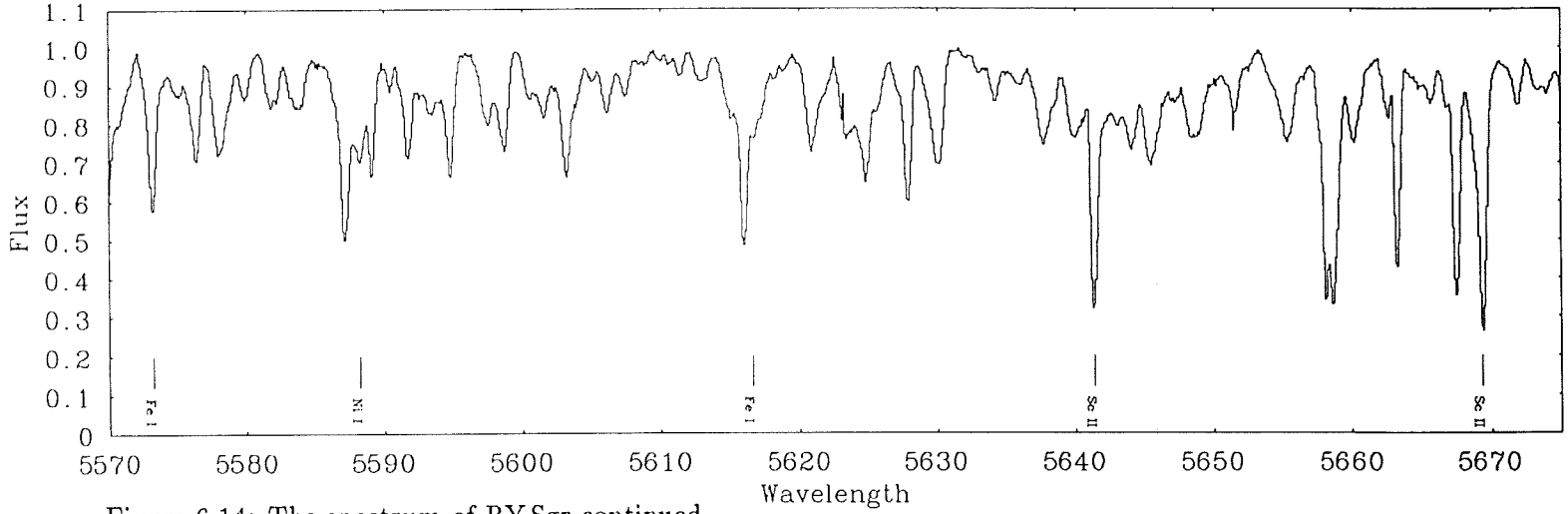

Figure 6.14: The spectrum of RY Sgr continued.

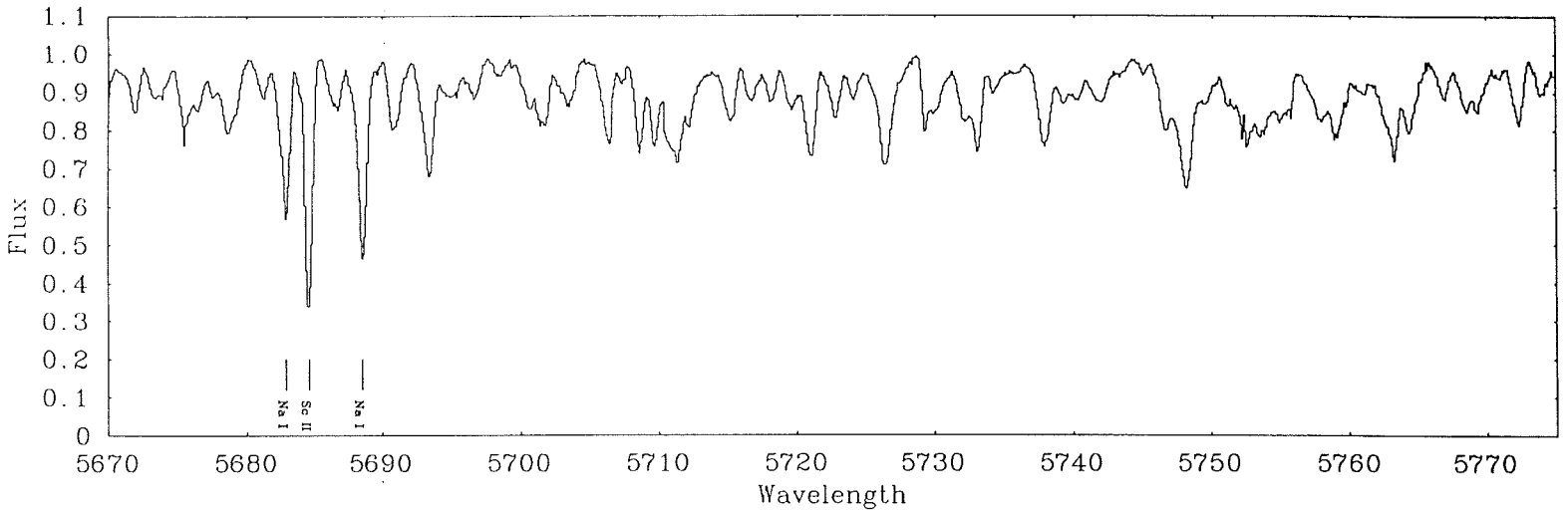

Figure 6.15: The spectrum of RY Sgr continued.

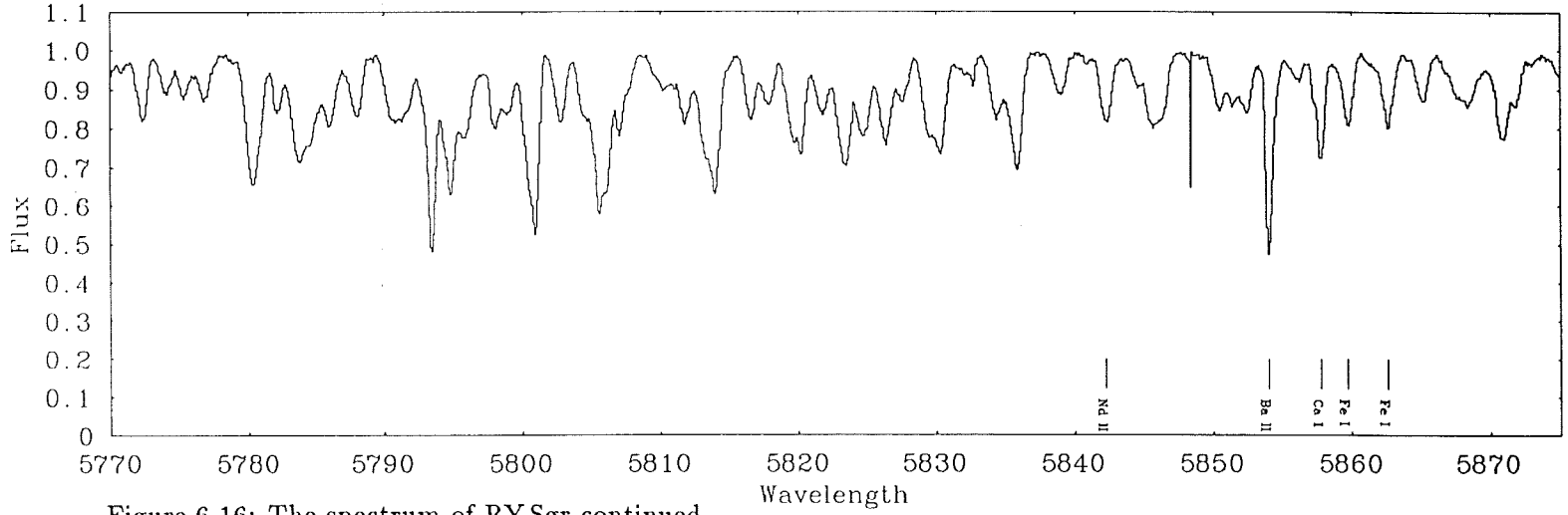

Figure 6.16: The spectrum of RY Sgr continued.

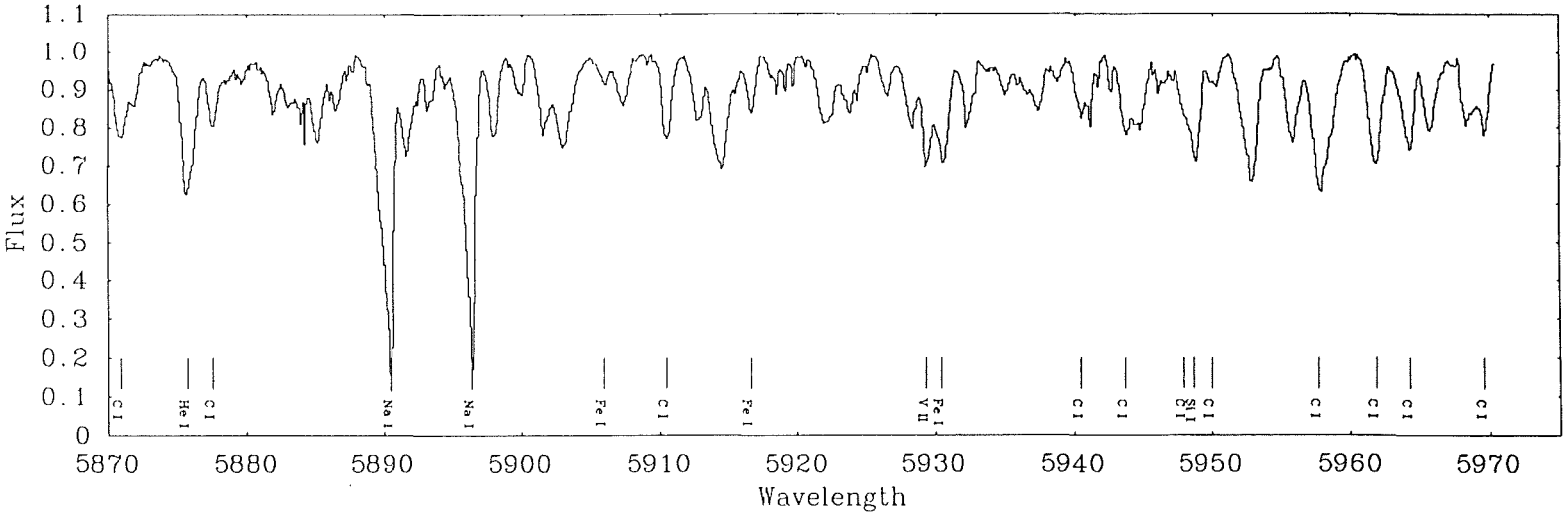

Figure 6.17: The spectrum of RY Sgr continued.

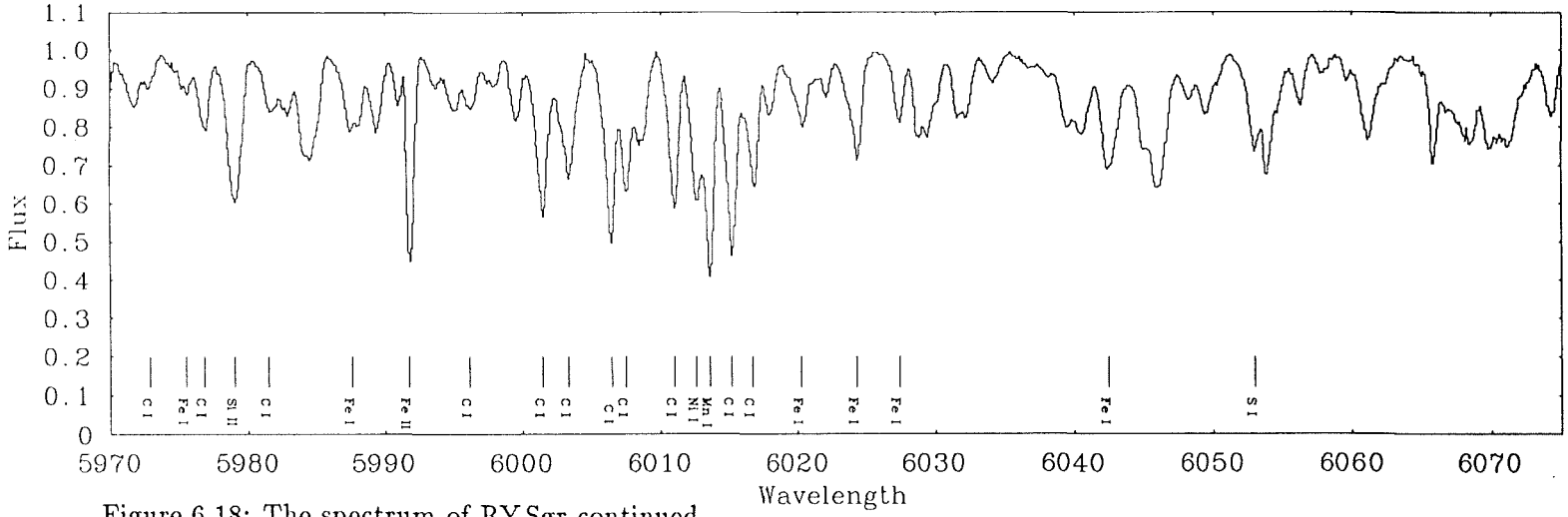

Figure 6.18: The spectrum of RY Sgr continued.

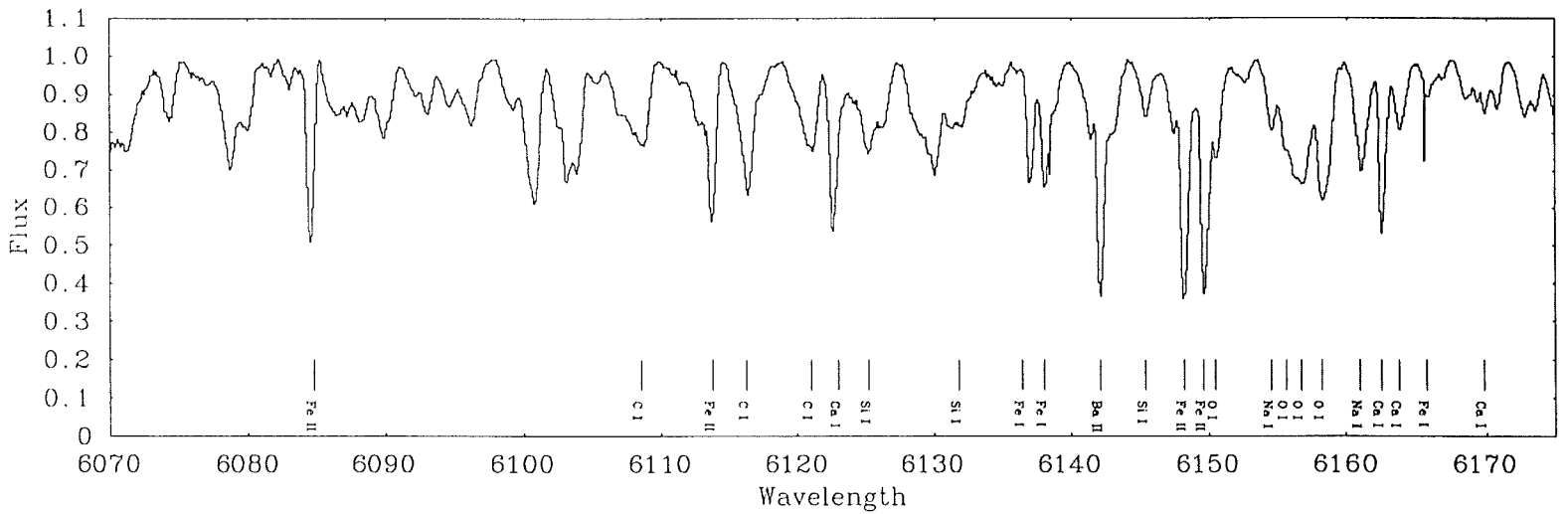

Figure 6.19: The spectrum of RY Sgr continued.

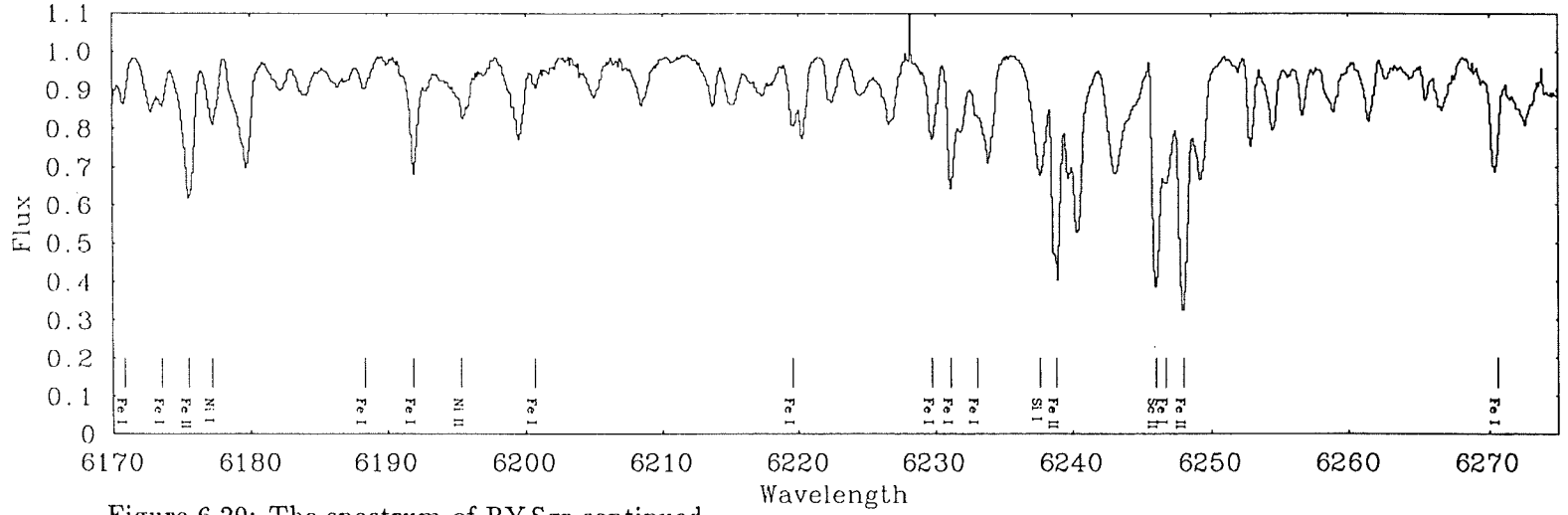

Figure 6.20: The spectrum of RY Sgr continued.

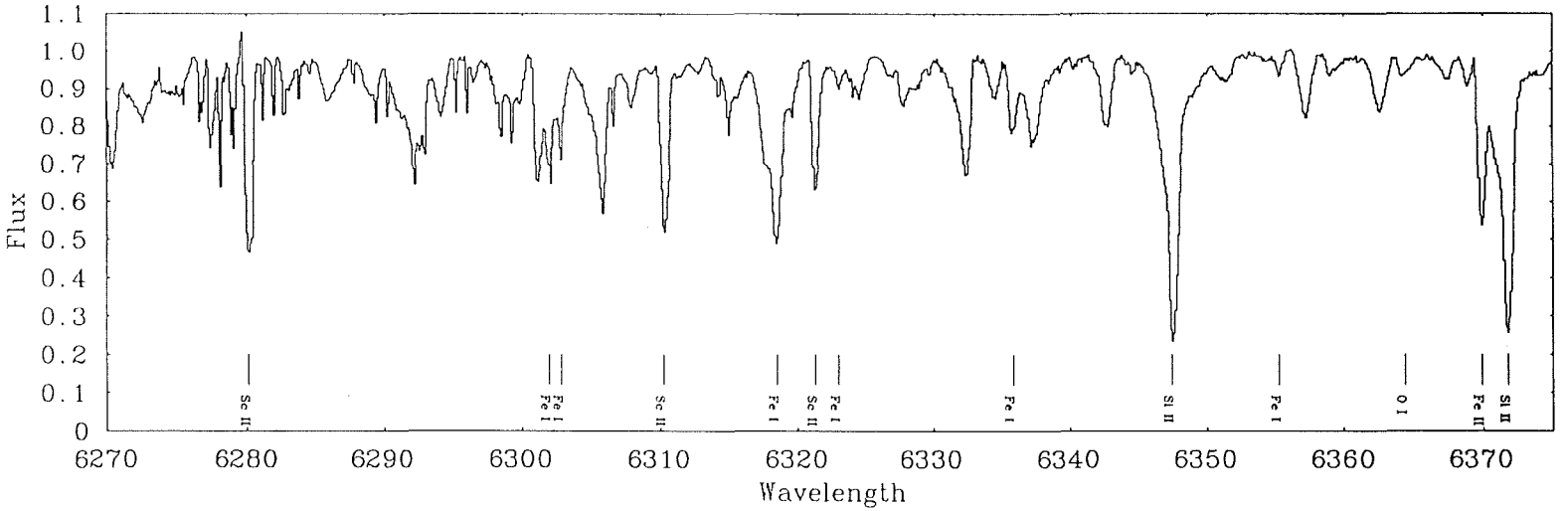

Figure 6.21: The spectrum of RY Sgr continued.

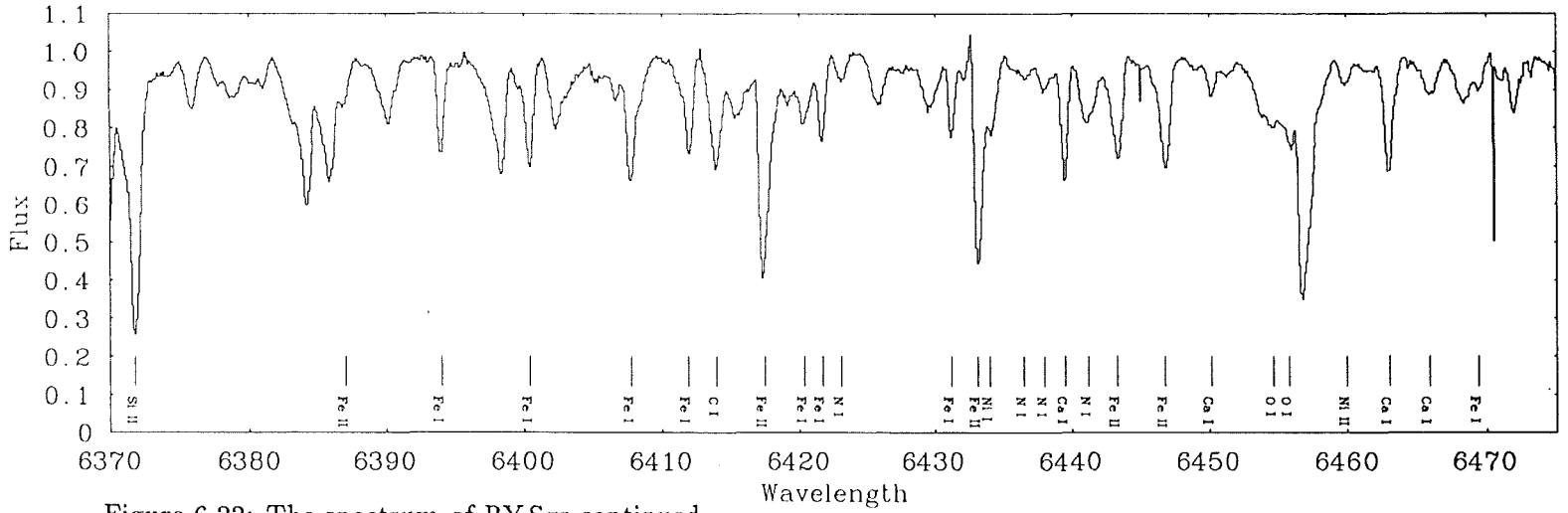

Figure 6.22: The spectrum of RY Sgr continued.

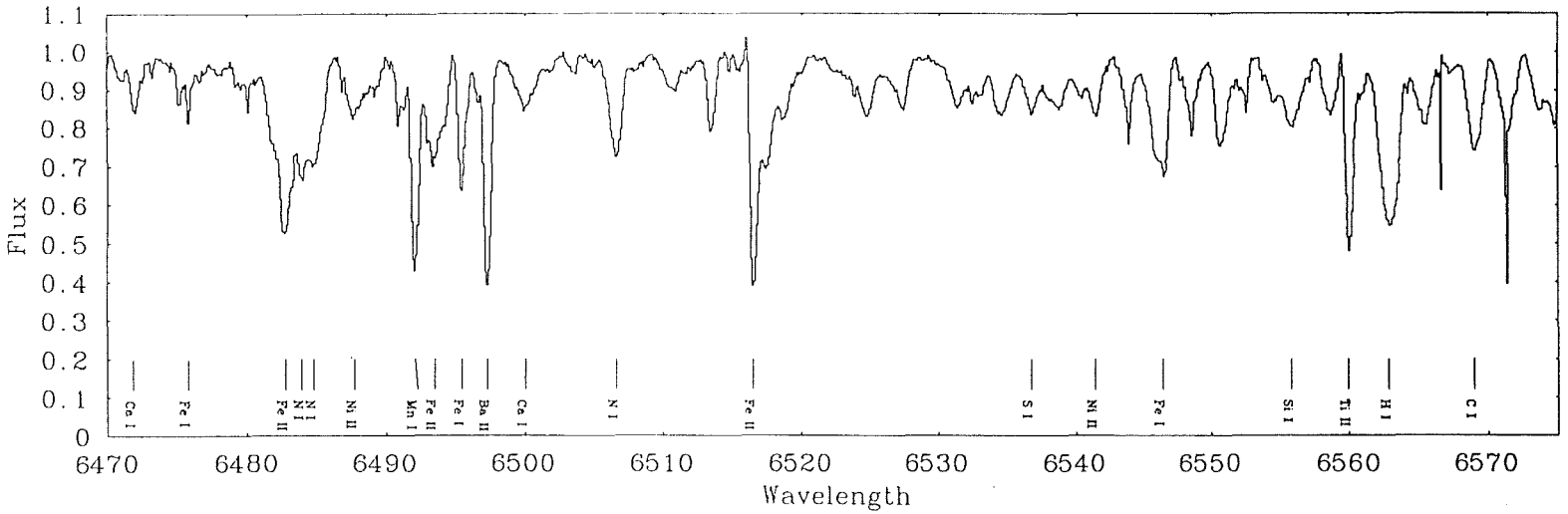

Figure 6.23: The spectrum of RY Sgr continued.

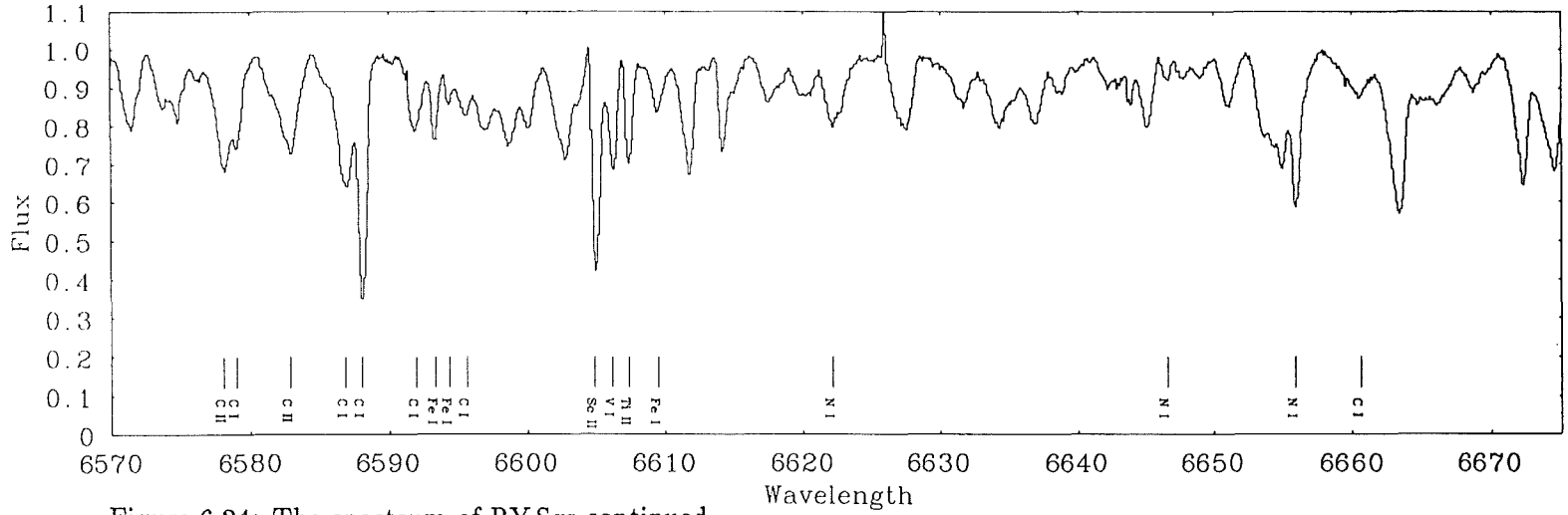

Figure 6.24: The spectrum of RY Sgr continued.

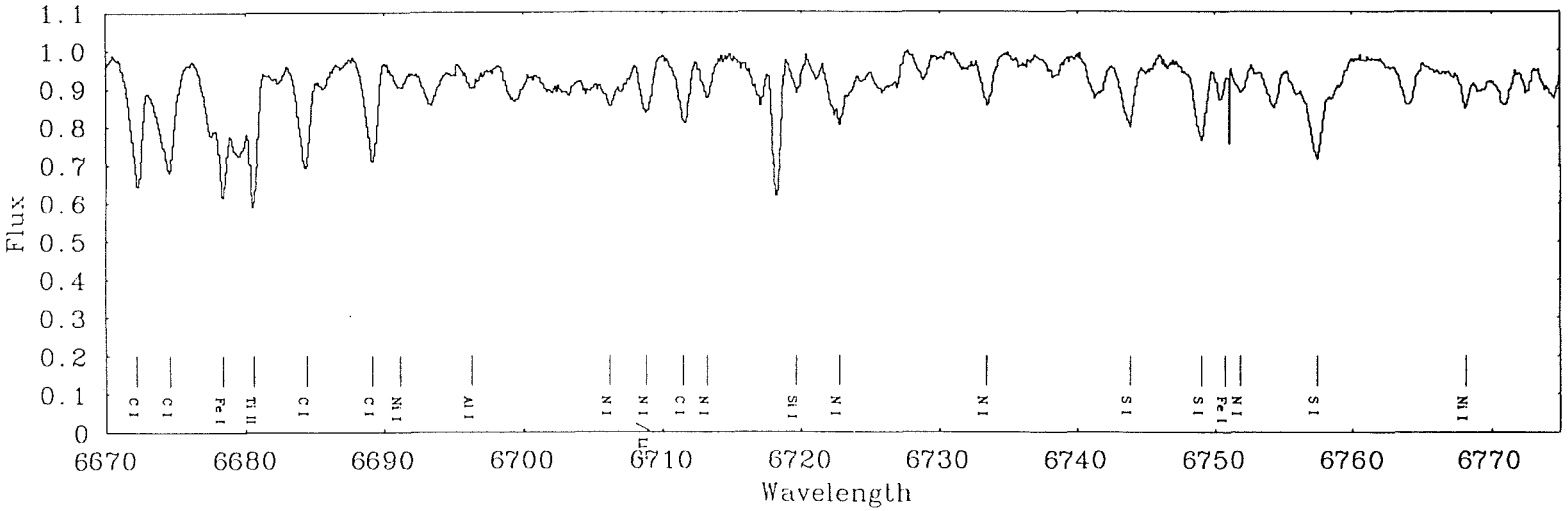

Figure 6.25: The spectrum of RY Sgr continued.

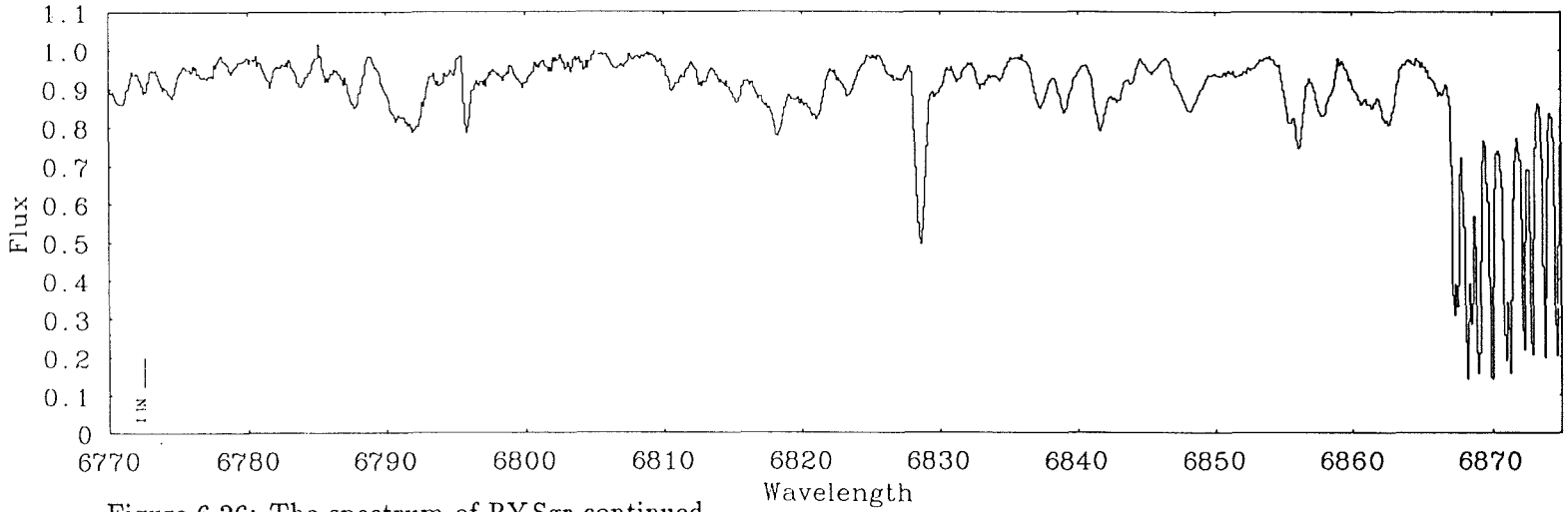

Figure 6.26: The spectrum of RY Sgr continued.

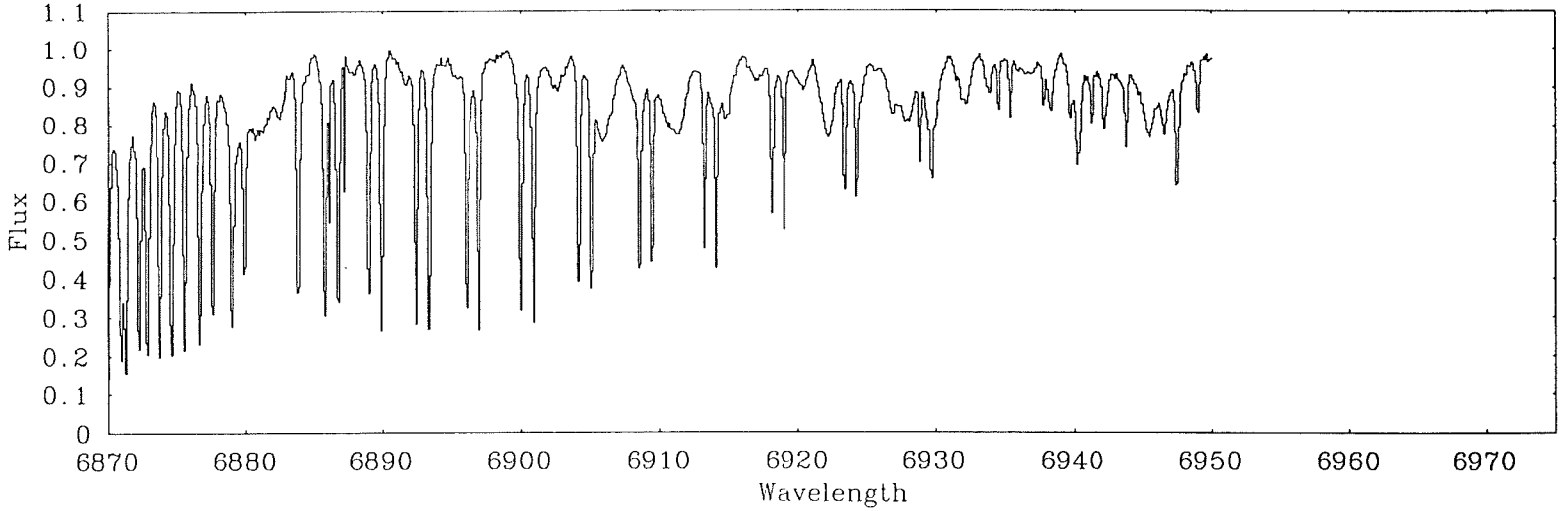

Figure 6.27: The spectrum of RY Sgr continued.

Table 6.2: Equivalent widths for RY Sgr.

Ion	Line	Multiplet	EP(eV)	$\log gf\lambda$	EW
H I	6562.81	1	10.2	4.53	777
He I	5875.630	11	20.9	4.51	456
C I	4932.00	13	7.65	1.91	648
	5912.58	71	9.00	...	203
	5940.10	26.12	8.64	1.41	168
	5943.39	70	0.09	2.32	187
	5947.61	26.12	8.64	...	247
	5950.04	21.11	8.64	1.64	95
	5957.56	26.11	8.64	1.70	
	5963.99	26.12	8.64	...	679
	5969.33	17.20	7.95	...	183
	5972.59	26.10	8.64	...	87
	5981.22	17.20	7.95	0.75	
	5996.06	26.08	26.08	...	217
	6001.13	26.07	8.64	1.69	462
	6002.98	26.08	8.65	...	384
	6006.03	26.08	8.65	...	513
	6007.18	26.07	8.64	...	223
	6010.68	26.07	8.64	...	383
	6108.53	36	8.85	...	
	6115.85	36	8.85	...	425
	6120.82	36	8.85	...	348
	6413.55	29.04	8.77	1.96	332
	6568.71	61	9.00	...	341
	6578.77	60	9.00	1.60	195
	6586.27	59	9.00	...	489
	6587.62	22	8.53	2.52	466
	6591.45	35	8.85	1.41	268
	6595.24	35	8.85	1.88	257
	6596.85	35	8.85	...	404
	6660.38	34	8.85	0.89	236
	6665.88	34	8.85	1.77	
	6671.84	33	8.85	...	404
	6674.11	33	8.85	...	462
	6683.95	33	8.85	1.80	345
	6688.79	33	8.85	1.85	323
	6711.29	21.01	8.54	...	200
C II	6578.05	2	14.45	3.90	385
	6582.88	2	14.45	3.60	449
N I	6423.03	21.03	11.76	1.59	70
	6436.71	21.01	11.76	2.42	101

Table 6.3: Equivalent widths for RY Sgr continued.

Ion	Line	Multiplet	EP(eV)	$\log gf\lambda$	EW
N I	6437.68	21.02	11.75	-0.88	125
	6440.94	21.03	11.76	2.67	289
	6483.75	21	11.75	2.77	142
	6484.80	21	11.76	3.05	421
	6506.31	21	11.76	0.44	319
	6622.54	20	11.76	2.29	276
	6646.50	20	11.75	2.16	67
	6656.51	20	11.75	2.16	372
	6706.11	59	11.84	2.03	194
	6708.76	59	11.84	2.04	185
	6713.11	59	11.84	1.02	132
	6722.62	59	11.84	2.85	162
	6733.32	58	11.84	2.04	146
	6752.03	58	11.84	2.50	152
O I	5958.48	23	10.99	2.91	
	6155.98	10	10.74	3.09	
	6156.77	10	10.74	3.31	196
	6158.18	10	10.74	3.46	500
	6363.79	1F	0.02	-6.45	83
	6453.60	9	10.74	2.46	
	6454.45	9	10.74	2.68	
Na I	5682.63	6	2.09	3.39	296
	5688.21	6	2.10	3.67	441
	5889.95	1	0.00	3.75	1054
	5895.92	1	0.00	3.44	925
	6154.23	5	2.10	2.28	190
	6160.75	5	2.10	2.59	321
Mg I	5167.32	2	2.70	3.39	535
	5183.60	2	2.70	4.13	572
Al I	6696.03	5	3.14	2.26	157
Si I	5948.55	16	5.08	2.47	152
	6125.03	30	5.61	2.01	331
	6131.72	30	5.61	2.32	
	6145.02	29	5.61	2.28	153
	6237.34	28	5.59	...	391
	6555.47	62	5.98	2.68	
	6719.62	...	6.00	2.00	42
Si II	5978.91	4	10.07	4.00	495
	6347.09	2	8.09	...	1016
	6371.36	2	8.09	...	745

Table 6.4: Equivalent widths for RY Sgr continued.

Ion	Line	Multiplet	EP(eV)	$\log gf\lambda$	EW
S I	6052.66	10	7.84	...	364
	6536.36	...	8.05	2.63	235
	6743.58	8	7.86	3.21	243
	6748.78	8	7.87	3.35	274
	6757.20	8	7.87	3.61	375
Ca I	5188.85	49	2.92	3.75	528
	5857.45	47	2.92	4.04	200
	6122.23	3	1.89	3.53	356
	6162.18	3	1.90	3.75	284
	6163.76	20	2.52	2.75	199
	6169.56	20	2.52	3.42	155
	6439.08	18	2.52	3.83	220
	6449.82	19	2.52	3.17	101
	6462.57	19	2.52	4.11	262
	6471.67	18	2.52	3.02	132
	6499.65	18	2.51	3.16	276
Sc II	5239.82	26	1.45	3.12	450
	5526.81	31	1.76	3.67	524
	5640.97	29	1.49	2.48	520
	5669.03	29	1.49	2.42	580
	5684.19	29	1.50	2.57	451
	6245.63	28	1.50	2.65	313
	6279.76	28	1.49	2.19	378
	6309.90	28	1.49	1.96	360
	6320.85	28	1.49	1.74	234
	6604.60	19	1.35	2.18	404
Ti II	4874.01	114	3.09	2.69	499
	4911.21	114	3.11	...	566
	5185.90	86	1.88	...	485
	5418.80	69	1.57	...	420
	6559.57	91	2.05	1.31	368
	6607.02	91	2.05	...	210
	6680.26	112	3.08	...	156
V I	6605.98	48	1.19	2.40	258
V II	5928.89	98	2.51	2.15	210
Cr I	5208.44	7	0.94	3.84	559
Cr II	4876.44	30	3.85	2.25	589
	5237.34	43			575

Table 6.5: Equivalent widths for RY Sgr continued.

Ion	Line	Multiplet	EP(eV)	$\log gf\lambda$	EW
Mn I	6013.50	27	3.06	3.63	396
	6491.71	39	3.75	3.52	401
Fe I	4872.14	318	2.88	3.13	323
	4877.61	384	2.99	...	244
	4890.76	318	2.86	3.58	407
	4891.50	318	2.84	3.91	346
	4903.32	318	2.87	3.04	218
	4907.74	687	3.42	...	291
	4957.30	318	2.84	3.61	654
	5129.66	965	3.93	...	505
	5371.49	15	0.95	2.16	428
	5429.70	15	0.95	1.98	473
	5432.95	1143	4.43	...	482
	5434.53	15	1.01	1.83	347
	5446.92	15	0.99	1.88	337
	5455.61	15	1.01	1.73	474
	5572.85	686	3.38	3.95	334
	5615.65	686	3.32	4.10	428
	5859.61	1181/165	4.55	3.02	183
	5862.36	1180/187	4.55	3.17	188
	5905.67	1181	4.65	2.87	81
	5916.26	170	2.45	0.91	120
	5930.16	1180	4.65	3.53	384
	5975.36	1017	4.83	2.86	97
	5987.06	1260	4.80	2.65	
	6020.17	1178	4.61	3.49	233
	6024.07	1178	4.53	4.21	267
	6027.06	1018	4.06	2.70	178
	6042.09	...	...	...	494
	6136.62	169	2.44	2.98	212
	6137.70	207	2.58	2.94	301
	6165.37	1018	4.14	2.35	76
	6170.52	1260	4.79	3.53	224
	6173.34	62	2.22	0.96	80
	6188.00	959	3.94	2.17	109
	6191.56	169	2.42	2.78	246
	6200.32	207	2.60	1.45	81
	6219.29	62	2.20	1.23	130
	6229.23	342	2.84	0.54	207
	6230.73	207	2.55	2.90	135
	6232.66	816	3.65	2.40	105
	6240.66	64	2.22	0.26	492

Table 6.6: Equivalent widths for RY Sgr continued.

Ion	Line	Multiplet	EP(ev)	$\log gf\lambda$	EW
Fe I	6246.33	816	3.59	3.48	365
	6270.24	342	2.85	...	277
	6301.52	816	3.64	3.46	238
	6302.51	816	3.69	2.52	160
	6318.02	168	2.44	2.19	113
	6322.69	207	2.58	...	97
	6335.34	62	2.19	...	186
	6355.04	342	2.84	1.45	42
	6393.60	168	2.43	1.97	165
	6400.01	816	3.59	3.84	233
	6408.03	816	3.67	...	281
	6411.66	816	3.64	3.68	204
	6419.96	1258	4.71	3.51	240
	6421.36	111	2.28	3.79	159
	6430.86	62	2.18	3.79	138
	6469.19	1258	4.83	3.15	62
	6475.63	206	2.56	1.02	96
	6494.99	168	2.39	2.92	245
	6546.25	268	2.76	2.16	101
	6574.24	13	0.99	-1.24	189
	6592.93	268	2.73	2.28	158
	6593.88	168	2.43	1.55	116
	6609.12	206	2.55	0.95	179
	6677.99	268	2.69	2.51	104
	6750.15	111	2.41	...	114
Fe II	4893.78	36	2.82	-0.59	341
	4923.92	42	2.88	2.80	1061
	5197.57	49	3.22	1.65	503
	5234.62	49	3.21	1.95	565
	5316.78	48	3.21	1.38	774
	5362.86	48	3.19	1.25	550
	5534.86	55	3.23	1.24	542
	5991.38	46	3.15	0.15	364
	6084.11	46	3.19	0.20	317
	6113.33	46	3.21	-0.04	324
	6147.74	74	3.87	1.27	271
	6149.25	74	3.87	1.02	364
	6175.16	200	6.22	1.59	402
	6179.40	163	5.57	1.22	
	6238.38	74	3.87	1.11	416
	6247.56	74	3.87	1.37	510
	6369.45	40	2.88	-0.24	352
	6386.75	203	6.77	...	81
	6416.93	74	3.89	1.08	535
	6432.68	40	2.89	0.17	351

Table 6.7: Equivalent widths for RY Sgr continued.

Ion	Line	Multiplet	EP(eV)	$\log gf\lambda$	EW
Fe II	6442.95	...	5.55	1.29	260
	6446.40	199	6.22	1.83	275
	6482.21	199	6.19		
	6493.06	...	5.58	1.33	
	6516.08	40	2.89	0.43	327
Ni I	5587.86	70	1.93	1.85	456
	6012.25	...	...	...	431
	6176.81	224	4.07	3.95	185
	6690.80	140	3.62	2.07	150
	6767.78	57	1.83	1.75	148
	6772.32	127	3.66	2.85	
Ni II	6195.36	...	14.50	...	
	6433.77	...	15.00	...	248
	6459.74	...	14.70	...	91
	6487.23	...	15.00	...	279
	6541.19	...	15.00	...	210
Y II	4883.69	22	1.08	3.23	445
	4900.13	22	1.03	2.91	467
	5087.42	20	1.08	2.84	324
	5402.78	35	1.84	3.30	213
	5521.59	27	1.74	2.83	113
Ba II	4934.09	1	0.00	2.52	421
	5421.05	6	5.70	...	363
	5853.68	2	0.60	2.50	351
	6141.73	2	0.70	3.72	261
	6496.91	2	0.60	3.38	417
Nd II	5431.53	80	1.12	3.69	
	5842.39	86	1.28	3.54	196
La II	6390				260

6.7 References

Barton J., Sadler E., (1990) *AAO Newsletter No.* **51**

Danziger I., (1965) *Mon. Not. R. astr. Soc.,* **130**, 199

D'Odorico S., Ghigo M., & Ponz D., (1987) *ESO Scientific Report No.* **6**

Drilling J.S., Hill P.W., (1986) *In IAU Coll. No.* **87**, *Hydrogen-Deficient Stars and Related Objects,* 499 eds. Hunger, K., Schönberner D. and Rao, N. Kameswara., Reidel

Horne K., (1986) *Publ. Astron. Soc. Pacific,* **98**, 609

Howarth I., & Murray J., (1988) *Starlink User Note* **50.11**

Keenan P.C., Greenstein J.L., (1963) Contib. Perkins Obs. Series **II**, No. 13

Cottrell P., Lambert D.L., (1982) *Astrophys. J.,* **261**, 595

Lawson W., (1986) *In IAU Coll. No.* **87**, *Hydrogen-Deficient Stars and Related Objects,* 211 eds. Hunger, K., Schönberner D. and Rao, N. Kameswara., Reidel

Lawson W., (1990) *The Characteristics of the Cool Hydrogen Deficient Carbon stars* (thesis) University of Cantabury

Moore C., (1959) *A Multiplet Table of Astrophysical Interest, N.B.S. Technical Note* **36**

Shortridge K., (1986) *Starlink User Note* **86.7**

Weise W.L., Smith M.W., Glennon B.M., (1966) *Atomic Transition Probabilites,* Vol**13**, (NSRDS-NBS4).

Chapter 7

Model Atmosphere Analyses of R CrB and RY Sgr

7.1 Introduction

R CrB and RY Sgr are two of the brightest (V=6.0 and 7.2) R CrB stars and consequently the best studied. R CrB was first analysed using the curve of growth technique (Mihalas 1978) by Searle (1961) and subsequently re-analysed by Schönberner (1975, S75) and Cottrell and Lambert (1982, CL82) using model atmospheres. RY Sgr was analysed using the curve of growth technique by Danziger (1965) and then re-analysed by S75. In both cases the first analyses obtained qualitatively correct results with the later analyses making quantitative determinations of the effective temperature, surface gravity and composition. The analyses of S75 and CL82 both used Schönberner's model atmosphere program STERNE.

One of the major difficulties in determining accurate atmospheric parameters for the R CrB and other cool stars is the measurement of equivalent widths (EW) due to the proximity of many close absorption lines. In order to reduce the amount of line blending CL82 chose to observe R CrB in the yellow-red wavelength region. They used a Reticon detector which enabled them to obtain higher signal to noise observations and consequently more accurate EWs. This resulted in reduced errors in the atmospheric

parameters in the analysis of CL82 compared with S75.

Although CL82 observed RY Sgr, they discovered that many of the metal lines showed time-dependent behavior and abandoned the analysis. Further observations by Lawson (1990) showed that the spectral variations were due to the presence of a shock wave travelling through the atmosphere. In the previous chapter it was shown that the observations of RY Sgr presented here were not affected by the shock wave due to the phase in the pulsation cycle at which the observations were made.

In the following sections the details of how the atmospheric parameters may be obtained from the measured EWs are presented together with the analyses of R CrB and RY Sgr. R CrB is re-analysed to compare the effects of using two different sets of models.

7.2 The line formation program SSG.

The program SSG (Bell 1975) was chosen as a basis from which to calculate EWs. Although the program was originally designed for spectrum synthesis and opacity distribution function calculations only minor modifications were needed to enable it to calculate EWs. It complements the model atmosphere programs MARCS and KMARCS in using the same continuous opacity sources. In general, model atmosphere and line formation programs will not calculate the same total continuous opacity for the same set of physical conditions due to their use of different individual opacity sources and different authors calculated opacities. Individually these differences are small but if the atmosphere is hydrogen-deficient then they become important. This was highlighted by CL82 who found that their line formation program calculated the total continuous opacity some 50% less than that used in the model atmosphere program STERNE which calculated their models. This will seriously affect the derived abundances, introducing systematic errors, and to a lesser extent the derived atmospheric parameters.

In Chapter 5, KMARCS model temperature structures were compared with those obtained from STERNE. The major difference, not including the effects of line blanketing, was the greater extension of the STERNE model. Although the number of depth

points and consequently the degree of extension may be increased in KMARCS, it is only worth doing so if the outermost layers significantly contribute to the calculated EW.

In order to determine the number of depth points required two hydrogen-deficient models with the same parameters and differing numbers of depth points were calculated. The first had the usual 35 points from $\log\tau = 1.0$ to -4.2 and the second 40 points from $\log\tau = 1.0$ to -5.8. The EW of a theoretical line was calculated for each model. The theoretical line was given excitation energies of $\chi = 0.5$, 2.5 and 5.0eV and oscillator strengths of $\log gf = -1.5$ and 1.5. The calculated EWs showed no dependence on the number of depth points used, the maximum difference in EW being less than 1%. On the basis of these results KMARCS models were calculated using only 35 depth points.

7.3 The Determination of the Atmospheric Parameters.

In chapter 5 it was shown that the structure of hydrogen-deficient models is determined by H/He and C/He in addition to the usual temperature and gravity parameters. These additional parameters arise because the most abundant species, He, is not the major opacity source. The analyses of R CrB and RY Sgr (CL82 and S75) have shown that H/He << C/He and consequently only C/He is important in determining the atmospheric structure. Hydrogen may then effectively be treated as a metal. However this is not likely to be case for all R CrB and HdC stars as the observations of NSV 6708 (Kilkenny and Marang 1989) and HD 148853 (Warner 1967) have shown them to be only slightly hydrogen-deficient. In these cases both C/He and H/He will need to be determined simultaneously with temperature and gravity.

7.3.1 The Effective Temperature

The temperature is determined from the requirement that the derived abundance of any line in a given ionization stage be independent of the excitation potential, χ, of the line. In order to obtain an accurate temperature determination the species used should have lines with as large a range in χ as possible.

CL82 chose to use lines from O I as the primary temperature determinant with Fe I as a check. The lines of O I are attractive because of the large range in χ, $\delta\chi \sim 9$eV, due to the presence of a weak forbidden line. However this large range in χ is provided by a single line and therefore the temperature derived from O I will be very sensitive to errors in the EW of the forbidden line. For this reason and because the forbidden O I line in RY Sgr is severely blended, the O I lines were not used to determine the temperature.

The Fe I lines, although with a smaller range in χ, $\delta\chi \sim 4.5$eV, are more numerous and evenly distributed over the range of χ. The large number, ~ 50, minimises the errors in the measured EWs and gf values and should therefore provide an accurate temperature diagnostic.

A series of theoretical EWs is calculated for each line with differing abundances. The abundance of each line is then obtained from the measured EW by linear interpolation. In order to determine whether the derived abundance is independent of the excitation potential of the line the correlation coefficient, r, is calculated. This is given by

$$r = \frac{\sum(x_i - \bar{x})(y_i - \bar{y})}{(N-1)s_x s_y} \tag{7.1}$$

where x_i and y_i are the excitation potential and derived abundance of the line and s_x and s_y the respective sample standard deviations. If the correlation coefficient $r = 0$, then the derived abundance is independent of the excitation potential and if $|r| = 1$ they are linearly related.

7.3.2 The Surface Gravity

The surface gravity is determined from the requirement that the derived abundance of a species be independent of the stage of ionization used. This requires the species to have as many as possible lines in differing stages of ionization. The best species is Fe, with ~ 50 line in Fe I and ~ 10 lines in Fe II.

7.3.3 The Micro-turbulent Velocity

The micro-turbulent velocity, ξ_t is an additional parameter required to fit the observed EWs and acts as an additional broadening agent. The interpretation of ξ_t as small scale turbulence in the strict hydrodynamic sense is probably only true for some cases. In hot O and B type stars the need for ξ_t is removed when line formation takes into account NLTE effects. In many supergiant atmospheres ξ_t may exceed the sound speed, implying supersonic turbulence. Thus care must be taken in the interpretation of ξ_t, as micro-turbulence may be merely the result of the failure to treat the line formation process correctly.

The ξ_t is obtained from the requirement that the derived abundance of a species be independent of the reduced EW. The reduced EW is defined as $\log \mathrm{EW}/\lambda$. The C I lines are relatively insensitive to the temperature and gravity and highly sensitive to ξ_t and thus are used to obtain ξ_t.

7.3.4 The Carbon-Helium Ratio

In principle the C/He ratio may be directly obtained from the EWs of the observed He I lines. Unfortunately the high excitation energy of He I ($\chi \sim 20$eV) results in very weak lines. In addition over the wavelength region observed, only the He I 5876Å line is sufficiently strong and free from blends to enable its EW to be measured. A further line at 6678Å is too severely blended for measurement.

Doubt as to the accuracy of the C/He ratio determined from the He I lines is cast by the possibility of chromospheric contamination. Observations of R CrB by Querci and Querci (1978) and Zirin (1982) of the He I 10830Å line were inconsistent. In the former case the line exhibited a P Cygni profile attributed to circumstellar emission and the latter failed to detect it.

Upper and lower limits to C/He can be imposed following the arguments in S75. The upper limit arises from a consideration of the heavy metal (Z>16) abundances. Since the R CrB stars are not extreme population I objects, the heavy metal abun-

dances should not exceed the solar values. If C/He is too large then the derived metal abundances will exceed the solar values due to the large value of the continuous opacity. Thus the maximum C/He permitted is that which gives rise to the solar abundances.

The lower limit to C/He is obtained from the weak C I lines. If the C/He ratio is too small then the computed C I lines only match the observed lines for unrealistically large values of ξ_t.

7.4 A Re-Analysis of R CrB

A grid of models with C/He=0.004 was calculated with temperatures between 5000K and 8000K and with surface gravities of $\log g = 0.0, 0.5$ and 1.0. The measured EWs from CL82 were chosen in preference to those used by S75 for the reasons outlined earlier.

The Si I and Ca I lines were used to obtain an upper limit of C/He< 0.04 and the weak C I lines C/He> 0.001. The value of C/He=0.004 was chosen for the grid on the basis of lying within the limits given above and being the value obtained by CL82.

The effective temperature was found to be 7400 ± 500K and the surface gravity $\log g = 0.55 \pm 0.25$ from the Fe I and Fe II lines. The micro-turbulent velocity was $\xi_t = 8 \pm 2 \mathrm{kms}^{-1}$ from the C I, Fe I and Fe II lines. Figures 7.1 and 7.2 show the derived abundances as functions of the excitation potential and reduced EW. The atmospheric

Parameter	S75	CL82	This study
Temperature (K)	6900±600	7000±250	7400±500
Gravity (cms^{-2})	0.15±0.65	0.5±0.3	0.55±0.25
C/He	0.03	0.004	0.005
Micro-turbulence (kms^{-1})	6.5±1	8±1	8±2

Table 7.1: The derived parameters for R CrB.

parameters together with the values obtained in previous studies are shown in Table 7.1 and the abundances in Table 7.2. An extra model was calculated with the determined atmospheric parameters and this was then used to obtain the abundances. By using

Element	S75	CL82	This study
$[H/He]$	-4.7	-5.9	-5.4
$[Fe/Total]$	-0.6	-1.1	-0.4
$[C/He]$	0.9	0.0	0.0
$[C/Fe]$	1.7	1.5	1.0
$[N/Fe]$	...	1.1	0.1
$[O/Fe]$	...	0.9	0.2
$[Y/Fe]$	...	...	0.2
$[Nd/Fe]$	...	...	1.4
$[Ba/Fe]$	...	...	0.1

Table 7.2: Abundance ratios for R CrB relative to the solar abundances.

such a model to determine the abundances in preference to the closest model available in the grid possible systematic errors in the abundances should be minimised. Apart from the C/He ratio obtained by S75 there is good agreement between the three studies, at least to within the quoted errors.

7.5 The Analysis of RY Sgr

The analysis was carried out using the same methods outlined above and used for R CrB. The same grid of models and C/He=0.004 were used to determine the atmospheric parameters as in the case of R CrB. Limits to the C/He ratio were obtained from the silicon and calcium lines giving 0.002–0.03. The EWs used together with the associated atomic data are given in Tables 6.2–6.7 presented in Chapter 6. The derived parameters are $T_{eff} = 7000 \pm 500$K, $\log g = 0.65 \pm 0.25$ and $\xi_t = 10 \pm 2 \mathrm{kms}^{-1}$. The lack of correlation between the derived abundances and the excitation potential is shown in Figure 7.3 and between the derived abundances and the reduced EW in Figure 7.4. Again the abundances were obtained from a model calculated using the determined atmospheric parameters. These parameters together with the derived abundances are given in Tables 7.3 and 7.4 along with the values determined by S75.

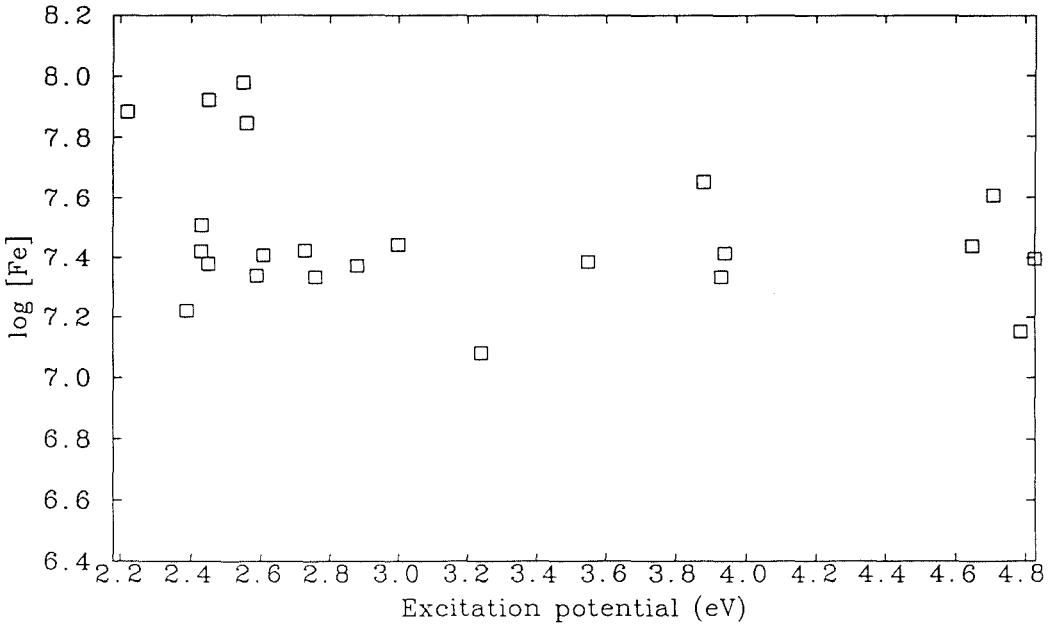

Figure 7.1: The derived abundances as a function of χ for R CrB.

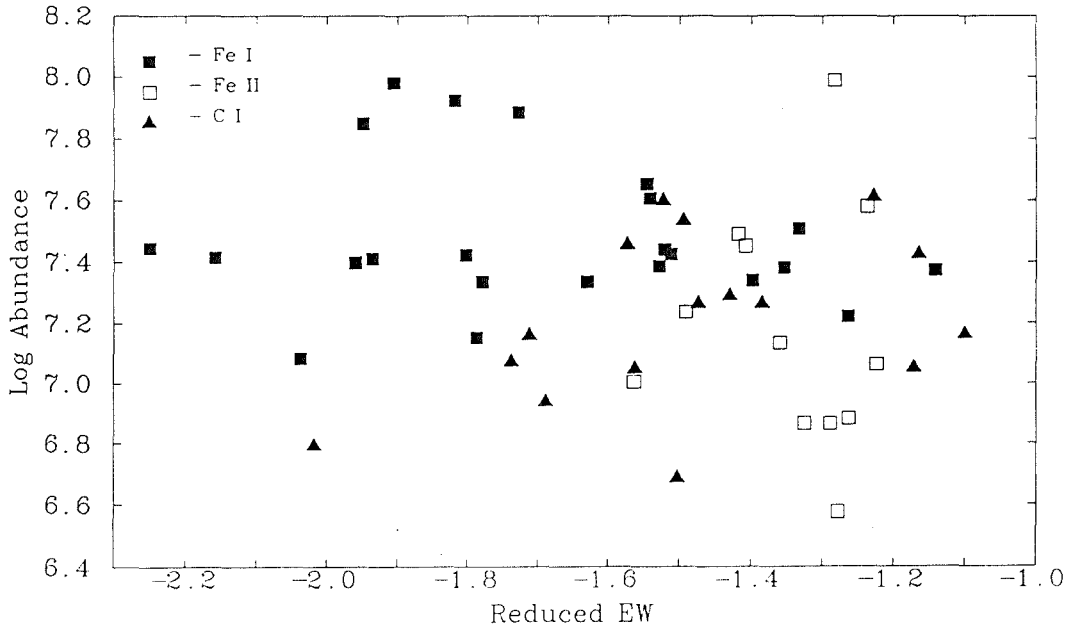

Figure 7.2: The derived abundances as a function of the reduced EW for R CrB.

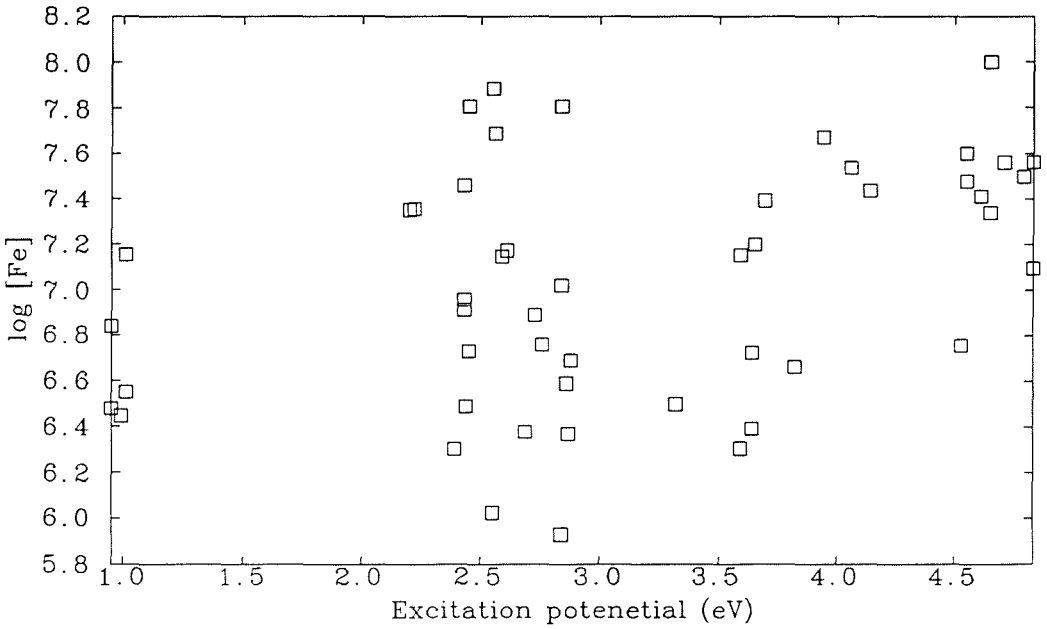

Figure 7.3: The derived abundances as a function of χ for RY Sgr.

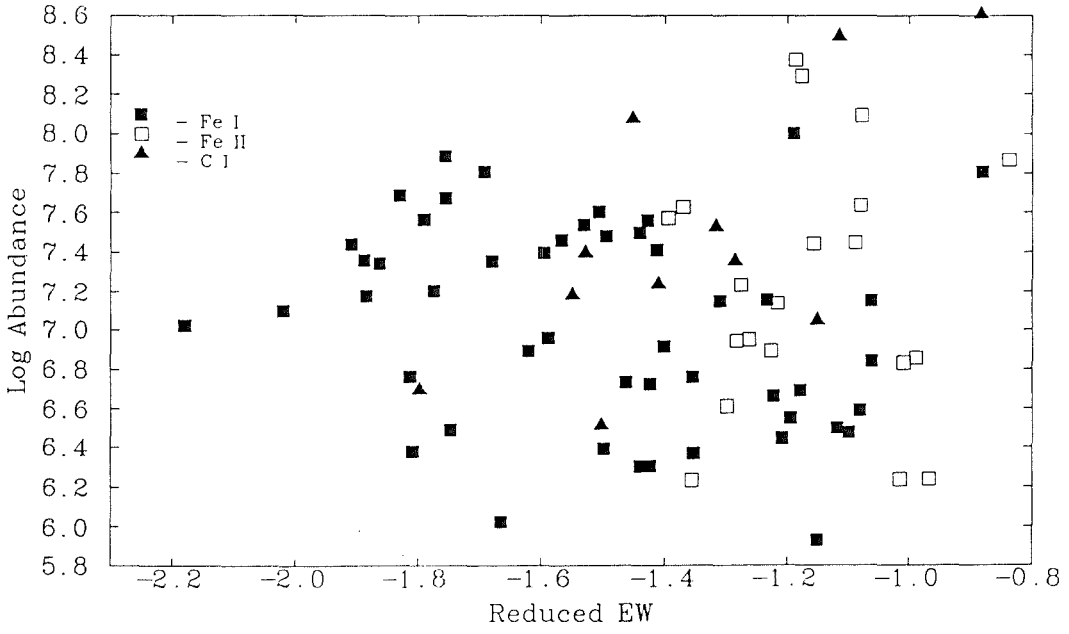

Figure 7.4: The derived abundances as a function of the reduced EW for RY Sgr.

Parameters	S75	This study
Temperature (K)	7100±600	7000±500
Gravity (cms^{-2})	0.10±0.65	0.65±0.25
C/He	0.03	0.005
Micro-turbulence (kms^{-1})	11.0±1	10±2

Table 7.3: The derived parameters for RY Sgr.

Element	S75	This study	Element	This study
$[H/He]$	-5.1	-4.4	$[S/Fe]$	0.6
$[Fe/Total]$	-0.4	-0.4	$[Ca/Fe]$	-0.3
$[C/He]$	0.9	0.1	$[Sc/Fe]$	0.6
$[C/Fe]$	1.5	1.0	$[Ti/Fe]$	0.9
$[N/Fe]$	...	1.7	$[V/Fe]$	0.5
$[O/Fe]$	-0.3	-0.2	$[Ni/Fe]$	1.4
$[Na/Fe]$	...	0.6	$[Y/Fe]$	0.4
$[Mg/Fe]$	...	1.5	$[Nd/Fe]$	1.9
$[Al/Fe]$	...	0.9	$[Ba/Fe]$	0.1
$[Si/Fe]$	...	0.4		

Table 7.4: Abundance ratios of RY Sgr relative to the solar abundances.

7.6 Error Analysis

Random errors arise mainly from the uncertainties in the measured EWs of the lines and the associated atomic data. The difficulties in obtaining accurate EWs have been discussed in Chapter 6 and are principally due to the difficulty in determining the continuum level. This is illustrated in Figures 6.1 and 6.2 which compared the values of the EW presented here with values obtained by Danziger (1965) and CL82. The atomic data required to calculate the EW are the oscillator strength, gf, and the excitation potential, χ which for many lines are unknown or derived from solar observations. Although the data used is the most recent available, the values may be uncertain by as much as 0.25 dex. A comparison of the values quoted in CL82 and those obtained from the compiled line list of Bell (1973) showed a scatter of $\sim$ 0.1 dex. The overall effect of these errors is to desensitize the atmospheric parameter diagnostics and increase the

derived abundance errors. To minimise these effects as many lines as possible should be used when determining these parameters.

As stated earlier, the temperature was determined from the requirement that the derived abundance of the FeI lines be independent of the excitation potentials. The correlation coefficient, r, was used to determine the temperature at which the correlation was a minimum. By using the correlation coefficient an estimate of the error in the temperature may be obtained. If the hypothesis $H_0 : r = 0$ is considered, then for the 50 FeI lines, H_0 will be rejected at a significance level of 10% when $|r| > 0.24$ and 5% when $|r| > 0.28$ in favour of the alternative hypothesis $H_1 : r \neq 0$. From the range in values of r obtained from models with different temperatures the error in T may be found. For both R CrB and RY Sgr $\delta T = \pm 500$K from the use of the 5% significance level.

The error in the derived gravity is obtained from the error in the derived FeI abundance and was found to be ± 0.25.

The error in the micro-turbulent velocity, ξ_t, was found using the same method employed to determine the error in the temperature. The error for a single species was found to be $\sim 1\text{kms}^{-1}$ but a large variation was found between different species. In the case of RY Sgr, ξ_t=7 (C I), 10 (Fe I) and 12kms^{-1} (Fe II), thus $\delta\xi_t = 2\text{kms}^{-1}$.

The most difficult error to try and quantify is the error in C/He. The upper and lower limits are wide and only the single He I 5876Å line is available for a direct determination of the ratio. The value obtained from the He I line is consistent with these limits but may be unreliable due to the possible NLTE effects discussed earlier.

The errors in the abundance determinations arising from errors in the atmospheric parameters are large but tend to be systematic, affecting all elements similarly. These errors may be minimised by comparing the ratios of the element abundances, then the estimated errors are ~ 0.25 dex. However, for the elements in which only a few strong lines have been used the errors are larger ~ 0.5 dex. The effects are summarised as follows, where $[X]$ is the abundance of a general element:

1. $\delta T = \pm 500K$, $\delta[X] \sim \pm 0.5$;

2. $\delta \log g = \pm 0.25$, $\delta[X] \sim \pm 0.05$;

3. $\delta \xi_t = 2 kms^{-1}$, $\delta[X] \sim \pm 0.1$;

4. C/He = 0.001 – −0.03, $\delta[X] \sim \pm 0.5$.

Note that the estimated errors due to uncertainties in $\delta \xi_t$ only apply to weak lines with EW< 250mÅ. The stronger lines are much more dependent on ξ_t and their associated errors are much greater. For this reason only the weak lines have been used to determine abundances when available.

7.7 Discussion

The atmospheric parameters derived for R CrB and RY Sgr are in agreement with those obtained by S75 and CLS2 to within the estimated errors. The main differences in the analysis of R CrB are C/He ratio and the surface gravity. In both cases it is the analysis of S75 which differs from the others. The only difference between the analysis presented here and that of CLS2 is a larger estimated error in the derived temperature. The lower C/He ratio obtained here and in CLS2 is due to the use of weaker C I lines.

The differing $[Fe/Total]$ ratios obtained make it difficult to directly compare the C, N and O abundances. However all three elements are overabundant in comparison with the solar values. Of more interest is the ratio C:N:O which may then be directly compared with the solar value and those predicted from the calculations of nuclear burning. For R CrB and RY Sgr the ratios are C:N:O=10:1:5 and C:N:O=10:10:1 respectively whereas for the sun C:N:O=5:1:9. These ratios may be understood as resulting from a mixture of CNO cycle and 3α processed material. The former is rich in N but poor in C and O whereas the latter is rich in C and O. The presence of large quantities of nuclear processed material at the surface of these stars implies that at some earlier point of their evolution considerable mixing must have taken place. It is during this period of mixing that it is most likely that the hydrogen-deficiency will be created.

The metals in both R CrB and RY Sgr have solar abundances. However, it must be

remembered that the metal abundance was used to provide an upper limit to the C/He ratio. In determining this limit the assumption was made that the metal abundances did not exceed the solar values.

Only three s-process elements were identified in the spectra of R CrB and RY Sgr, yttrium Y, barium Ba and neodymium Nd. Yttrium and barium were found to have solar values but neodymium was over-abundant in both stars. However, this abundance was only based on one or two relatively strong lines and therefore is probably not significant.

Both the models and the EWs were calculated using the assumption that the atmosphere could be represented as a one dimensional plane parallel layer. This assumption is only valid when the extent of the photosphere, z, is small in comparison with the radius of the star, R. From the models of R CrB and RY Sgr, z was found to be $\sim 3\,R_{\odot}$. The evolution models of Schönberner (1975) and Weiss (1987) required masses of $\sim 1.0\,M_{\odot}$, thus z/R$\sim$ 0.03. The small value of z/R justifies the use of plane parallel atmospheres.

7.8 Conclusion

These results have proved insensitive to the use of different models, KMARCS as opposed to STERNE. The inclusion of line-blanketing and convection into the KMARCS models, although altering the temperature structure, does not alter the derived atmospheric parameters.

The large errors in the derived element abundances prevent a more thorough investigation as to the origins of the R CrB stars, although most of the theoretical models of R CrB progenitors are not sophisticated enough to make accurate predictions of observable quantities.

7.9 References

Bell R.A., (1973) *Mon. Not. R. astr. Soc.*, **164**, 197

Danziger I.J. (1965) *Mon. Not. R. astr. Soc.*, **130**, 199

Gustafsson B., Bell R., Erikson K., Nordlund A., (1975) *Astr. Astrophys.*, **42**, 402

Kilkenny D., Marang F., (1989) *Mon. Not. R. astr. Soc.*, **238**, 1p

Kurucz R.L., (1970) *SAO Spec Rept. No.* **309**

Lawson W. (1986) *In IAU Coll. No.* **87**, *Hydrogen-Deficient Stars and Related Objects*, 211 eds. Hunger, K., Schönberner D. and Rao, N. Kameswara., Reidel

Mihalas D., (1978) *Stellar Atmospheres*

Querci M., Querci F., (1978) *Astr. Astrophys.*, **70**, L45

Schönberner D., (1975) *Astr. Astrophys.*, **44**, 383

Warner B., (1967) *Mon. Not. R. astr. Soc.*, **137**, 119

Weiss A., (1987) *Astr. Astrophys.*, **285**, 165

Zirin H., (1982) *Astrophys. J.*, **260**, 655

Chapter 8

Identification of Suspected R CrB stars

8.1 Introduction

The 4^{th} edition of the General Catalogue of Variable Stars (Kholopov 1985) lists 37 stars as being members of the R CrB class. This classification is based upon their photometric behaviour which is often just a few observations which show that the star declined in brightness by a few magnitudes. For conclusive identification the suspected R CrB star must be observed through minima and whilst pulsating at maximum light. Failure to make sufficient observations results in the inclusion of other types of star in the R CrB class.

It would difficult and time consuming to follow all suspected R CrB stars photometrically in order to decide their identity on the basis of their light curves. However, as was stated in Chapter 1 the R CrB stars are hydrogen-deficient, hence spectroscopy may be used to determine their classification. If the star is hydrogen-deficient the hydrogen Balmer lines and the G band of CH should be very weak or absent.

There is some evidence that there exists a range of hydrogen-deficiency in both the HdC and R CrB stars. Warner (1967) found that the HdC star HD 148839 had a hy-

drogen abundance of [H/Fe]=-1.7 compared to the more typical values of [H/Fe]< −4.8. Similarly the R CrB star NSV 6708 (Kilkenny and Marang 1989) has relatively strong Balmer lines and possible weak CH bands at 4300Å (G band) and 4775Å (Figure 8.1). These observations complicate the task of classifying suspected R CrB stars purely on the basis of the presence/absence of hydrogen lines.

8.2 Observations and Reductions

Spectroscopic observations were obtained by Drs. Hill and Pollacco with the Isaac Newton telescope at the Observatorio del Roque de los Muchachos over four nights from 13th September 1987. The intermediate dispersion spectrograph (IDS) was used with the 1200 lines per millimeter grating to obtain spectra with a resolution of 1.5Å/pixel using the IPCS detector. Observations were obtained at central wavelengths of 4400Å and 5700Å for most stars.

Flat field frames together with copper-argon arc frames were obtained for the reduction process. In addition the two photometric standards EG 247 (Oke 1974) and BD +28 4211 (Stone 1977) were observed in each wavelength region to enable the spectra to be flux calibrated.

The reductions from two dimensional IPCS images to wavelength and flux calibrated spectra followed the usual method outlined below using the Figaro suite of programs (Shortridge 1986).

1. Each frame was divided by the normalised flat-field to remove the effects of differing pixel sensitivities.
2. The spatial positions of the star and sky were identified by hand and then extracted by summation.
3. The sky contribution was then subtracted.
4. The arc associated with each spectrum is extracted and then wavelength calibrated.

5. The wavelength scale is mapped onto the stellar spectrum.

6. The two flux standards were processed similarly. The published fluxes were used to create the calibration spectrum which was then divided into each of the stellar spectra. In principal this results in flux calibrated spectra but in this case due to non-photometric weather conditions during the observations the spectra have an arbitrary flux scale.

As an aid to classification the carbon stars, HR 690, HR 800, HR 849, HR 1602 were also observed together with the HdC star HD 182040 and the R CrB star XX Cam. These spectra together with those of the suspected R CrB stars are shown in igures 8.2 to 8.8

8.3 Analysis of spectra of suspected R CrB stars

8.3.1 BG Cep

The blue spectrum shows strong hydrogen Balmer lines with pressure broadened wings. The red spectrum shows Hα in strong emission. The spectral type of B8e was assigned to this star (Herbig 1960) and it is not a hot R CrB star as stated by Schaefer (1986).

8.3.2 LO Cep

Hydrogen lines are visible with Hα in weak emission . This is definitely not a R CrB star and was classified as A0-A5e.

8.3.3 CC Cep and DZ And

The blue spectra show weak Hβ and Hγ with Hα only visible in DZ And. The absence of Hα in CC Cep is most likely due to the low signal-to-noise ratio in that spectrum. The CH band at 4300Å is prominent in DZ And being slightly weaker but still visible

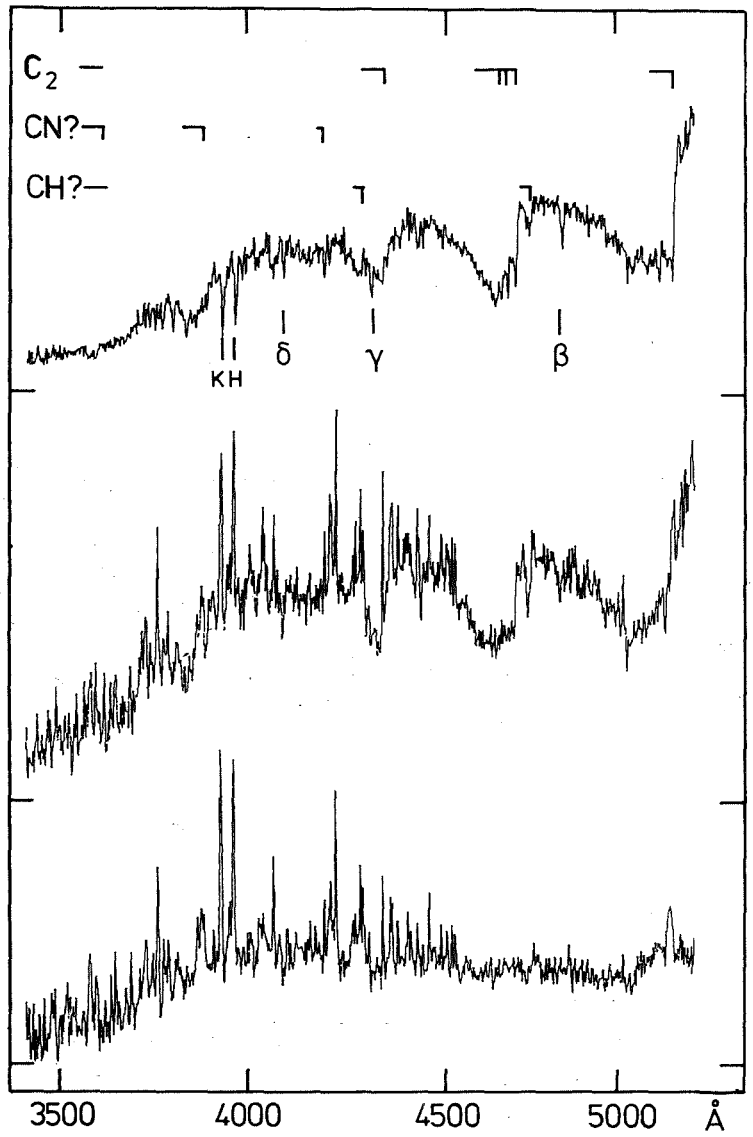

Grating 6 (100 Å mm^{-1}) spectrograms of NSV 6708 obtained on 1988 September 14, 17 and 19 47419, 7422 and 7424). The upper spectrogram, obtained on 14th, shows strong C_2 bands and the *H* ıes of Ca II; Balmer series lines β–δ are present and so are CN bands and, possibly, CH bands. The 7th) and lower (19th) spectrograms show the rapid development of the 'chromospheric' lines as the . (see text).

Figure 8.1: The spectrum of NSV 6708 taken from Kilkenny and Marang (1989).

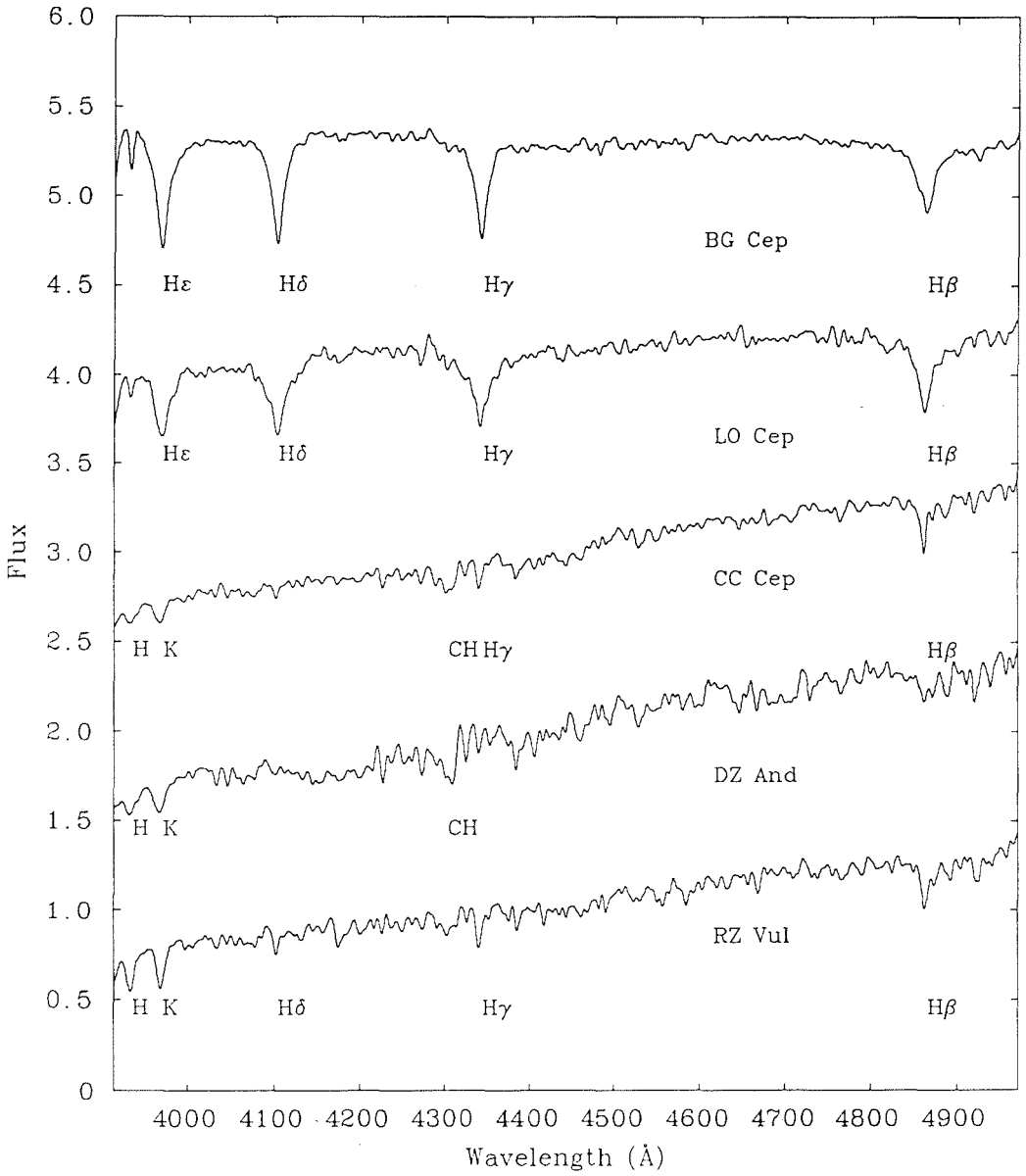

Figure 8.2: Blue spectra of suspected R CrB stars.

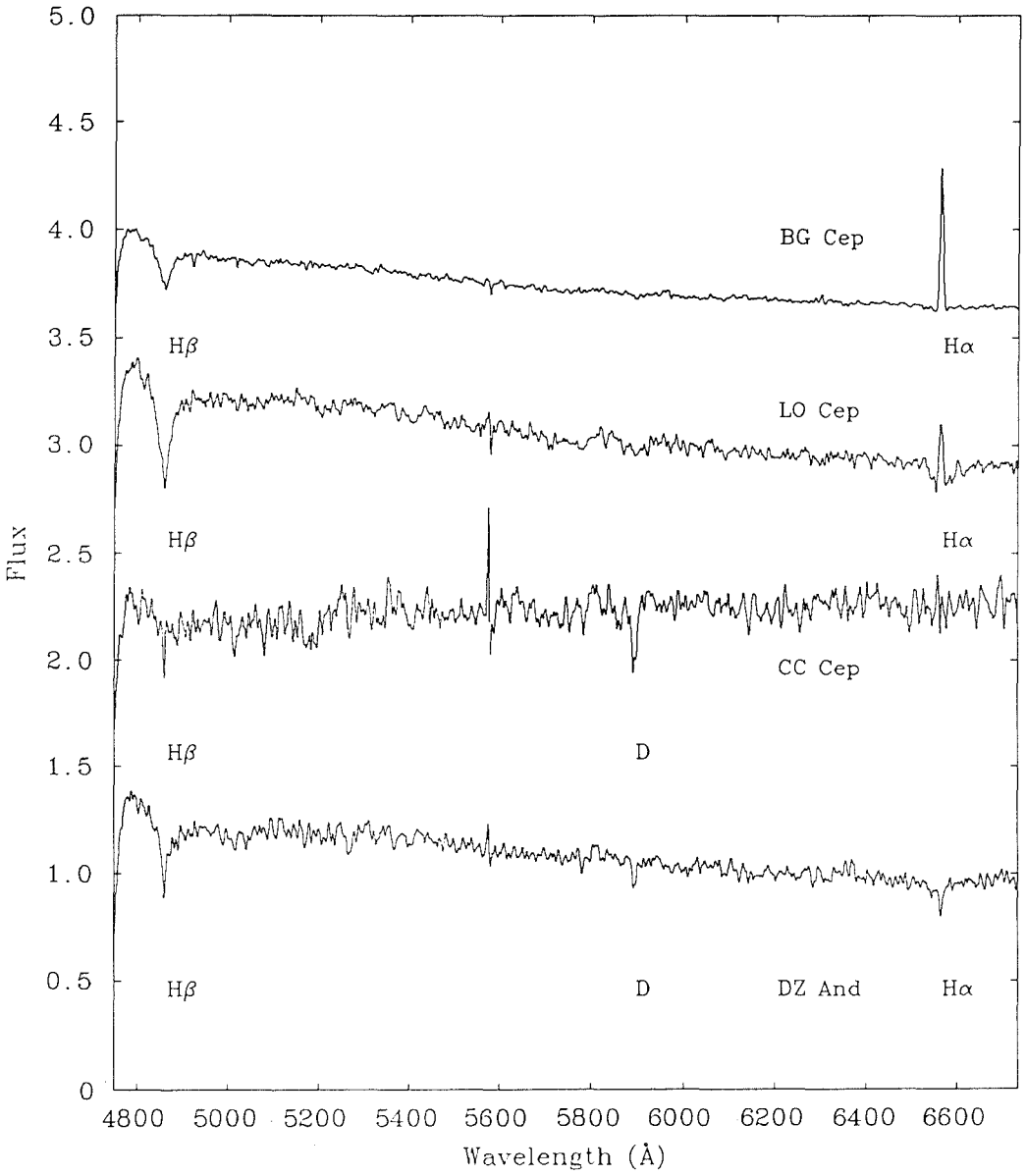

Figure 8.3: Red spectra of suspected R CrB stars.

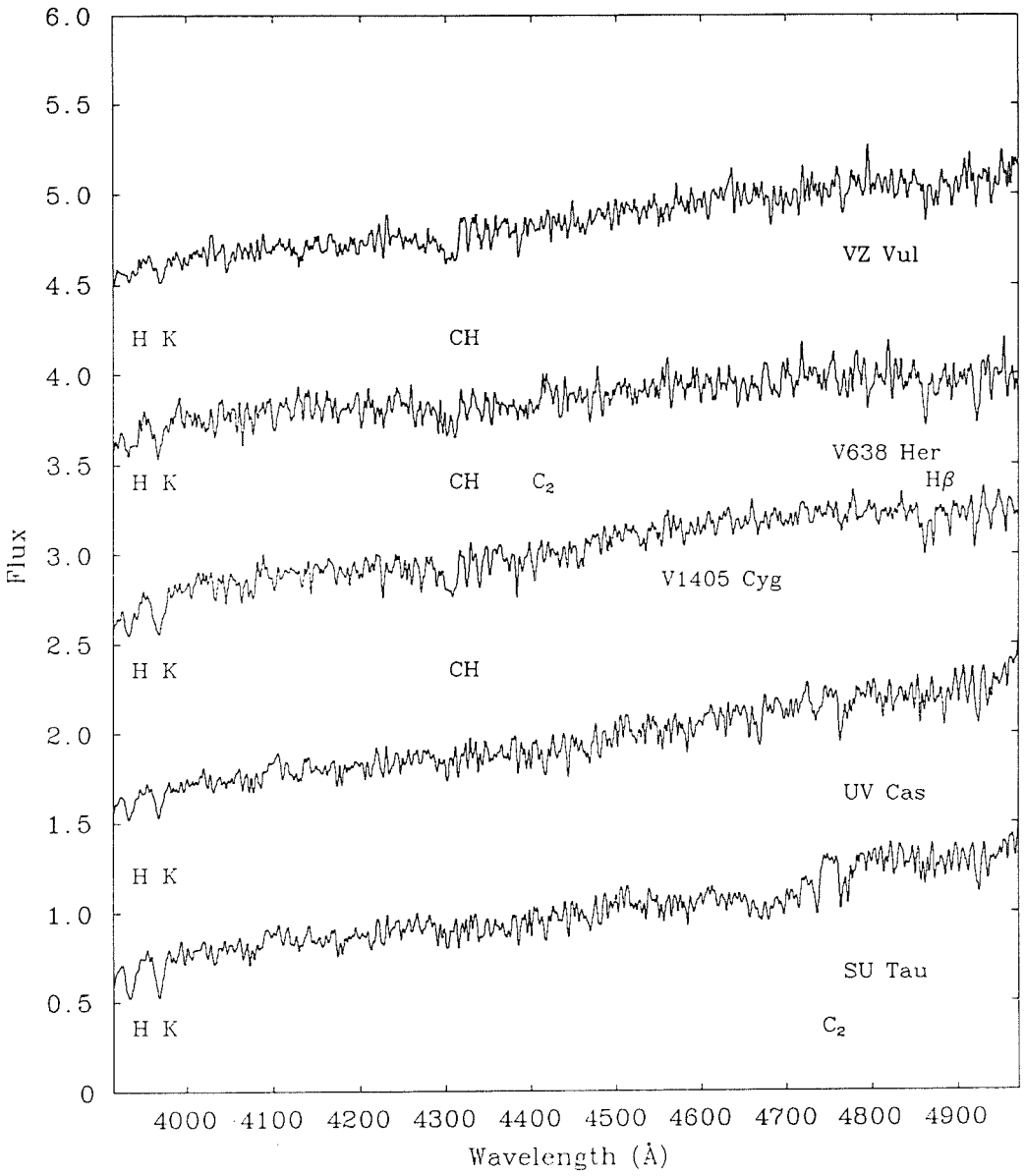

Figure 8.4: Blue spectra of suspected R CrB stars.

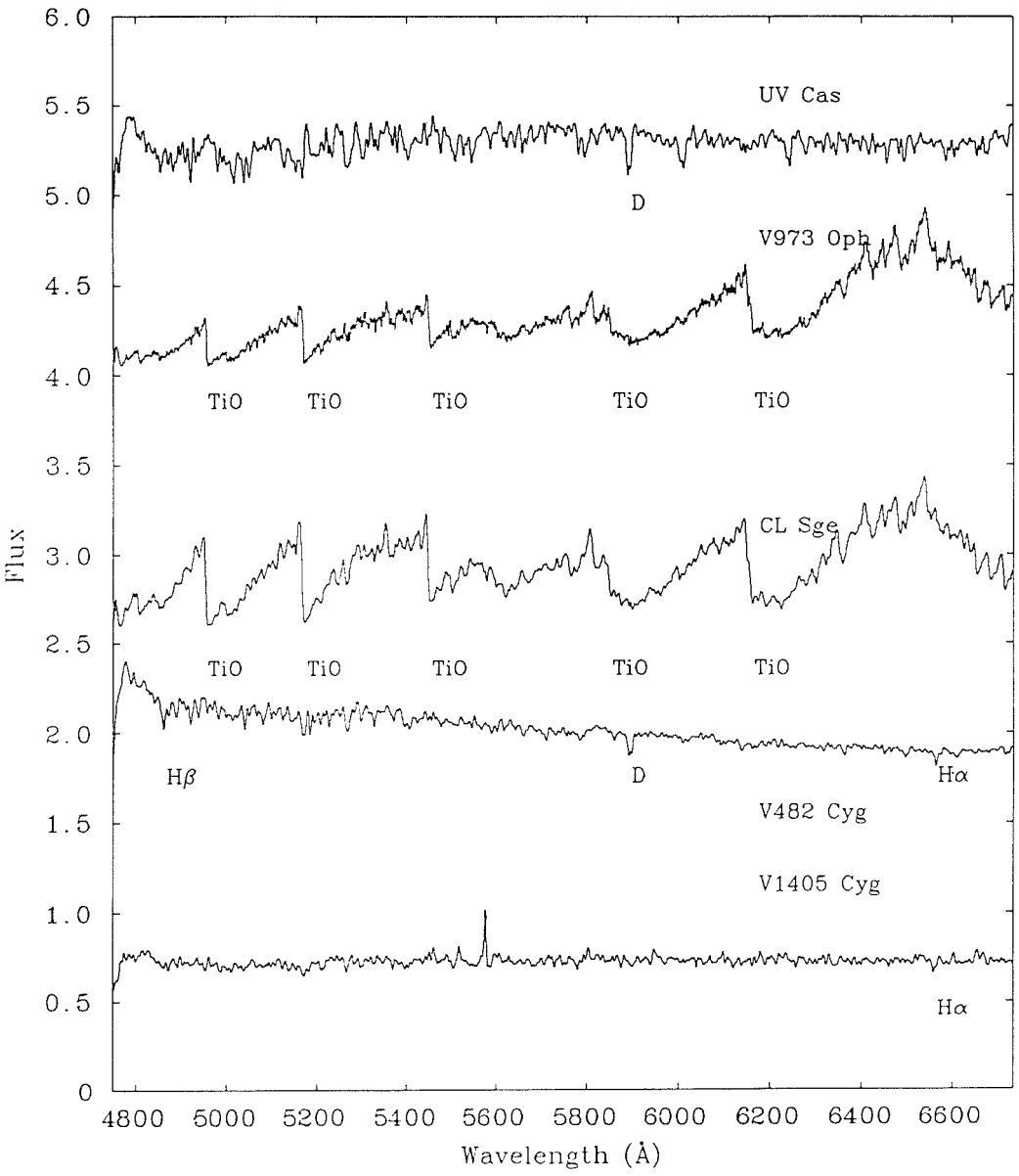

Figure 8.5: Red spectra of suspected R CrB stars.

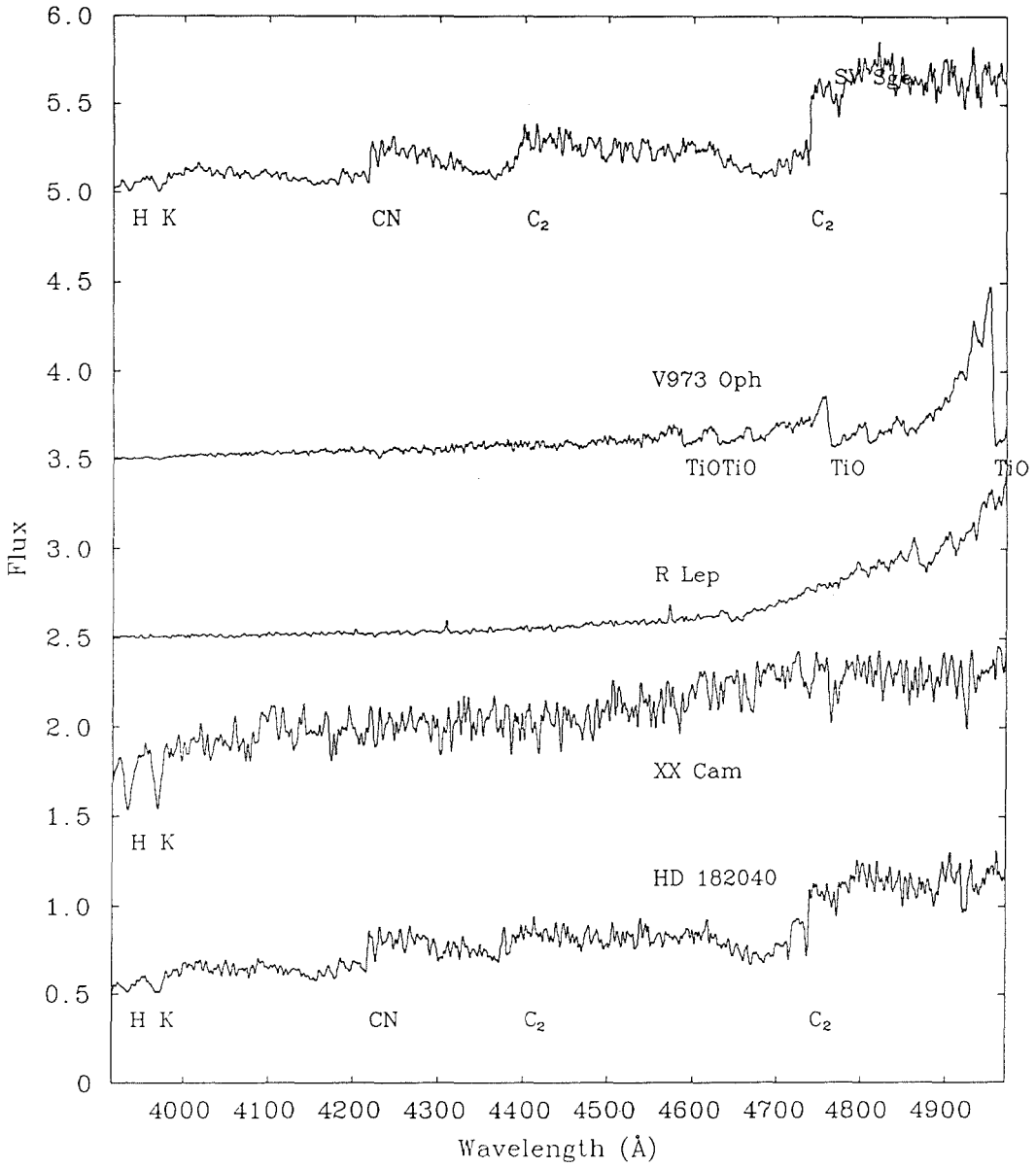

Figure 8.6: Blue spectra of suspected R CrB stars and XX Cam and HD 102040.

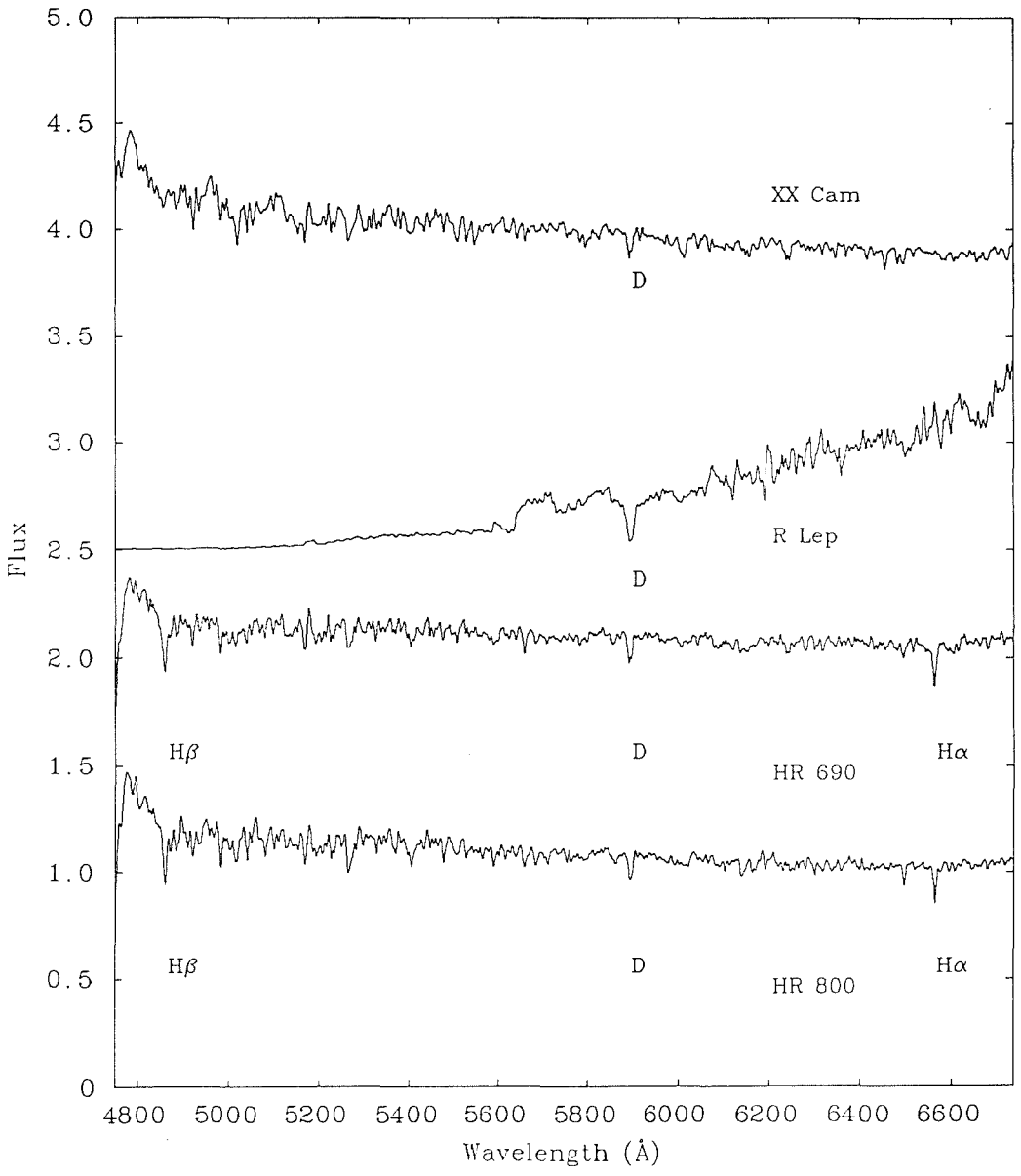

Figure 8.7: Red spectra of XX Cam and several carbon stars.

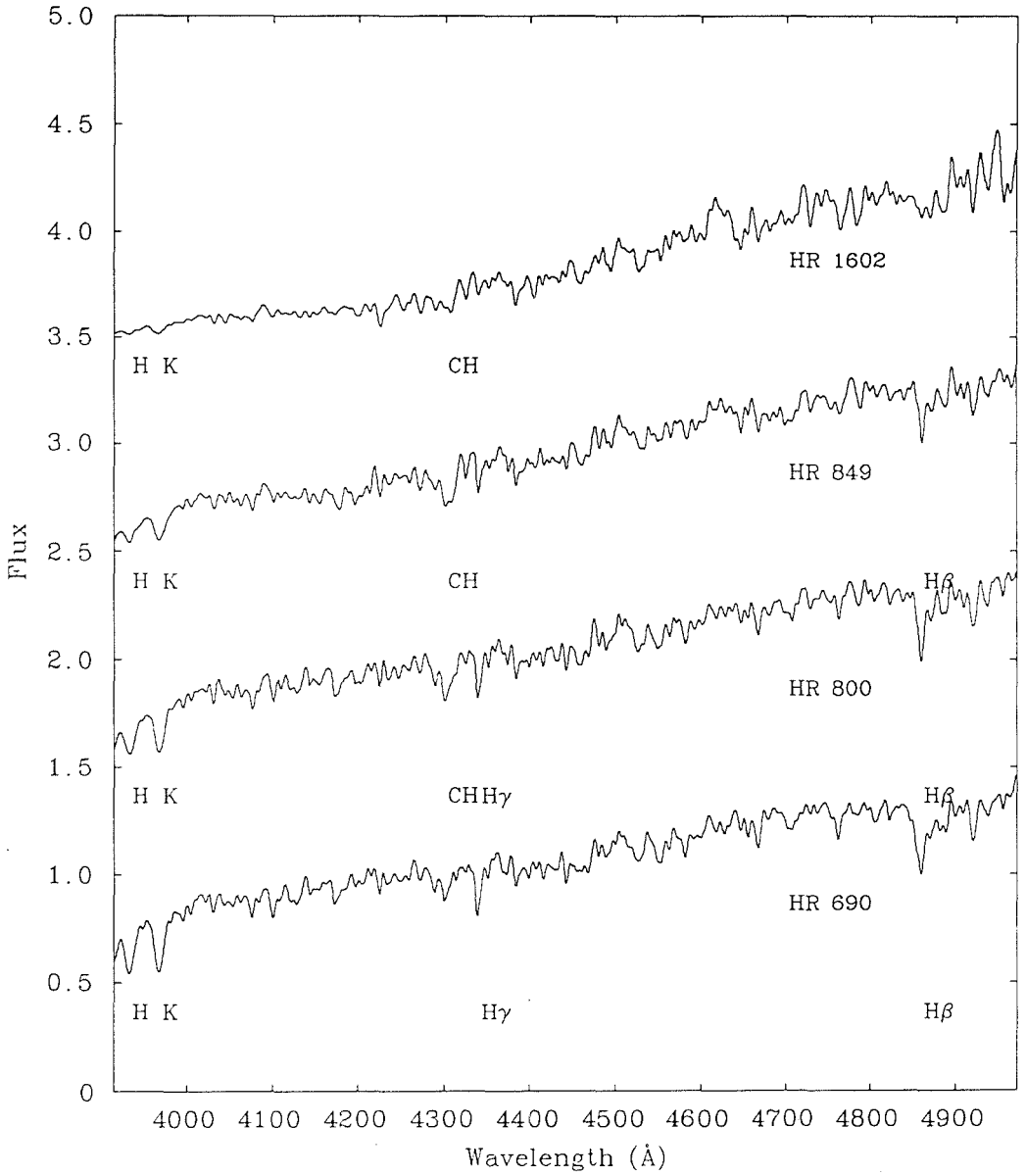

Figure 8.8: Blue spectra of known carbon stars.

in CC Cep. These spectra appear similar those of the carbon stars HR 800 and HR 849. Consequently these two stars are not R CrB stars.

8.3.4 RZ Vul

Only a spectrum in the blue region was obtained, showing Hβ, Hγ and Hδ. This star is not hydrogen-deficient and is similar to the carbon star HR 690.

8.3.5 VZ Vul, V638 Her and V1405 Cyg

Only weak Hβ and the CH G band at 4300Å may be seen in these stars. The presence of the strong CH band implies that the stars cannot be hydrogen-deficient and consequently are not R CrB stars. The spectra appear very similar to that of the carbon star HR 1602.

8.3.6 UV Cas and SU Tau

The blue spectra are very similar to that of XX Cam with no hydrogen or molecular bands visible. The presence of an infra-red excesses (Walker 1986) implies that the stars are R CrBs rather than HdC stars. There are no hydrogen lines visible in the blue or red spectrum.

8.3.7 SV Sge

No hydrogen lines are visible in the blue spectrum obtained. The spectrum is dominated by strong CN and C_2 molecular bands. The spectrum is very similar to that of the HdC star HD 182040 but has an observed infra-red excess (Walker 1986) so is most likely a R CrB star.

8.3.8 V973 Oph and CL Sge

The spectra are dominated by the presence of molecular bands due to TiO, typical of M type stars. No hydrogen lines may be seen in either the blue or red spectra which is to be expected given the low temperature of M type stars. It is unlikely that either star is a R CrB or HdC although hydrogen-deficiency is impossible to determine from the spectra.

8.3.9 V482 Cyg

Only a red spectrum was obtained showing weak Hα and Hβ. These hydrogen lines are weaker than those in the carbon stars but approximately the same strength as in V1405 Cyg. V1405 Cyg was judged hydrogen-rich on the basis of a strong G band but the absence of such a spectrum for V482 Cyg prevents such classification.

8.4 Literature Survey

The most recent catalogue of known R CrB and HdC stars is that of Drilling and Hill (1987) and is shown in Table 8.1. Many of the stars classified as R CrB from the GCVS have subsequently been identified within the literature as other types of stars.

AZ Cas a VV Cep binary system (M supergiant and B star) (Cowley (1976).

V425 Cas a cataclysmic binary (Bond and Chanmugam 1978).

V433 Cas a Mira (Rosino *et al.* 1976).

BH Lac spectrum contains strong sharp hydrogen lines (Herbig 1960)

V352 Aql a symbiotic star (Bond 1900).

SY Cep classified A3 (Herbig 1960) subsequently as a RW Aur variable (Artyukhina 1960).

Name	R.A.	(2000) Dec.	V	B-V	Comments
XX Cam	04 08 38.7	+53 21 39	7.30	0.87	
HV 5637	05 11 32	-67 56 00	15.79	1.37	LMC
W Men	05 26 24	-71 11 18	13.86	0.42	LMC
HV 12842	05 45 03	-64 24 24	13.65	0.51	LMC
SU Tau	05 49 06	+19 04 00	9.70	1.10	
UW Cen	12 43 17.1	-54 31 41	9.11	0.67	
Y Mus	13 05 48.4	-65 30 48	10.37	0.97	
NSV 6708	14 34 49.4	-39 33 20	7.00		
S Aps	15 09 24.6	-72 03 45	9.88	1.28	
HD 137613	15 27 48.3	-25 10 11	7.50	1.19	HdC
R CrB	15 48 34.4	+28 09 24	5.83	0.59	
RT Nor	16 24 19.0	-59 20 42	10.24	1.12	
HD 148839	16 35 45.9	-67 07 37	8.31	0.93	HdC
RZ Nor	16 32 41.5	-53 17 09	11.00	1.33	
LR Sco	17 27 54	-43 50 54	9.72	0.55	
WX CrA	18 08 50.4	-37 19 46	10.43	1.26	
V3975 Sgr	18 13 24	-25 47 24	10.97	1.02	
VZ Sgr	18 15 09	-29 42 24	10.15	0.73	
RS Tel	18 18 51.3	-46 32 54	9.77	0.81	
GU Sgr	18 24 15.5	-24 15 29	10.11	1.17	
HD 173409	18 46 26.5	-31 20 34	9.54	0.89	HdC
V CrA	18 47 32.2	-38 09 31	10.24	0.79	
HD 175893	18 58 47.4	-29 30 17	9.30	1.15	HdC
SV Sge	19 08 12	+17 37 42	10.39	1.86	
RY Sgr	19 16 32.8	-33 31 18	6.18	0.62	
HD 182040	19 23 10.1	-10 42 10	6.98	1.05	HdC
V482 Cyg	19 59 44	+33 58 30	12.1p		
U Aqr	22 03 20.0	-16 37 40	11.17	0.99	
UV Cas	23 02 13	+59 36 42	10.60	1.38	

Table 8.1: Catalogue of known HdC and R CrB stars.

VY Mon a RW Aur variable (Struve and Straka 1962). On the basis of a low dispersion spectrum reclassified as Geα with the suggestion that it may be a T Tauri star (Herbig and Rao 1974).

V405 Cen a cataclysmic variable of sub-class VY Scl (Kilkenny and Lloyd Evans 1989).

V803 Cen interacting binary white dwarfs (O'Donoghue *et al.* 1987).

AE Cir a symbiotic star (Kilkenny 1989a).

V618 Sgr a symbiotic star (Kilkenny 1989b).

MT Pup a symbiotic star (Kilkenny 1989b).

V605 Aql a Wolf-Rayet star (Seitter 1989).

SY Hyi not a R CrB star (Feast 1979).

Z Cir not a R CrB star (Feast 1974).

V1860 Sgr not a R CrB star (Feast 1974).

V731 Sco not a R CrB star (Feast 1974).

For the following list of stars no judgement can be made as to their classification until further observations have been made: UX Ant, V1405 Cyg, V1773 Oph, V589 Sgr and GM Ser.

8.5 Conclusion

The use of purely photometric observations as the basis of classification of a variable star as belonging to the R CrB class has been shown to result in erroneous identifications. This is illustrated with the misclassification of the stars in the previous sections. However, by using medium resolution spectroscopy and looking for the presence of hydrogen Balmer lines or the CH bands the hydrogen abundance may be estimated. Since R CrB stars are hydrogen-deficient, this provides a simple method of rejecting the mis-classified stars.

8.6 References

Artyukhina N.M., (1960) *Sov. Astron.*, 4, 91

Bond H.E., Chanmugam G., (1978) *Advances in Ultraviolet Astronomy: 4 years of IUE* p550

Bond H.E., (1969) *Publ. Astron. Soc. Pacific,* **88**, 192

Cowley A., (1976) *Publ. Astron. Soc. Pacific,* **81**, 297

Feast M.W., (1974) *In IAU Sym. No.***67**, *Variable Stars and Stellar Evolution, 129* eds. Sherwood V. and Plaut L.

Feast M.W., (1979) *In IAU Coll. No.***46**, *Changing Trends in Variable Star Research*

Herbig G.H., (1960) *Astrophys. J.,* **131**, 632

Herbig G.H., Rao N., (1974) *Astrophys. J.,* **174**, 401

Drilling J.S., Hill P.W., (1986) *In IAU Coll. No.* **87**, *Hydrogen-Deficient Stars and Related Objects,* 499 eds. Hunger, K., Schönberner D. and Rao, N. Kameswara., Reidel

Kilkenny D., Marang F., (1989) *Mon. Not. R. astr. Soc.,* **238**, 1p

Kilkenny D., Lloyd Evans T., (1989) *Observatory* Vol. **109** 85

Kilkenny D., (1989a) *Observatory* Vol. **109** 88

Kilkenny D., (1989b) *Observatory* Vol. **109** 229

Rosino L., Biannchini A., DiMartino D., (1976) *Astron. and Astrophy. Suppl.* **24**, 1

O'Donoghue D., Menzies J.W., Hill P.W., (1987) *Mon. Not. R. astr. Soc.,* **227**, 347

Oke J., (1974) *Astrophys. J. Suppl. Ser.,* **27**, 21

Schaefer B.E., (1986) *Astrophys. J.,* **307**, 644

Shortridge K., (1986) *Starlink User Note* **86.7**

Stone R., (1977) *Astrophys. J.,* **218**, 767

Struve O., Straka W.C., (1962) *Publ. Astron. Soc. Pacific,* **74**, 474

Walker H.J., (1986) *In IAU Coll. No.* **87**, *Hydrogen-Deficient Stars and Related Objects,* 407 eds. Hunger, K., Schönberner D. and Rao, N. Kameswara., Reidel

Warner B., (1967) *Mon. Not. R. astr. Soc.,* **137**, 119

Chapter 9

Conclusion

9.1 Photometry of Hydrogen-Deficient stars

The photometry of the R CrB and HdC stars was presented in Chapter 2. The observations obtained were insufficient to realise the aim of accurate period determination in order to compare with the predictions of the theoretical models. Variability was observed in all objects and tentative periods measured for S Aps, V CrA and U Aqr. As a result of the short time-base of the observations (6 months), it was only possible to search for periods in the interval 20–80 days. The periods found for these three objects agree with those of the theoretical models with temperatures of around 7000K.

Observations obtained over a time-base of several years at the Mount John Observatory of the same objects found periods significantly greater than those obtained here. Many of the stars were also multi-periodic. The longer periods (80–110 days) imply lower temperatures for these objects, provided that the theoretical period-temperature relationship is correct.

It is obvious that to obtain accurate periods, observations must be acquired over a time-scale of years and on a nightly basis. The only reasonable way to achieve this is through the use of dedicated automatic photoelectric photometers.

The observations of DY Cen presented in Chapter 3 confirmed the variability.

The periods measured agreed with those obtained previously. The dominant period of 3.8 days is consistent with the temperature-period relation for its estimated temperature. However, the observations of DY Cen presented in Chapter 2 showed significant variability over a much longer time-scale and with a large amplitude. Unfortunately insufficient data were obtained and no period determination was possible. The theoretical models do not predict either the large amplitude or the time-scale of the variability.

Again in order to obtain the data necessary for the long period determination the use of an automatic photoelectric photometer is required.

9.2 Model Atmospheres

The models presented in Chapter 5 are an improvement over the earlier models. This will be more apparent at low temperatures where the molecular opacity sources start to begin important. There are two main areas in which the models may be improved:

1. hydrogen-deficient opacity distribution functions,
2. the use of spherically symmetric models.

The use of hydrogen-rich opacity distribution functions provides a lower limit to the amount of line-blanketing present in the atmosphere. The resulting changes in the model's temperature structure occur in the region of line formation and will affect the derived temperature, gravity and composition.

The effects of sphericity are easily dealt with by solving the transfer equation in spherical coordinates. Such an algorithm already exists for the MARCS model atmosphere code. The difficulty in calculating spherical atmospheres arises not through the increased complexity of the radiation transport but indirectly through the lower surface temperatures. In the outer layers of such atmospheres the major opacity sources are minority molecular species such as water. The model temperature structure becomes very sensitive to small changes in the molecular abundances and this results in convergence difficulties.

9.3 The analysis of R CrB stars

New and improved models incorporating convection and metal line-blanketing were used to derive the atmospheric parameters of the R CrB stars R CrB and RY Sgr. the results obtained were in agreement with earlier attempts to within the estimated errors. The estimated errors were principally due to the difficulties in measuring the equivalent widths (EW) and in determining the C/He ratio.

The accurate measurement of EWs requires high resolution and signal-to-noise observation, which were obtained using the UCL echelle spectrograph (UCLES), together with accurate continuum placement. The design of UCLES results in short orders which only contain about 50Å of spectrum, but matches the size of current large ccds, *e.g.* Thomson 1024x1024. However, 50Å is insufficient to determine the placement of the continuum level when the spectrum contains many absorption lines as seen in the R CrB stars. A more traditional coudé spectrograph coupled to a *long* detector such as a RETICON would probably provide the means to obtain more accurate EW, although at the expense of requiring multiple exposures to obtain the same wavelength coverage.

Until a method of accurately determining C/He is found the errors in the derived parameters, especially the abundances, will remain large. Direct determination of C/He using the He I lines is unreliable due to their weakness and possible contamination by a chromospheric component. Further observation of the He I 10830Å in both stars is needed to determine whether a chromospheric component is present.

More accurate abundances of the key elements C, N and O together with s-process elements will be needed to discriminate between the various theoretical models of R CrB evolution. However, it must be noted that at present the theoretical models are not sophisticated enough to make reliable predictions of the key elements.

Future work must include analyses of the remaining R CrB and HdC stars. The methods presented in Chapter 7 for obtaining the atmospheric parameters are only suitable for the hotter stars ($T_{eff} \preceq 6000$K). Although the methods remain valid at lower temperatures the difficulties discussed above become extreme. Therefore the

cooler R CrB and HdC stars may best be analysed using the technique of spectrum synthesis, in which a theoretical spectrum is fitted to the observed spectrum.

9.4 Identification of R CrB stars

Intermediate resolution spectroscopy was shown to be a straight-forward means of rejecting mis-identified R CrB stars. Further observations are needed in order to confirm/reject the remaining "R CrB" stars.

Appendix A

Data tables for R CrB photometry

Each table contains the differential magnitudes plus the mean comparison colours. The time of observation is the helio-centric Julian date minus 2440000 and is shown in column 1.

H.J.D.	V	B-V	U-B	V-R	V-I
7303.35	10.292	0.971	0.473	0.536	0.982
7310.33	10.328	0.982	0.440	0.544	0.981
7311.30	10.321	0.972	0.470	0.544	0.987
7317.33	10.321	0.942	0.416	0.513	0.932
7336.24	10.331	0.949	0.471	0.537	0.971
7339.25	10.337	0.933	0.425	0.524	0.983
7342.24	10.278	0.939	0.358	0.520	0.961
7344.26	10.282	0.928	0.392	0.518	0.950
7353.25	10.330	0.955	0.413	0.537	1.006
7362.26	10.272	0.905	0.395	0.524	0.955
7373.26	10.276	0.935	0.402	0.525	0.958
7384.27	10.312	0.954	0.435	0.525	0.972
7388.26	10.305	0.937	0.432	0.536	0.973
7389.26	10.300	0.951	0.425	0.524	0.967
7391.25	10.304	0.950	0.432	0.518	0.972
7392.26	10.307	0.949	0.450	0.520	0.972
7393.24	10.284	0.925	0.405	0.511	0.953
7394.24	10.274	0.935		0.523	0.951
7399.25	10.292	0.945		0.519	0.961

Table A.1: Y Mus

H.J.D.	V	$B-V$	$U-B$	$V-R$	$V-I$
7280.58	9.842	1.252		0.760	1.501
7282.47	9.851	1.256		0.767	1.527
7283.40	9.852	1.256		0.767	1.516
7284.47	9.839	1.259		0.766	1.518
7299.40	9.622	1.236		0.769	1.457
7310.36	9.703	1.247	0.607	0.767	1.475
7311.37	9.706	1.247	0.577	0.770	1.486
7334.37	9.636	1.237	0.563	0.748	1.476
7336.35	9.630	1.239	0.566	0.769	1.468
7341.34	9.606	1.236	0.585	0.771	1.465
7342.29	9.632	1.253	0.580	0.775	1.474
7343.29	9.640	1.252	0.567	0.772	1.485
7347.29	9.695	1.253	0.590	0.777	1.483
7353.29	9.785	1.260	0.633	0.777	1.500
7362.31	9.785	1.253	0.588	0.761	1.497
7364.27	9.760	1.243	0.583	0.784	1.503
7367.26	9.705	1.245	0.601	0.784	1.490
7369.29	9.661	1.229	0.615	0.776	1.476
7372.25	9.591	1.220	0.542	0.769	1.454
7376.25	9.561	1.233	0.583	0.768	1.452
7380.24	9.572	1.239	0.578	0.760	1.452
7382.26	9.586	1.229	0.583	0.762	1.451
7383.27	9.586	1.226	0.574	0.768	1.453
7384.32	9.583	1.230	0.570	0.758	1.450
7385.25	9.583	1.224	0.573	0.765	1.459
7389.28	9.596	1.236	0.557	0.760	1.457
7390.31	9.620	1.240	0.578	0.774	1.470
7391.33	9.620	1.231	0.593	0.772	1.463
7393.31	9.656	1.245	0.578	0.770	1.477
7399.31	9.722	1.247		0.779	1.500
7400.32	9.716	1.231		0.785	1.493
7408.28	9.660	1.235		0.780	1.477

Table A.2: S Aps

H.J.D.	V	B-V	U-B	V-R	V-I
7281.47	10.056	1.059	0.965	0.561	1.004
7282.58	10.079	1.037	0.483	0.540	0.926
7299.51	10.188	1.072	0.126	0.565	0.960
7310.40	10.308	1.169	0.804	0.605	1.010
7313.50	10.326	1.169	0.728	0.609	1.017
7337.36	10.263	1.096	0.743	0.571	0.954
7343.34	10.229	1.086	0.736	0.561	0.937
7344.34	10.215	1.082	0.719	0.566	0.947
7352.31	10.248	1.112	0.784	0.590	0.980
7353.31	10.275	1.143	0.788	0.590	0.991
7364.37	10.333	1.140	0.760	0.591	0.998
7367.28	10.332	1.132	0.722	0.582	0.996
7368.30	10.317	1.125	0.682	0.575	0.992
7372.32	10.271	1.058	0.704	0.555	0.943
7373.29	10.259	1.057	0.661	0.560	0.952
7376.29	10.224	1.048	0.622	0.551	0.935
7378.30	10.196	1.027	0.641	0.540	0.917
7383.33	10.141	1.032	0.635	0.532	0.915
7385.27	10.090	1.025	0.636	0.532	0.902
7388.30	10.101	1.056	0.678	0.546	0.932
7389.32	10.119	1.061	0.683	0.557	0.939
7390.35	10.147	1.067	0.698	0.553	0.943
7392.42	10.206	1.087	0.736	0.561	0.966
7393.39	10.236	1.106	0.742	0.578	0.978
7399.38	10.444	1.138	0.126	0.600	1.018
7408.34	10.487	1.133	0.126	0.597	1.010

Table A.3: RT Nor

H.J.D.	V	$B-V$	$U-B$	$V-R$	$V-I$
7281.56	9.981	0.770	0.284	0.500	0.899
7283.59	9.998	0.771	0.590	0.507	0.903
7299.63	10.048	0.797	0.238	0.524	0.925
7311.59	10.060	0.550	0.869	0.490	0.915
7334.57	9.840	0.735	0.173	0.463	0.821
7354.46	9.957	0.742	0.175	0.475	0.845
7368.45	10.011	0.742	0.177	0.489	0.866
7372.47	10.006	0.732	0.169	0.490	0.870
7378.34	9.974	0.737	0.178	0.481	0.858
7383.48	9.912	0.728	0.171	0.465	0.829
7384.48	9.900	0.740	0.152	0.455	0.820
7385.45	9.901	0.724	0.156	0.460	0.827
7386.41	9.897	0.724	0.162	0.456	0.826
7388.41	9.892	0.724	0.157	0.457	0.827
7389.47	9.888	0.729	0.158	0.462	0.830
7390.48	9.880	0.737	0.159	0.457	0.816
7393.45	9.879	0.731	0.049	0.467	0.820
7394.47	9.886	0.732	0.205	0.471	0.835
7399.46	9.911	0.749	0.086	0.479	0.845
7408.40	9.867	0.732	0.086	0.488	0.855
7409.34	9.865	0.735	0.086	0.483	0.852
7435.32	9.958	0.735	0.186	0.476	0.834
7436.32	9.963	0.736	0.086	0.470	0.839
7437.32	9.981	0.728	0.086	0.473	0.845
7438.32	10.001	0.739	0.086	0.471	0.842

Table A.4: V CrA

H.J.D.	V	B-V	U-B	V-R	V-I
7310.67	11.063	0.995	0.277	0.644	1.114
7311.65	11.083	1.047	0.344	0.658	1.131
7342.62	10.902	0.930	0.294	0.589	1.022
7353.58	10.937	0.957	0.207	0.623	1.074
7354.58	10.945	0.950	0.211	0.625	1.070
7364.56	10.901	0.942	0.237	0.614	1.045
7366.55	10.906	0.941	0.238	0.621	1.058
7369.52	10.851	0.936	0.267	0.607	1.022
7374.56	10.885	0.941	0.275	0.625	1.069
7383.53	10.889	0.930	0.223	0.617	1.046
7384.55	10.888	0.921	0.218	0.610	1.050
7385.53	10.891	0.918	0.223	0.613	1.043
7386.48	10.894	0.922	0.225	0.605	1.041
7387.54	10.909	0.927	0.205	0.609	1.048
7388.50	10.922	0.920	0.224	0.619	1.055
7389.51	10.923	0.932	0.215	0.611	1.041
7390.55	10.931	0.926	0.221	0.605	1.045
7393.53	10.948	0.918	0.223	0.606	1.041
7394.53	10.945	0.929	0.211	0.609	1.038
7394.52	10.966	0.944	0.263	0.600	1.013
7408.48	10.890	0.921	0.129	0.596	1.019
7409.43	10.883	0.915	0.129	0.613	1.026
7435.41	10.886	0.947	0.129	0.615	1.046
7436.41	10.894	0.946	0.129	0.620	1.044

Table A.5: U Aqr

H.J.D.	V	B-V	U-B	V-R	V-I
7281.52	7.526	1.202	0.863	0.618	1.077
7303.47	7.454	1.202	0.882	0.616	1.051
7336.39	7.475	1.198	0.850	0.608	1.051
7343.31	7.528	1.200	0.868	0.614	1.063
7344.31	7.536	1.207	0.868	0.609	1.064
7352.29	7.501	1.197	0.732	0.609	1.051
7354.27	7.479	1.196	0.825	0.608	1.046
7372.28	7.482	1.201	0.881	0.609	1.053
7383.29	7.520	1.203	0.856	0.614	1.059
7384.34	7.531	1.206	0.863	0.617	1.067
7385.29	7.518	1.199	0.880	0.614	1.060
7389.30	7.524	1.211	0.867	0.620	1.072
7390.33	7.545	1.212	0.891	0.619	1.078
7391.31	7.542	1.204	0.891	0.622	1.081
7393.29	7.544	1.199	0.907	0.621	1.080
7399.29	7.488	1.204	0.199	0.606	1.064
7400.31	7.487	1.193	0.199	0.606	1.061
7408.26	7.502	1.218	0.199	0.616	1.062
7409.25	7.508	1.211	0.199	0.621	1.066

Table A.6: HD 137613

H.J.D.	V	$B-V$	$U-B$	$V-R$	$V-I$
7310.63	9.443	1.201	0.925	0.590	0.972
7313.61	9.413	1.180	0.850	0.581	0.958
7318.58	9.416	1.196	0.876	0.580	0.948
7334.61	9.585	1.233	0.942	0.605	1.004
7354.53	9.423	1.178	0.877	0.578	0.950
7364.48	9.389	1.166	0.842	0.581	0.960
7372.49	9.501	1.167	0.837	0.583	0.978
7373.48	9.479	1.179	0.869	0.578	0.964
7376.42	9.457	1.177	0.859	0.583	0.966
7383.50	9.238	1.113	0.393	0.571	0.911
7384.50	9.235	1.131	0.779	0.563	0.921
7385.48	9.210	1.116	0.790	0.552	0.914
7386.43	9.246	1.130	0.786	0.566	0.926
7388.43	9.264	1.133	0.808	0.564	0.924
7389.49	9.298	1.132	0.819	0.562	0.935
7390.50	9.290	1.122	0.817	0.566	0.925
7393.49	9.357	1.134	0.831	0.555	0.927
7408.44	9.429	1.137	0.785	0.575	0.964
7409.39	9.427	1.139	0.788	0.570	0.951
7435.34	9.336	1.131	0.786	0.567	0.922
7436.34	9.344	1.126	0.810	0.562	0.950
7437.34	9.352	1.142	0.799	0.568	0.944
7438.34	9.401	1.150	0.794	0.573	0.957

Table A.7: HD 175893

H.J.D.	V	B-V	U-B	V-R	V-I
7310.47	9.822	0.858	-0.092	0.620	1.278
7318.51	9.731	0.853	-0.090	0.610	1.266
7336.43	9.834	0.852	-0.093	0.612	1.275
7337.41	9.831	0.867	-0.082	0.621	1.293
7342.42	9.768	0.836	-0.096	0.599	1.256
7343.39	9.832	0.884	-0.112	0.626	1.298
7353.37	9.804	0.879	-0.111	0.618	1.295
7354.35	9.800	0.851	-0.098	0.610	1.275
7364.41	9.736	0.857	-0.113	0.611	1.276
7372.38	9.817	0.847	-0.083	0.618	1.288
7373.35	9.811	0.856	-0.095	0.620	1.285
7383.36	9.807	0.849	-0.098	0.605	1.273
7384.44	9.813	0.853	-0.108	0.612	1.273
7385.41	9.810	0.851	-0.107	0.612	1.274
7388.37	9.786	0.853	-0.101	0.616	1.274
7389.33	9.778	0.850	-0.094	0.616	1.275
7390.42	9.787	0.852	-0.096	0.614	1.272
7392.44	9.781	0.857	-0.099	0.617	1.286
7393.43	9.774	0.856	-0.097	0.624	1.264
7394.44	9.779	0.857	-0.100	0.611	1.277
7437.28	9.780	0.862	-0.099	0.618	1.280
7438.28	9.781	0.849	-0.099	0.609	1.275

Table A.8: HD 320156

H.J.D.	V	$B-V$	$U-B$	$V-R$	$V-I$
7310.50	11.021	0.362	-0.451	0.270	0.547
7311.54	11.048	0.365	-0.435	0.268	0.566
7313.52	11.067	0.380	-0.477	0.270	0.556
7337.45	11.030	0.359	-0.486	0.265	0.550
7342.45	11.095	0.330	-0.448	0.300	0.661
7343.41	11.006	0.354	-0.463	0.250	0.533
7352.40	11.104	0.266	-0.434	0.341	0.583
7353.39	10.976	0.361	-0.469	0.271	0.545
7354.38	10.981	0.357	-0.455	0.262	0.535
7372.41	10.979	0.343	-0.463	0.266	0.554
7373.38	10.961	0.360	-0.469	0.256	0.546
7380.33	10.991	0.356	-0.456	0.258	0.540
7383.39	10.977	0.363	-0.460	0.269	0.550
7384.39	10.992	0.361	-0.464	0.273	0.557
7385.36	11.006	0.358	-0.465	0.259	0.545
7386.35	11.007	0.364	-0.478	0.258	0.547
7388.33	10.976	0.361	-0.467	0.258	0.546
7389.36	10.991	0.355	-0.458	0.272	0.555
7391.37	11.016	0.361	-0.462	0.269	0.562
7392.36	11.041	0.399	-0.469	0.276	0.561
7393.34	11.037	0.350	-0.463	0.262	0.544
7394.39	11.003	0.357	-0.439	0.261	0.553
7432.28	11.097	0.382	-0.446	0.277	0.569
7437.27	11.036	0.359	-0.449	0.262	0.524
7438.26	11.028	0.365	-0.440	0.278	0.570

Table A.9: LSIV -1 2

H.J.D.	V	$B-V$	$U-B$	$V-R$	$V-I$
7310.53	10.310	0.573	-0.044	0.403	0.793
7336.59	10.404	0.463	-0.281	0.391	0.745
7343.43	10.411	0.456	-0.234	0.392	0.753
7354.40	10.427	0.487	-0.259	0.398	0.773
7364.45	10.356	0.472	-0.266	0.389	0.759
7373.42	10.351	0.467	-0.261	0.397	0.754
7376.36	10.334	0.467	-0.261	0.389	0.749
7383.42	10.350	0.466	-0.256	0.391	0.765
7384.42	10.328	0.461	-0.257	0.390	0.761
7385.39	10.323	0.471	-0.256	0.382	0.744
7388.35	10.322	0.471	-0.250	0.382	0.756
7389.38	10.331	0.468	-0.264	0.392	0.759
7390.44	10.321	0.471	-0.273	0.399	0.761
7391.39	10.304	0.477	-0.269	0.391	0.759
7392.40	10.313	0.478	-0.258	0.389	0.754
7393.36	10.341	0.455	-0.236	0.379	0.743
7394.41	10.340	0.473	-0.255	0.399	0.765

Table A.10: BD-1 3438

H.J.D.	V	$B-V$	$U-B$	$V-R$	$V-I$
7299.65	9.601	0.185	-0.555	0.120	0.223
7310.65	9.497	0.189	-0.550	0.121	0.232
7311.64	9.496	0.196	-0.548	0.122	0.236
7318.61	9.560	0.190	-0.521	0.172	0.361
7334.65	9.521	0.196	-0.539	0.128	0.245
7336.63	9.507	0.194	-0.536	0.119	0.236
7337.59	9.497	0.184	-0.546	0.118	0.240
7342.57	9.502	0.180	-0.535	0.115	0.237
7353.53	9.500	0.180	-0.546	0.128	0.237
7364.51	9.557	0.187	-0.544	0.119	0.226
7372.51	9.524	0.188	-0.536	0.118	0.227
7373.55	9.515	0.187	-0.545	0.114	0.221
7374.52	9.502	0.184	-0.534	0.111	0.217
7384.52	9.587	0.206	-0.508	0.127	0.239
7385.50	9.577	0.189	-0.502	0.120	0.234
7388.45	9.557	0.191	-0.523	0.123	0.235
7389.45	9.549	0.188	-0.529	0.123	0.232
7390.52	9.540	0.195	-0.527	0.119	0.236
7392.53	9.542	0.207	-0.540	0.120	0.235
7393.51	9.569	0.192	-0.521	0.119	0.244
7394.51	9.575	0.198	-0.519	0.111	0.231
7435.38	9.551	0.183	-0.528	0.136	0.251
7436.36	9.544	0.191	-0.541	0.114	0.231
7437.36	9.543	0.186	-0.539	0.127	0.232

Table A.11: BD+1 4381

H.J.D.	V	$B-V$	$U-B$	$V-R$	$V-I$
7299.59	9.291	-0.002	-0.665	0.051	0.106
7310.57	9.276	-0.003	-0.659	0.061	0.108
7311.57	9.267	-0.002	-0.666	0.050	0.102
7318.53	9.319	-0.013	-0.664	0.055	0.104
7336.57	9.332	-0.002	-0.671	0.055	0.107
7342.51	9.318	-0.000	-0.670	0.043	0.099
7343.47	9.315	-0.002	-0.662	0.056	0.106
7353.47	9.337	0.014	-0.671	0.058	0.115
7354.44	9.346	-0.001	-0.658	0.054	0.111
7366.44	9.289	-0.004	-0.661	0.053	0.106
7368.41	9.241	0.010	-0.661	0.051	0.104
7369.42	9.271	0.005	-0.670	0.054	0.107
7372.43	9.256	-0.007	-0.665	0.048	0.101
7373.44	9.258	-0.001	-0.666	0.048	0.108
7374.47	9.274	-0.003	-0.670	0.057	0.114
7377.37	9.290	-0.008	-0.660	0.050	0.101
7379.34	9.263	-0.005	-0.676	0.049	0.098
7383.44	9.265	-0.010	-0.674	0.054	0.106
7384.46	9.277	0.005	-0.672	0.052	0.102
7385.43	9.301	0.002	-0.670	0.060	0.110
7386.38	9.329	0.003	-0.664	0.046	0.104
7388.39	9.296	-0.001	-0.652	0.055	0.111
7389.43	9.280	0.002	-0.667	0.061	0.108
7390.45	9.277	-0.010	-0.670	0.060	0.110
7392.50	9.255	-0.006	-0.663	0.055	0.103
7393.47	9.282	0.003	-0.662	0.051	0.111
7394.49	9.307	-0.006	-0.658	0.055	0.112
7398.46	9.305	-0.003	-0.686	0.054	0.100
7399.47	9.309	0.009	-0.668	-0.012	0.110
7408.42	9.309	-0.003	-0.663	-0.012	-0.025
7409.37	9.323	-0.000	-0.669	-0.012	-0.025
7432.32	9.253	-0.029	-0.643	0.006	0.073
7435.30	9.239	-0.007	-0.673	0.057	0.112
7436.30	9.248	-0.008	-0.677	0.055	0.108
7437.30	9.254	-0.010	-0.665	0.051	0.103

H.J.D.	V	$B-V$	$U-B$
7299.45459	12.8375	0.3483	0.0510
7336.29688	13.1942	0.3533	-0.8920
7337.30225	13.0242	0.3033	-0.7900
7339.27979	12.6292	0.3178	-0.5515
7341.28613	13.2842	0.1688	-0.9635
7342.25879	12.9842	0.3223	-0.8940
7343.24805	13.0942	0.1538	-0.7945
7344.27979	13.1642	0.3153	-0.8920
7347.25293	13.2292	0.3253	-0.9075
7353.26758	13.1042	0.3763	-0.8720
7354.24316	13.2492	0.3538	-0.8555
7369.26367	12.3542	0.4133	-0.5840
7372.22656	12.5592	0.2963	-0.6225
7384.28857	12.8342	0.3323	-0.6065
7385.23291	12.6992	0.3513	-0.6295
7388.27832	12.7442	0.3193	-0.6020
7389.23877	12.7842	0.3393	-0.6145
7390.28223	12.7375	0.3313	-0.6053
7391.28027	12.7542	0.3953	-0.6215
7393.26465	12.7017	0.4543	-0.6472
7394.26514	12.7942	0.3588	-0.5625
7399.27197	12.8659	0.3246	-0.6337
7400.26416	12.9092	0.3213	-0.4380
7408.23877	12.8442	0.3333	-0.5868

Table A.13: DY Cen

Appendix B

Data table for DY Cen photometry.

The table contains the magnitudes and colours of the HD 116562 (C) together with the differential magnitudes and colours for DY Cen (V) and the HD 116388 (Ck), see chapter 3 for details.

HJD	Comparison			Variable - Comparison			Check - Comparison		
+244000	V	B-V	U-B	V	B-V	U-B	V	B-V	U-B
7635.41	9.410	0.274	0.111	3.247	0.054	-0.765	-1.827	-0.209	-0.053
7635.47	9.416	0.276	0.114	3.241	0.041	-0.763	-1.827	-0.211	-0.054
7635.59	9.423	0.284	0.122	3.245	0.104	-0.672	-1.828	-0.209	-0.065
7641.28	9.400	0.272	0.103				-1.821	-0.201	-0.050
7641.35	9.411	0.277	0.107	3.427	-0.003	-0.795	-1.832	-0.201	-0.048
7641.54	9.402	0.278	0.107	3.339	0.038	-0.739	-1.819	-0.208	-0.053
7642.25	9.408	0.270	0.100	3.392	0.041	-0.738	-1.830	-0.199	-0.061
7642.30	9.399	0.272	0.108				-1.820	-0.208	-0.057
7642.37	9.409	0.274	0.106	3.320	0.042	-0.796	-1.826	-0.208	-0.049
7642.46	9.408	0.274	0.107	3.304	0.058	-0.783	-1.827	-0.209	-0.050
7642.57	9.404	0.272	0.099	3.280	0.047	-0.746	-1.827	-0.215	-0.048
7643.26	9.403	0.271	0.102	3.361	0.040	-0.760	-1.824	-0.213	-0.049
7643.31	9.417	0.278	0.114	3.372	0.039	-0.761	-1.823	-0.203	-0.055
7643.37	9.411	0.278	0.114	3.348	0.013	-0.768	-1.820	-0.210	-0.047
7643.46	9.405	0.273	0.106	3.338	0.053	-0.788	-1.823	-0.208	-0.054
7643.56	9.402	0.268	0.097	3.336	0.069	-0.763	-1.822	-0.207	-0.051
7644.26	9.415	0.274	0.107	3.464	0.035	-0.764	-1.818	-0.205	-0.058
7645.25	9.410	0.273	0.104	3.469	0.021	-0.775	-1.824	-0.217	-0.060
7645.30	9.411	0.274	0.111	3.447	0.027	-0.764	-1.835	-0.201	-0.058
7645.36	9.410	0.277	0.115	3.422	0.046	-0.782	-1.831	-0.207	-0.058
7645.44	9.408	0.277	0.110	3.408	0.039	-0.768	-1.827	-0.207	-0.052
7645.59	9.391	0.268	0.093	3.372	0.055	-0.754	-1.807	-0.207	-0.060

HJD	Comparison			Variable - Comparison			Check - Comparison		
+244000	V	B-V	U-B	V	B-V	U-B	V	B-V	U-B
7646.27	9.406	0.272	0.104	3.419	0.025	-0.743	-1.823	-0.208	-0.054
7646.33	9.409	0.271	0.110	3.414	0.034	-0.755	-1.821	-0.207	-0.056
7646.41	9.407	0.272	0.111	3.394	0.044	-0.751	-1.817	-0.207	-0.054
7646.46	9.406	0.275	0.109	3.396	0.085	-0.781	-1.820	-0.209	-0.053
7646.55	9.402	0.272	0.102	3.362	0.055	-0.749	-1.823	-0.209	-0.053
7647.27	9.399	0.271	0.106	3.423	0.038	-0.753	-1.825	-0.211	-0.054
7647.34	9.406	0.272	0.113	3.408	0.044	-0.749	-1.828	-0.211	-0.053
7647.42	9.407	0.274	0.109	3.388	0.052	-0.760	-1.830	-0.208	-0.050
7647.46	9.408	0.274	0.110	3.382	0.051	-0.760	-1.832	-0.208	-0.050
7647.51	9.409	0.273	0.110	3.363	0.069	-0.760	-1.828	-0.208	-0.053
7647.58	9.420	0.276	0.108	3.386	0.045	-0.750	-1.823	-0.207	-0.050
7648.33	9.408	0.274	0.113	3.404	0.039	-0.769	-1.822	-0.205	-0.056
7648.38	9.405	0.275	0.114	3.399	0.050	-0.771	-1.818	-0.207	-0.055
7648.46	9.402	0.273	0.112	3.382	0.053	-0.770	-1.817	-0.209	-0.052
7648.53	9.401	0.273	0.107	3.389	0.061	-0.764	-1.817	-0.210	-0.052
7650.46	9.411	0.274	0.107	3.291	0.057	-0.762			
7650.54	9.404	0.272	0.089				-1.826	-0.203	-0.034
7651.28	9.417	0.276	0.108	3.352	0.038	-0.755	-1.834	-0.205	-0.061
7651.40	9.402	0.274	0.107	3.341	0.043	-0.764	-1.825	-0.206	-0.055
7651.49	9.407	0.272	0.108	3.338	0.048	-0.770	-1.833	-0.207	-0.051
7651.53	9.399	0.278	0.108	3.331	0.045	-0.742	-1.825	-0.207	-0.056
7651.59	9.400	0.275	0.102	3.338	0.050	-0.752			
7652.24	9.418	0.269	0.107	3.443	0.041	-0.783	-1.826	-0.202	-0.060
7652.29	9.410	0.271	0.106	3.453	0.030	-0.764	-1.825	-0.208	-0.056
7652.41	9.409	0.274	0.102	3.435	0.041	-0.760	-1.828	-0.209	-0.051
7652.46	9.409	0.272	0.104	3.453	0.034	-0.758	-1.830	-0.207	-0.049
7652.53	9.410	0.275	0.104	3.454	0.048	-0.765	-1.830	-0.207	-0.049
7653.41	9.402	0.273	0.105	3.401	0.042	-0.745	-1.811	-0.212	-0.052
7653.45	9.402	0.273	0.111	3.374	0.047	-0.753	-1.817	-0.209	-0.054
7653.49	9.406	0.277	0.114	3.371	0.043	-0.758	-1.817	-0.217	-0.054
7653.54	9.407	0.281	0.112	3.381	0.048	-0.745	-1.820	-0.211	-0.053
7657.25	9.425	0.267	0.111	3.377	0.030	-0.759	-1.835	-0.198	-0.062
7657.35	9.412	0.271	0.111	3.364	0.048	-0.779	-1.830	-0.207	-0.055
7657.39	9.408	0.273	0.109	3.360	0.038	-0.768	-1.830	-0.208	-0.047